

# Introduction and Structural Characterizations of Defects on Nano Carbon Materials

January 2015

Jungpil Kim  
Graduate School of Engineering  
CHIBA UNIVERSITY

(千葉大学審査学位論文)

# Introduction and Structural Characterizations of Defects on Nano Carbon Materials

January 2015

Jungpil Kim  
Graduate School of Engineering  
CHIBA UNIVERSITY

## **Outline**

<b>Abstract</b>	<b>1</b>
<b>Chapter 1 Background of this research</b>	<b>2</b>
1.1 Nano carbon materials	2
1.1.1 Fullerenes	3
1.1.2 Carbon nanotubes	6
1.1.3 Graphene	8
1.1.4 Characterization	12
1.2 Defects in nano carbon materials	13
1.2.1 Pentagons and heptagons	13
1.2.2 Vacancy defect	15
1.2.3 Functional groups	17
1.3 Spectroscopic analysis of defects	17
1.3.1 Infrared spectroscopy	18
1.3.2 X-ray photoelectron spectroscopy	18
1.3.3 Raman spectroscopy	20
1.4 Density functional theory calculation	21
1.5 Purpose of this study	21
1.5.1 Spectral change of simulated X-ray photoelectron spectroscopy from graphene to fullerene	21
1.5.2 Pyrolysis of epoxidized fullerenes analyzed by spectroscopies	23
1.5.3 Oxygen migration and selective CO and CO <sub>2</sub> formation from epoxidized fullerenes	25
<b>Chapter 2 Experimental</b>	<b>27</b>
2.1 X-ray photoelectron spectroscopy of fullerene related materials	27
2.1.1 Spectral change of simulated X-ray photoelectron spectroscopy from graphene to fullerene	27
2.1.1.1 Simulation of X-ray photoelectron spectroscopy	27
2.1.1.2 Measurement of X-ray photoelectron spectroscopy	32
2.1.2 Pyrolysis of epoxidized fullerenes analyzed by spectroscopies	32
2.1.2.1 Simulation of X-ray photoelectron spectroscopy	32
2.1.2.2 Measurement of X-ray photoelectron spectroscopy	32
2.2 Other experimental parts	33

2.2.1 Pyrolysis of epoxidized fullerenes analyzed by spectroscopies	33
2.2.1.1 Sample preparation	33
2.2.1.2 Characterization	33
2.2.1.3 Computational method	34
2.2.2 Oxygen migration and selective CO and CO <sub>2</sub> formation from epoxidized fullerenes	34
<b>Chapter 3 Results and discussion</b>	<b>35</b>
3.1 Spectral change of simulated X-ray photoelectron spectroscopy from graphene to fullerene	35
3.2 Pyrolysis of epoxidized fullerenes analyzed by spectroscopies	44
3.2.1 Elemental analysis and constructed model structures	44
3.2.2 Mass analysis	46
3.2.3 XPS analysis	48
3.2.3.1 Computational XPS Analysis	48
3.2.3.2 Empirical XPS Analysis	50
3.2.4 DRIFT spectroscopic analysis	53
3.2.5 Distributions of electronic charge	56
3.2.6 Proposed pyrolysis mechanisms of epoxidized C <sub>60</sub>	57
3.2.7 Evidence of an absence of cross-linked C <sub>60</sub>	58
3.3 Oxygen migration and selective CO and CO <sub>2</sub> formation from epoxidized fullerenes	60
3.3.1 Migration of oxygen atom(s)	60
3.3.2 Pyrolysis of one oxygen atom on C <sub>60</sub>	62
3.3.3 Pyrolysis of two oxygen atoms on C <sub>60</sub>	62
3.3.3.1 Two types of intermediates	62
3.3.3.2 Pyrolysis of 2A <sub>1</sub>	64
3.3.3.3 Pyrolysis of 2A <sub>4</sub>	67
3.3.3.4 Comparison for pyrolysis of 2A <sub>1</sub> and 2A <sub>4</sub>	70
3.3.4 Pyrolysis of three oxygen atoms on C <sub>60</sub>	71
3.3.4.1 Three types of intermediates	71
3.3.4.2 Formation of CO and CO <sub>2</sub> gases	73
3.3.4.3 Desorption of O <sub>2</sub> gas	75
3.3.5 Summary of the formation of gases from two and three oxygen atoms on C <sub>60</sub>	76
3.3.6 Comparison with experimental results	77
<b>Chapter 4 Conclusions</b>	<b>78</b>

4.1 Spectral change of simulated X-ray photoelectron spectroscopy from graphene to fullerene	78
4.2 Pyrolysis of epoxidized fullerenes analyzed by spectroscopies	78
4.3 Oxygen migration and selective CO and CO <sub>2</sub> formation from epoxidized fullerenes	78
<b>References</b>	<b>80</b>
<b>List of publications</b>	<b>90</b>
<b>List of presentations</b>	<b>90</b>
<b>List of awards</b>	<b>91</b>
<b>Acknowledgement</b>	<b>92</b>

## Abstract

Nano carbon materials include various defects such as functional groups, pentagons, heptagons, and vacancy defects. These defects affect the electronic, chemical, mechanical, and magnetic properties of graphene. Thus, it is essential to analyze the defects on nano carbon materials in detail. In this study, defects such as oxygen-containing functional groups, pentagons, and vacancy defects were analyzed by empirical and simulated spectroscopies.

First, C1s X-ray photoelectron spectroscopy (XPS) spectra of graphene with two to twelve pentagons were simulated using density functional theory calculation. Peak shifts and full width at half maximum (FWHM) of calculated C1s spectra were applied to actual C1s spectra. Introduction of pentagons shifted the peak top toward low binding energy. The presence of pentagons also influenced FWHM of calculated C1s spectra. Introduction of six pentagons increased the calculated FWHMs from 1.25 to 1.45 eV. These calculated shifts and FWHMs were close to the actual shifts of graphite (284.0 eV) and fullerene (282.9 eV) and FWHMs of graphite (1.25 eV) and fullerene (1.15 eV). By combining the calculated and actual results, we proposed peak shifts and FWHMs of graphene with different numbers of pentagons, which can be utilized for actual XPS analysis.

Second, epoxide was introduced on fullerenes and the epoxidized fullerenes upon heat treatment were analyzed by XPS, infrared spectroscopy (IR), and gas chromatography–mass spectrometry (GC-MS). Epoxide was transformed to C=O and lactone groups at 523 K. Lactone groups were decomposed into CO and CO<sub>2</sub> gases, generating vacancy defects at 673 K. The ratio of decomposed CO<sub>2</sub>/CO gas increased as the amount of epoxides increased.

Third, pyrolysis mechanism of epoxidized fullerenes was estimated by computational calculation. Epoxides were gathered and decomposed into CO and CO<sub>2</sub> gases. From the fullerenes with two epoxides, decomposition of CO gas is energetically favored than that of CO<sub>2</sub> gas. From the fullerenes with three epoxides, decomposition of CO<sub>2</sub> gas is energetically favored than that of CO gas. These results were well matched with those of the empirical study.

## Chapter 1 Background of this research

### 1.1 Nano carbon materials

Nano carbon materials have attracted much attention for a few decades. After discovery of fullerene (Fig. 1-1a) in 1985 [1], carbon nanotube (Fig. 1-1b) in 1991 [2], and graphene (Fig. 1-1c) in 2004 [3], the studies for these materials have been intensively performed. Nano carbon materials can be categorized depending on the bonding state of carbon atoms. For example, graphene, a sheet of  $sp^2C-sp^2C$  networks of carbon atoms, is one layer of graphite, indicating that graphene is macroscopically a 2D structure. Carbon nanotubes with a 1D structure are tubes of graphene. Fullerenes with a 0D structure are a shape of a soccer ball. Diamond (Fig. 1-1d) consists of  $sp^3C-sp^3C$  networks of carbon atoms, indicating that diamond is a 3D structure. Pure nano carbon materials such as graphene and carbon nanotubes consist of mainly hexagons. However, defects such as pentagons and heptagons, vacancy defects, functional groups, and zigzag and armchair edges exist in the actual nano carbon materials (Fig. 1-2). These defects influence the shape as well as various properties such as electronic, mechanical, chemical, and optical properties.

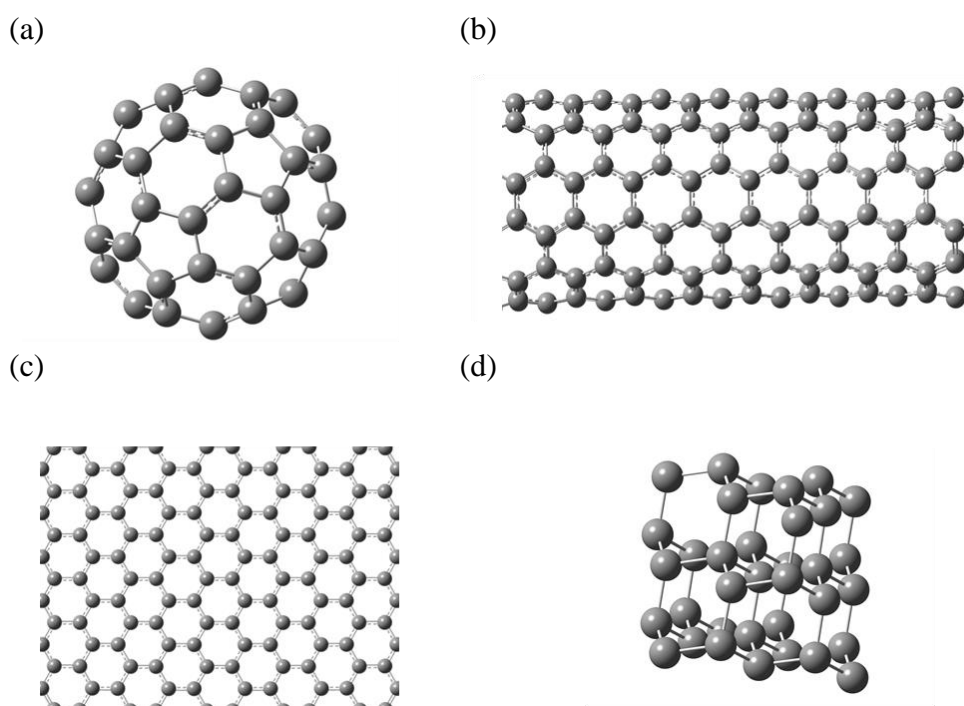


**Figure 1-1** Structures of nano carbon materials. (a) Fullerene. (b) Carbon nanotube. (c) Graphene. (d) Diamond.

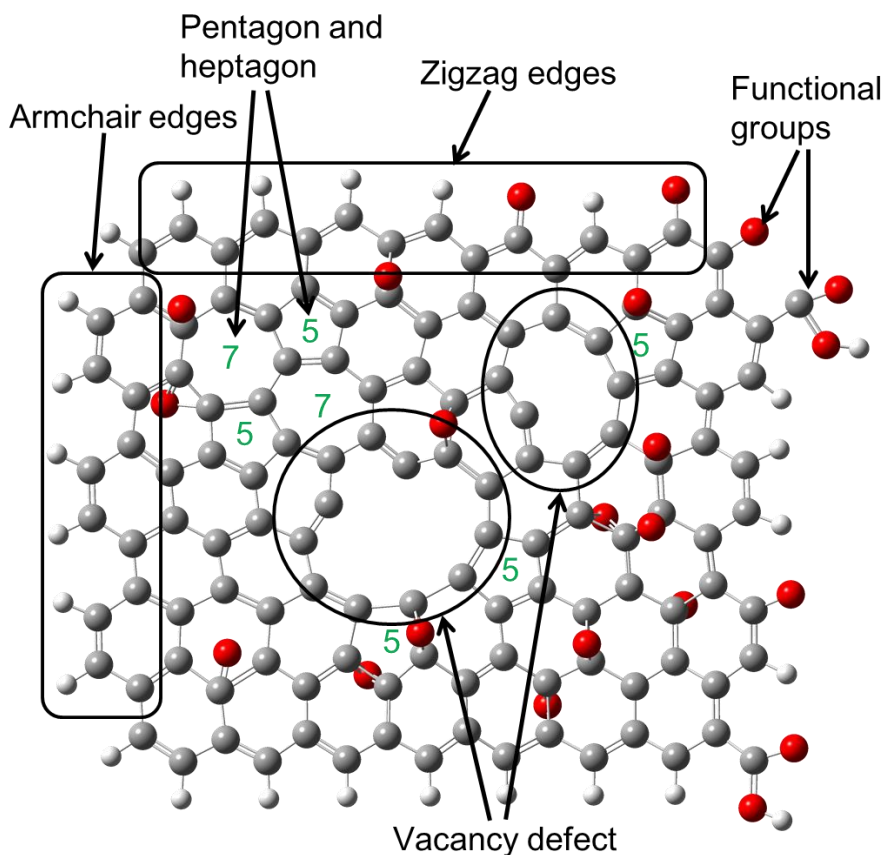


**Figure 1-2** Various types of defects on nano carbon materials.

### 1.1.1 Fullerenes

Fullerenes are hollow carbon shells with ca.  $sp^2C-sp^2C$  bonding. There are many types of fullerenes such as  $C_{60}$ ,  $C_{70}$ ,  $C_{72}$ ,  $C_{76}$ ,  $C_{84}$  and  $C_{100}$ . The most well-known fullerene is a  $C_{60}$  with  $sp^{2.28}C-sp^{2.28}C$  bonding [4], which resembles a soccer ball.  $C_{60}$  consists of 20 hexagons and 12 pentagons (Fig. 1-3), which means the existence of two types of bonding such as hexagon-hexagon bonding (6-6 bonding) and pentagon-hexagon bonding (5-6 bonding). By calculation, the lengths of 6-6 bonding and 5-6 bonding have been reported as 1.39 and 1.45 Å, respectively [5]. Electrons are localized on 6-6 bonding more than on 5-6 bonding [5].

$C_{60}$  contains the lowest unoccupied molecular orbital (LUMO) level ( $t_{1u}$ ) with three-fold degeneration and the highest occupied molecular orbital (HOMO) level ( $h_u$ ) with five-fold degeneration occupied by 10 electrons as shown in Fig. 1-4 [6]. Because of existence of 10 electrons in HOMO, multi-electron reaction such as oxidation proceeds. Moreover, energy level of LUMO of  $C_{60}$  is lower than that of graphene and

single walled carbon nanotubes. The low energy level of LUMO of  $C_{60}$  results in the outstanding performance as electron acceptor [7-10]. These electronic properties indicate that both  $C_{60}$  anion formed by reduction and  $C_{60}$  cation formed by oxidation are exceptionally delocalized compared with other nano carbon materials. The band gap between LUMO and HOMO is 1.8 eV, indicating that  $C_{60}$  is a semiconductor [11].

Regardless of these distinct properties,  $C_{60}$  is not able to be dissolved in almost all of solvents, which means that  $C_{60}$  is intractable. Thus, analysis of the structure, enhancement of properties, and applications to  $C_{60}$  composites are challenging. As a solution for this problem, chemical functionalization has been studied [12-20]. Chemical functionalization increases the solubility in liquid and provides different electronic and optical properties. By functionalization,  $sp^{2.28}C-sp^{2.28}C$  bonding is transferred to  $sp^3 C-sp^3C$  bonding, inducing that the conjugate system disappears. As the representative functionalization of  $C_{60}$ , hydrogenation [12], oxidation [13-15], hydroxylation [16-20], and nitrogenation [21] have been reported.

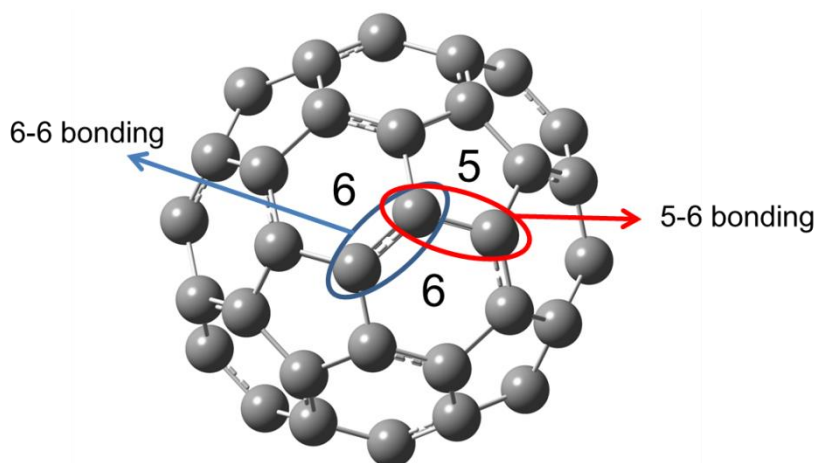


**Figure 1-3** The structure of  $C_{60}$  fullerene.

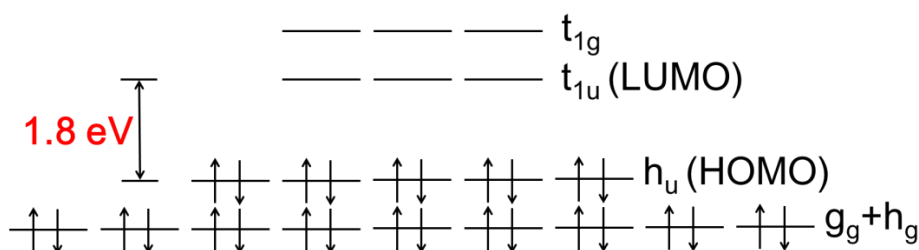


**Figure 1-4** HOMO and LUMO energy levels of  $C_{60}$ .

As the representative methods for synthesis of  $C_{60}$ , arc discharge (Fig. 1-5) and laser evaporation method (Fig. 1-6) have been utilized. Arc discharge evaporates carbon atoms between two carbon electrodes contacted each other in a chamber filled with an inert gas at ca. 4000 K, and  $C_{60}$  are synthesized on carbon electrodes [22,23]. Laser also evaporates carbon atoms from a carbon precursor such as a graphite bar at ca. 1400 K by irradiating a pulse laser under inert gas, and  $C_{60}$  is collected in the trap [24]. The laser evaporation method can synthesize  $C_{60}$  with high selectivity, where the arc discharge method synthesizes  $C_{60}$  with other fullerenes such as  $C_{70}$ ,  $C_{84}$ , and so forth. However, the productivity of  $C_{60}$  by the laser evaporation method is lower than that by the arc discharge method [25].

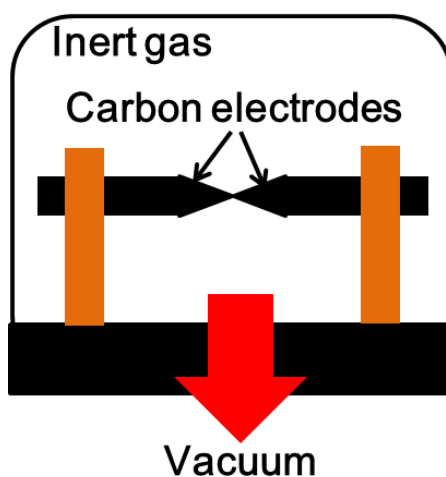


**Figure 1-5** Arc discharge method.

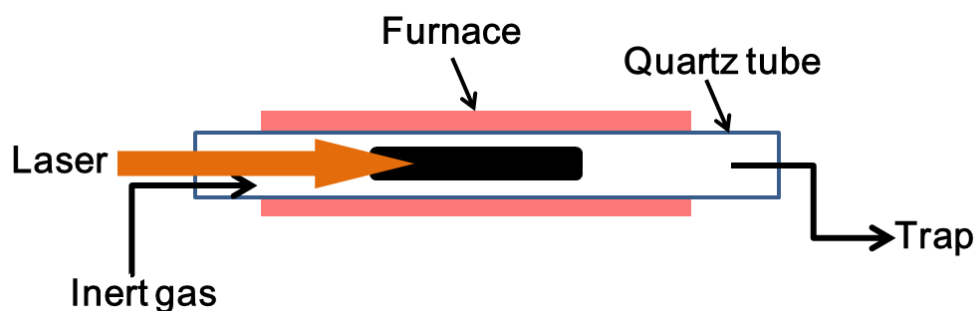


**Figure 1-6** Laser evaporation method.

### 1.1.2 Carbon nanotubes

Carbon nanotubes can be categorized into basically three types such as single walled carbon nanotubes (SWCNTs), double walled carbon nanotubes (DWCNTs), and multi walled nanotubes (MWCNTs). SWCNTs are cylindrical tubes with a single wall with diameters of 0.5-4.0 nm and lengths of several tens of  $\mu\text{m}$  (Fig. 1-7) [26]. The end caps of SWCNTs contain pentagons, which generate curvature. DWCNTs and MWCNTs have one and more layers wrapped around SWCNTs. The diameters of DWCNTs and MWCNTs are 1.2-4.7 and 1.9-100 nm [27], respectively.

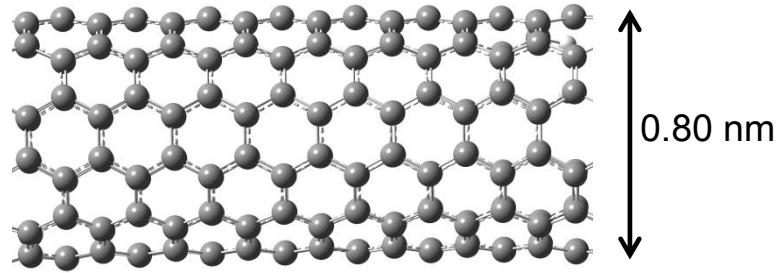


**Figure 1-7** Structure of (12, 0) SWCNT.

Structure of SWCNTs can be expressed using chiral vector ( $C_h$ ) [28]. Figure 1-8 shows that determination of structure of SWCNT using  $C_h$ . The  $C_h$  is defined using unit vector such as  $a_1$  and  $a_2$  using a following equation ( $n$  and  $m$  are constant numbers).

$$C_h(OA) = na_1 + ma_2 \quad (\text{eq. 1-1})$$

$C_h$  is also calculated by a following equation.

$$C_h = 3^{1/2} \times a_1 \times (n^2 + nm + m^2) \quad (\text{eq. 1-2})$$

Diameter of tube ( $d$ ) is calculated using  $C_h$ .

$$d = C_h / \pi \quad (\text{eq. 1-3})$$

Differences of chirality have an effect on the electronic properties of CNTs. For example, CNTs with “ $(n-m) / 3 = \text{constant number}$ ” are metallic and the other CNTs are semi-metallic [29]. Also, optical, chemical, and mechanical properties of CNTs depend on the chirality.

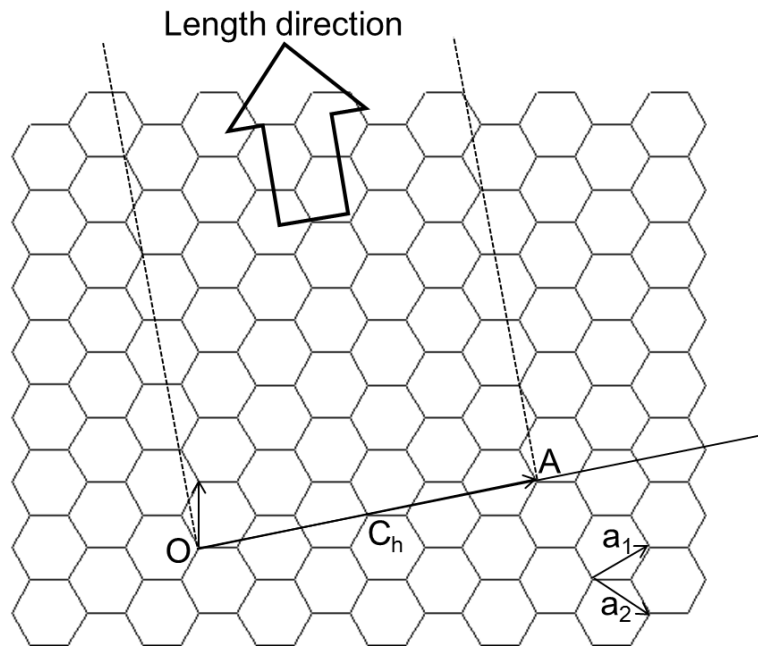


**Figure 1-8** Determination of chirality of SWCNT.  $C_h$  is chiral vector.  $a_1$  and  $a_2$  are unit vector.

Arc discharge, laser evaporation, and chemical vapor deposition (CVD) have been reported for synthesis of CNTs. Methods of arc discharge and laser evaporation are shown in section 1.1.1 (Figs. 1-5 and 1-6). A CVD method (Fig. 1-13) is explained in section 1.1.3.

Peapod is materials of  $C_{60}$  inserted in SWCNTs (Fig. 1-9), which was observed in 1998 by Smith et al [30]. Recently, not only  $C_{60}$  but also other organic and inorganic materials such as sulfur [31-33] and metal [34] have been inserted into SWCNTs. These encapsulations change the properties of SWCNTs, indicating that SWCNTs with different properties can be synthesized for various applications of SWCNTs [31-34]. SWCNTs can also be utilized as a test tube to observe chemical reaction under transmission electron microscope [35,36] and as a capsule to deliver drugs to in-vivo targets [37,38].

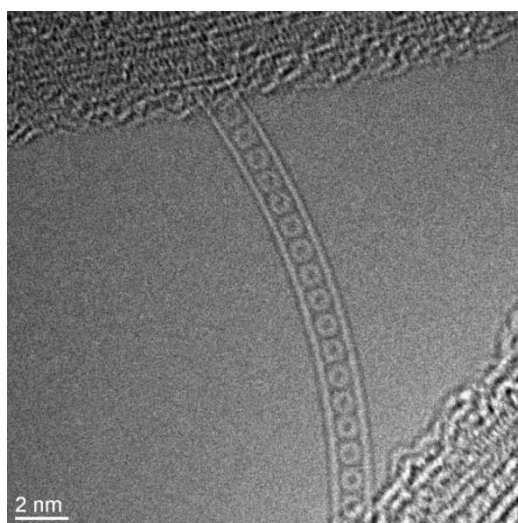


**Figure 1-9** Transmission electron microscopy image of peapod ( $C_{60}$  inserted into SWCNTs).

### 1.1.3 Graphene

The structure of graphene (Fig. 1-10) is one-atom-thick sheet of graphite. The carbon-carbon bond in graphene consists of strong  $sp^2C-sp^2C$  bonding whose length is 0.142 nm [39]. Because of this strong  $sp^2C-sp^2C$  bonding, tensile strength of graphene is the highest in the world [40,41] and chemical stability of graphene is also high. Moreover, pi electrons, which are not involved in  $sp^2C-sp^2C$  bonding, are delocalized on both sides of graphene layer. These pi electrons generate the high electrical conductivity of graphene.

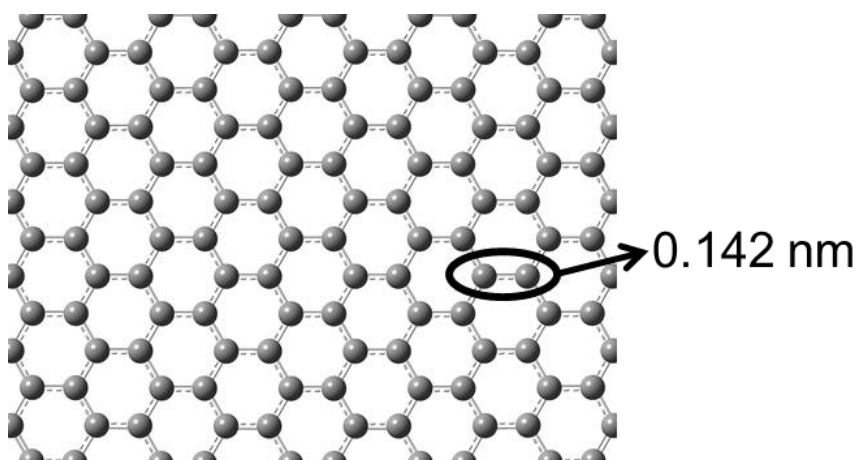


**Figure 1-10** The structure of graphene. The carbon atoms are arranged in the honeycomb structure.

Figure 1-11 shows the band structures of a typical semi-conductor and graphene. The band structure of the typical semi-conductor can be divided into conductance band and valance band. This typical semi-conductor exhibits a parabolic dispersion relation, in which the charge carriers move with some effective mass under electric fields. On the other hands, graphene has a linear dispersion relation around K point [42,43]. This connected point is so called “Dirac point”. Because of its linear band structure, the effective mass of charge is 0, exhibiting the high charge mobility. Although the charge mobility of the typical semi-conductor such as silicon is  $1400 \text{ cm}^2 \text{ Vs}^{-1}$ , that of graphene is  $15000 \text{ cm}^2 \text{ Vs}^{-1}$ . Because of this high charge mobility and the flat structures of graphene, graphene has attracted much attention for application to transistors. However, 0 band gap of graphene causes problems for application to transistors. To solve this problem, syntheses of graphene with narrow width [44,45], double layered graphene [46], graphene with vacancy defects [47,48], and graphene with hetero atoms [49,50] have been conducted.

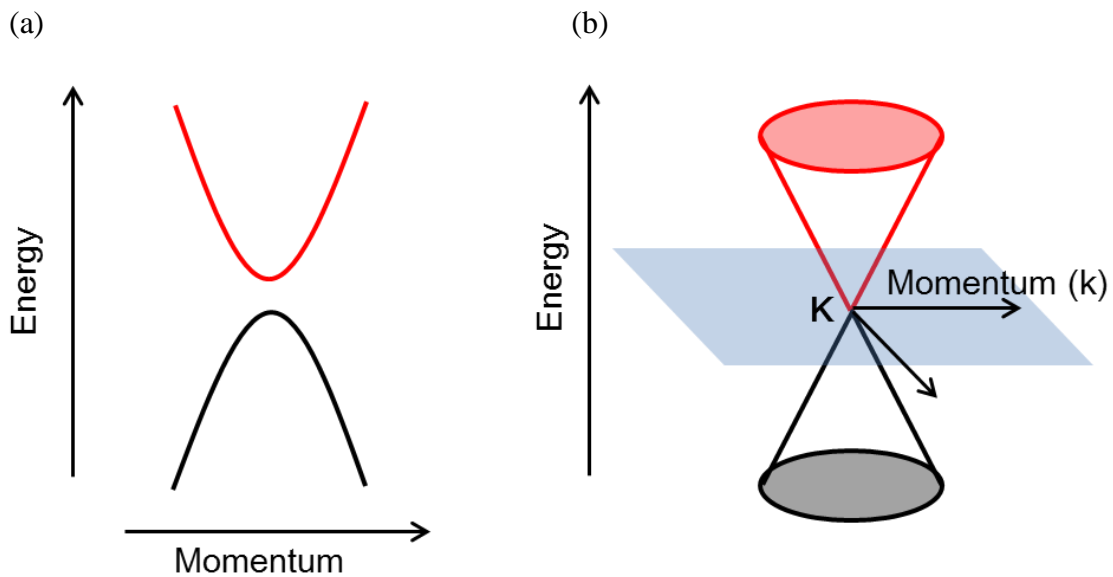


**Figure 1-11** Band structures of a typical semi-conductor (a) and graphene (b).

Four methods such as mechanical exfoliation, epitaxial growth, chemical vapor deposition (CVD), and reduction of graphene oxide (GO) have been reported for preparation of graphene. Mechanical exfoliation is a method for peeling graphene from natural graphite by scotch tape [3]. After transferring graphene from graphite to a substrate such as Si/SiO<sub>2</sub> by scotch tape, the position of graphene can be detected using

microscopes [3]. Graphene prepared by this method has superior structural features such as size with 100  $\mu\text{m}$  or larger, flatness, and small amount of defects. However, the position of graphene on the substrate is arbitrarily pasted by scotch tape, so that it is almost impossible to control the position of graphene pasted on the substrate. Moreover, this method is not suitable for bulk production because of the layer-by-layer peeling method.

The epitaxial growth is a method that graphene is formed from residual graphite on SiC surface after pyrolysis of silica inside SiC (Fig. 1-12) [51,52]. This method utilizes difference in pyrolysis temperature between silica and graphite. The epitaxial method has high repeatability and productivity, indicating this method is suitable to industry. However, it is difficult to obtain the SiC substrate with large size and synthesis cost is high. It is possible to solve this problem by growing thin SiC film on Si substrate by epitaxial growth [53].

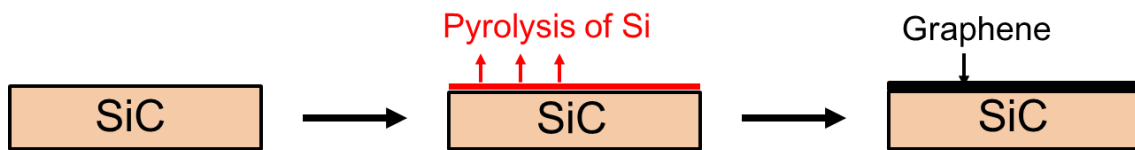


**Figure 1-12** Epitaxial growth mechanism of graphene on SiC.

The CVD method is commonly utilized to synthesize graphene because this method is suitable for synthesizing graphene with a large size, which can be utilized for electronic devices such as transistors [54-60]. Figure 1-13 shows the growth mechanism of graphene by the CVD method. Graphene is synthesized using carbon source on a metal foil as catalyst at 773-1273 K. In detail, the metal foil is reduced under vacuum together with hydrogen flow at 1273 K. Carbon source such as hydrocarbon gas is fed on metal foil at desired temperatures. The structure of graphene synthesized by this method depends on the temperature of synthesis, reaction time of synthesis, and partial pressure of carbon source [54,57,59]. For application to industry, it is necessary to synthesize the graphene at low temperatures. The reason why hydrocarbon gas such as methane gas is utilized for carbon source is low decomposition temperature of hydrocarbon gas. The graphene synthesized on the metal foil by the CVD method should be transferred to other substrates such as other metals and polymers for the following application. One of the transfer methods includes etching of the metal foil by

metal-chelating agents. Another transfer method include direct transfer to polymer substrates without etching of the metal foil for low-price mass production [61]. Graphene tend to be torn apart during transfer process unless it is carefully transferred. Depending on the transferring methods, the tendency of tearing differs.

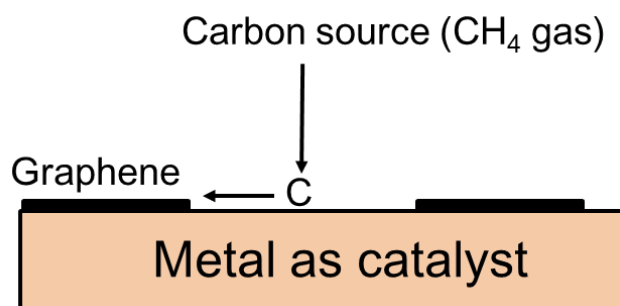


**Figure 1-13** Growth mechanism of graphene by CVD method.

GO is synthesized by oxidizing graphite and exfoliating the oxidized graphite [62-67]. The synthesis method of GO is shown in Fig. 1-14. In detail, oxygen-containing functional groups such as epoxy, hydroxyl, C=O, and carboxyl groups are introduced on graphite by reacting with strong acid such as nitric acid and sulfuric acid in addition to oxidizing agents such as potassium chlorate for synthesis of oxidized graphite, so called graphite oxide. Graphite oxide is rinsed in water to eliminate the residual acid for several times. The oxidized graphite layers are exfoliated to individual layers (GO) by either sonication or heat treatment. Reduction process is necessary to eliminate the oxygen-containing functional groups on surface of graphene. GO is reduced by reacting with the reductant such as hydrazine and reduced graphene oxide (RGO) is prepared. This chemically synthesized graphene is suitable for composite materials because of the mass production of RGO. This method is inexpensive, but various defects remain in the graphene. Synthesis of graphene without defects such as functional groups, pentagons, heptagons, and vacancy defects is challenging.

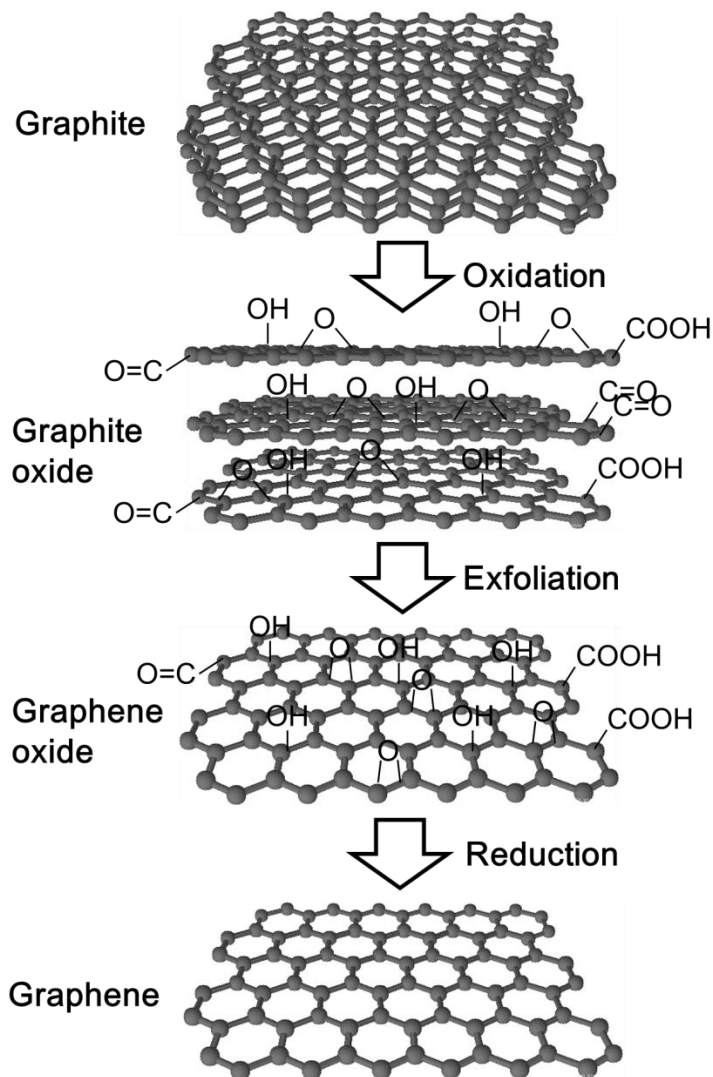


**Figure 1-14** Graphene synthesized from graphite by chemical exfoliation.

### 1.1.4 Characterization

Accurate characterizations of structures of nano carbon materials are necessary for controlling the structures and applying nano carbon materials to industries. Microscopies, spectroscopies, X-ray diffraction [68], and nitrogen adsorption [69,70] have been reported as common techniques for analysis of the structures. Especially, microscopes [71,72] such as transmission electron microscopy (TEM) and scanning tunneling microscope (STM) for direct imaging of the structures (Fig. 1-15) and spectroscopies [73-91] such as infrared spectroscopies (IR), X-ray photoelectron spectroscopy (XPS), and Raman spectroscopy have been utilized for detailed analysis of the defective structures.

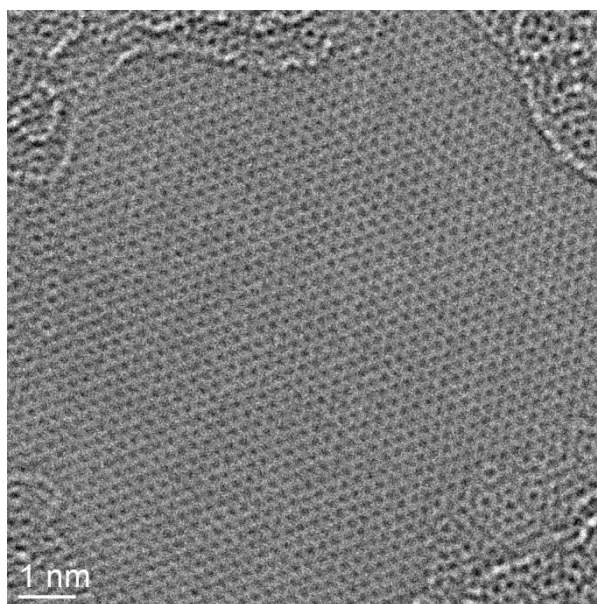


**Figure 1-15** High resolution TEM image of graphene.

## **1.2 Defects in nano carbon materials**

### **1.2.1 Pentagons and heptagons**

Existence of either pentagons or heptagons changes the structure of graphene and CNTs. For example, fullerenes and the end caps of CNTs have curvatures because of the presence of pentagons in the center of five hexagons (Fig. 1-16) [92,93]. Heptagons can form at the saddle-shaped junctions in the SWCNTs [94,95]. It has also been reported that pentagons and heptagons exist in Stone-Thrower-Wales (STW) defects [96], grain boundaries [97], and edges [98] of graphene (Fig. 1-17). Among these defects, the simplest structure is a STW defect. The STW defect is formed at formation energy of ca. 5 eV by rotating one of the C-C bonds in hexagonal lattice without removal and addition of atoms [99,100]. Another common defect is grain boundary. The grain boundary is formed in a graphene sheet because multiple graphene crystals grow on catalysts and those crystals with different orientations bond each other. The grain boundaries containing pentagons and heptagons are necessary to grow one graphene sheet [97]. Edges with pentagons and heptagons have been directly observed by TEM at atomic scale [98] because of the energetic stability of the edges [101].

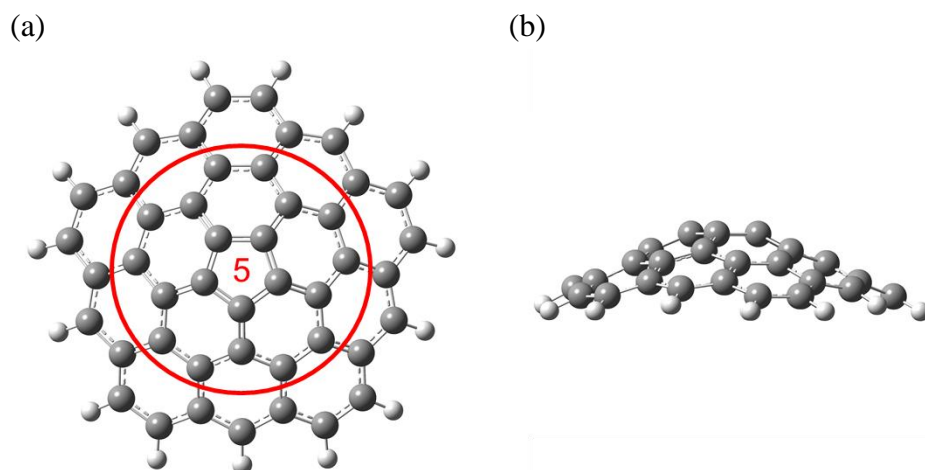


**Figure 1-16** One pentagon surrounded by five hexagons in graphene. (a) Top view. (b) Side view.

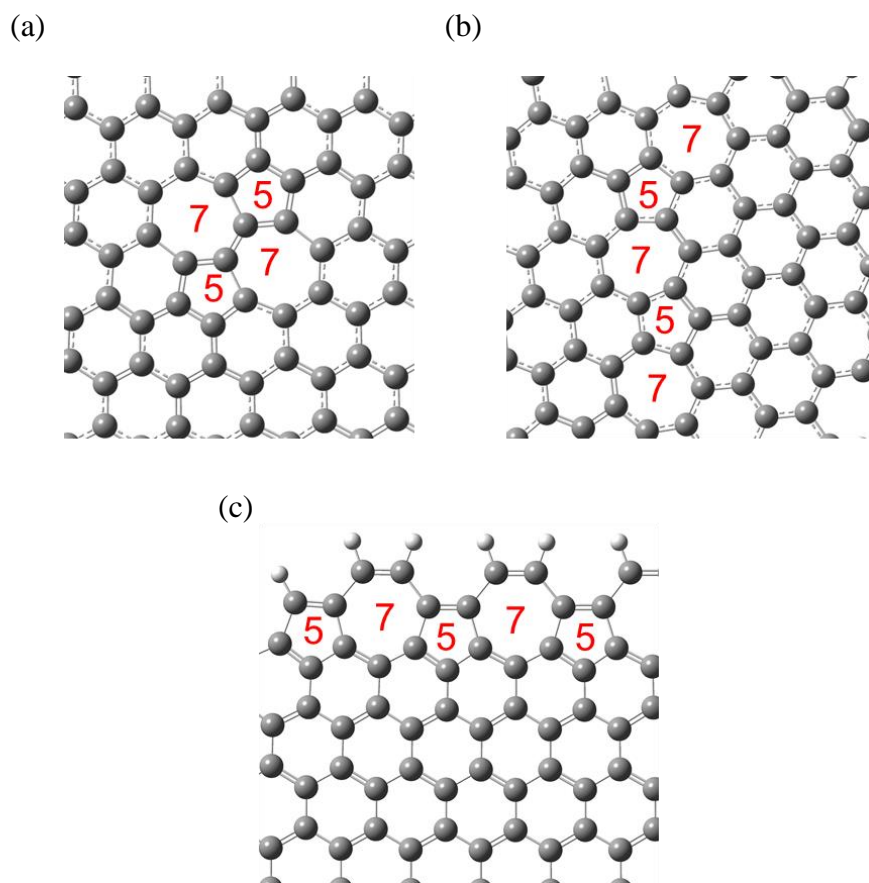


**Figure 1-17** Pentagons and heptagons in graphene. (a) STW defect. (b) Grain boundary. (c) Edges with pentagons and heptagons.

These structural changes generated by the presence of pentagons and heptagons influence mechanical, electronic, and chemical properties of SWCNTs [102-107] and graphene [108-110]. For example, the graphene are easily torn at the grain boundaries, indicating that the presence of pentagons and heptagons decrease the mechanical strength of graphene [40]. The introduction of STW into graphene widens the bandgap, indicating that the presence of pentagons and heptagons influence the electronic properties [106, 111]. The introduction of STW into graphene increases the adsorption of substances as well as the reactivity, indicating that the pentagons and heptagons also influences chemical properties [110].

### 1.2.2 Vacancy defects

Vacancy defects along with pentagons and heptagons are introduced on nano carbon materials during the growth process of nano carbon materials. Although existence of the vacancy defects decreases the mechanical strength of nano carbon materials, introduction of vacancy defects with nanometer size have advantages for applications in industries. For example, introduction of vacancy defect opens the bandgap of graphene for transistors [47,48]. Moreover, graphene with the vacancy defects have also been utilized as gas separators [111,112] and catalyst ligands [113,114]. As the methods for introducing vacancy defects on nano carbon materials, electron [115] and ion irradiation [116] and reaction with oxygen, such as heat treatment under oxygen gas [117], ozone oxidation generated by UV [118], and oxygen plasma treatment [119] have been reported. Because of these advantages of vacancy defects, the structural analysis has also been intensively performed recently.

Mono-vacancy defects (MV) on graphene (Fig. 1-18a) are pentagon-nonagon-hexagon (5-9-6) defects with one electron-rich unstable carbene site, which have been observed by TEM [120,121] as well as STM [122]. Two carbene sites among three carbene sites are bonded each other by Jahn-Teller distortion [123], and one carbene site remains, forming MV defects. The calculated formation energy of MV has been reported to be ca. 7.5 eV [124].

Divacancy defects (DV) on graphene (Fig. 1-18b) are pentagon-octagon-pentagon (5-8-5) defects without any carbene sites. The calculated formation energy of DV is ca. 4.0 eV [124], indicating that the DV is energetically more favored than the MV. It is because of the absence of carbene sites on DV. From DV on graphene, the other defects such as 555-777 and 5555-6-7777 can be formed by rotation of a carbon-carbon bond (Fig. 1-19). The rotation of one of bonds in an octagon in the 5-8-5 defect (Fig. 1-19a) transforms the defect into a structure with three pentagons and

three heptagons (555-777) defect (Fig. 1-19b) [125]. The formation energy of this defect has been reported as ca. 3 eV which is 1 eV lower than that of a 5-8-5 defect. Moreover, one more rotation of one of bonds in a heptagon of the 555-777 defect transforms the defect into a 5555-6-7777 defect (Fig. 1-19c). The formation energy of this defect has been reported as ca. 3.5 eV [125], whose energy is between those of 5-8-5 and 555-777 defects.

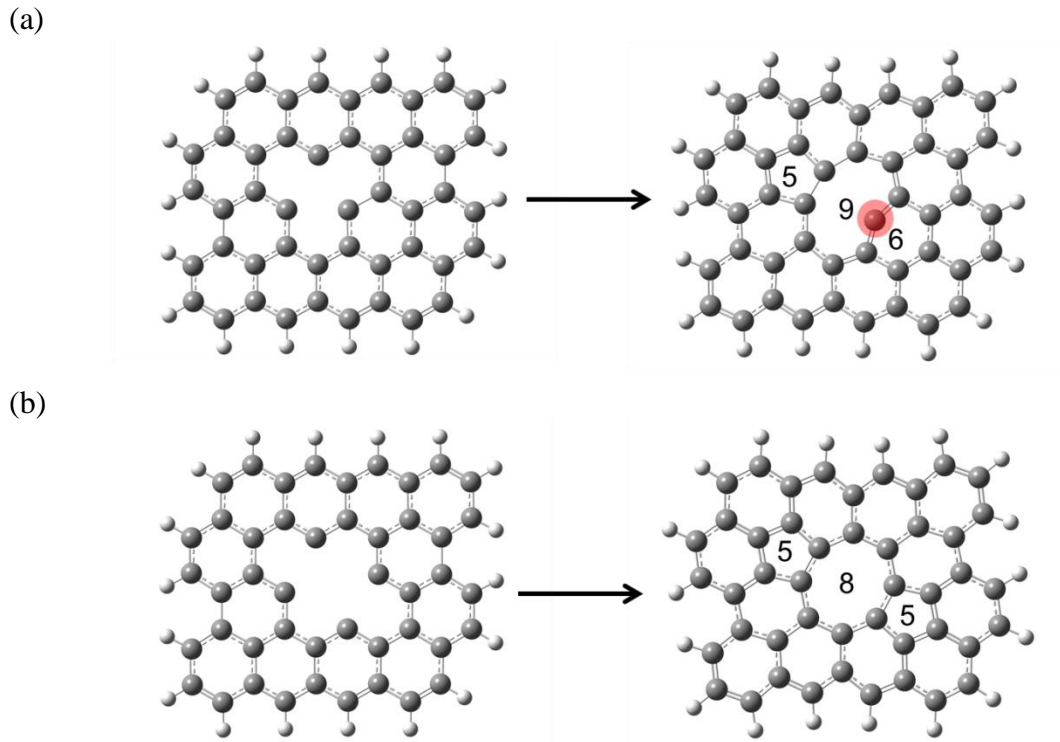


**Figure 1-18** Vacancy defects on graphene. (a) A mono-vacancy defect (5-9-6 defect) before and after optimization of the structure. (b) A divacancy defect (5-8-5 defect) before and after optimization of the structure.

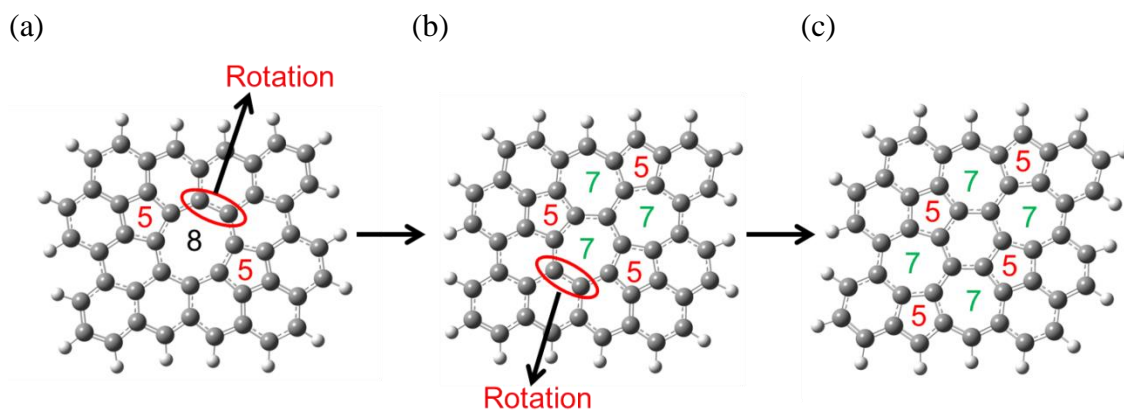


**Figure 1-19** Atomic structures of reconstructed divacancy defect in graphene. (a) 5-8-5 defect. (b) 555-777 defect transformed from the 5-8-5 defect by rotating a C-C bond. (c) 5555-6-7777 defect transformed from the 555-777 defect by another bond rotation.

### 1.2.3 Functional groups

Nano carbon materials such as fullerenes, CNTs, and graphene tend to aggregate because of van der Waals interactions. The agglomerated nano carbon materials cannot easily separate each other. Thus, these nano carbon materials without functionalization are neither soluble nor dispersible in most solvents [126]. The agglomeration complicates the utilization of nano carbon materials for most applications such as composite materials and molecular electronic device. The chemical modification of surface on nano carbon materials increases either solubility or dispersibility of nano carbon materials in various solvents [127-129] because of the presence of hydrophilic oxygen-containing functional groups. These functionalized nano carbon materials have been applied to the electronic device such as biosensors [130,131].

Introduction of functional groups can also change the electronic properties of nano carbon materials [132-137]. Graphene has high electronic conductivity but the zero bandgap of graphene prevent from the application to electronic devices such as sensors using semiconductors. Functionalization of graphene by hetero atoms opens up the bandgap, so that graphene can be used for electronic devices [138]. For example, nitrogen-containing graphene has been reported to have relatively low conductivity and larger on/off ratio [139].

### 1.3 Spectroscopic analysis of defects

Spectroscopic analyses such as IR, XPS, and Raman spectroscopy have been

utilized for characterizing the structure of nano carbon materials with defects such as pentagons, heptagons, vacancy defects, and functional groups. Analysis of defects requires these multiple spectroscopic methods because various possible defects are present in nano carbon materials. The more the number of analytical methods is, the higher the accuracy of the estimated structure of defects become.

### 1.3.1 Infrared spectroscopy

IR has been widely utilized to analyze the defects on nano carbon materials because of the simple and speedy measurement. For example, vacancy defects as well as functional groups such as C–OH, COOH, C=O, epoxy, alkoxy, C–N, C–ONH, and C–H on graphene have been analyzed by IR (Table 1-1) [73-78]. Especially, the detection of vacancy defects such as mono- and divacancy defects has been studied using simulated and experimental IR analysis of graphene oxide [74]. Although various defects of graphene have been gradually revealed by simulated and experimental IR analysis, the peak assignments for determining the defects only by IR are extremely challenging and almost impossible because many peaks are overlapped each other as shown in Table 1-1. Thus, characterization of defects on nano carbon materials requires combination of multiple analytical techniques.

**Table 1-1** Reported assignment of defects on graphene using IR

<b>Defects</b>	<b>Wavenumber / cm<sup>-1</sup></b>
C=C aromatic rings (without defect)	1577 [73], 1500-1600 [74,75], 1622 [76]
C–H	2854, 2925 [77]
C–O carboxylic	1416 [79]
C=O carboxylic	1600–1650, 1725 [78]
Epoxy	1070 [74], 1230 [76]
C–O Alkoxy	1060 [76]
C–OH hydroxyl	3000–3600 [78], 3000–3700 [74]
<u>C=ONH</u>	1653 [77]
C–N	1350 [76]
Mono-vacancy defects	804, 974, 1122, 1159, 1296 [74]
Di-vacancy defects	1067, 1104, 1237 [74]

### 1.3.2 X-ray photoelectron spectroscopy

XPS is a potent qualitative and quantitative surface characterization technique

because of high sensitivity of XPS. XPS has an ability to determine chemical state information within nanometer-scale depth ( $\leq 10$  nm). Thus, XPS is an ideal technique for investigating the types and amounts of defects of nano carbon materials.

The assignments of defects such as functional groups, vacancy defects, and pentagons using XPS have been experimentally revealed owing to the efforts of many researchers [79-85]. For example, oxygen-containing functional groups on nano carbon materials have been intensively analyzed by XPS. Only up to four peaks originating from C=C, mono-(C–O), di-(C=O, O–C–O), and trioxygenated carbon (COO) have been mainly utilized for the waveform separation of C1s spectra [79-82]. However, more than three types of functional groups in addition to C=C should exist on nano carbon materials. Thus, techniques to clarify the difference of many types of functional groups are essential for analyzing the structure.

Larciprete et al. conducted further detailed waveform separation using seven peaks including vacancy defects, C=C, C–C in the close vicinity of chemisorbed O atom, C–O–C in-plane ether, epoxide, C=O, and O–C=O on graphene. Also, an O1s spectrum was separated into four peaks such as C=O, C=O in different surroundings, epoxides, and C–O–C [80]. In addition to the functional groups, XPS analysis of pentagons on graphene has been also reported [81-83]. Point defects including one pentagon in graphene have been analyzed and the peak originating from pentagons was negatively shifted to -0.8 eV from a peak originating from carbon atoms on hexagons [81]. As another example, peak shifts of carbon atoms on a pentagon in MV(-1.10 ~ -0.37 eV), DV (-1.18 ~ -0.34 eV), and a STW defect (-0.94 eV) from the peak top of a C=C peak of graphene has been reported [82]. The references of peak shifts from the peak top of a C=C peak in C1s XPS spectra for various defects on graphene are summarized in Table 1-2.

**Table 1-2** Reported C1s XPS peak assignments of various defects on graphene.

<b>Defects</b>	<b>Peak shifts from a C=C peak / eV</b>
Ether	0.9-1.2 [80]
C–OH, Epoxy	1.9 [80], 2.0 [84], 2.1 [85]
C=O	3.4 [84], 3.5 [85]
COO	4.4 [85], 4.7 [84]
C–N	1.3 [84]
Vacancy defects	-1.1 [80], -0.8 [81]
STW defects	-0.1 [82]

### 1.3.3 Raman spectroscopy

Raman spectroscopy is especially sensitive to  $sp^2$  and  $sp^3$  carbon-carbon bonds of nano carbon materials. All of bands in the Raman spectrum corresponds to a specific vibrational frequency of a bond in the structures. The main band of Raman spectra of graphite with  $sp^2C-sp^2C$  bonds and diamond with  $sp^3C-sp^3C$  bonds appears ca.  $1580\text{ cm}^{-1}$  and ca.  $1330\text{ cm}^{-1}$ , respectively. The band at ca.  $1580\text{ cm}^{-1}$  is so called G band, originated from quadrant stretch of  $sp^2C-sp^2C$  bonds [86,87]. The band at ca.  $1360\text{ nm}^{-1}$  is so called D band, originated from ring breathing mode/in-phase ring stretch and intervalley scattering associated with graphene edges [88,89]. The presence of D band indicates the presence of disorder on the nano carbon materials. This band is often referred to as the disorder band and the intensity of the D band relative to that of the G band is often used as a measure for a degree of defects on nano carbon materials.

An intensity ratio of two main bands at ca.  $1580\text{ cm}^{-1}$  (G band) and  $2700\text{ cm}^{-1}$  (2D band) of graphene has been reported to be a measure to determine the number of graphene layer. Mono-layered graphene, double-layered graphene, and multi-layered graphene has been reported to show 3 or more, 1-2, 1 or less of the value of 2D/G band, respectively [90].

The number of graphene layer can also be estimated by the full width at half maximum (FWHM) of 2D band. The FWHM of 2D band of mono layered graphene spectrum is  $25\text{ cm}^{-1}$ , which is almost half of FWHM of the 2D band of graphite. It indicates that the 2D band of mono-layered graphene spectrum fits to a single band, whereas that of multi layered graphene spectrum fits to several bands [90]. These bands are generated as a result of the different interlayer interactions occurred at different depths within the graphene [90]. The number of graphene layer can also be estimated by the Raman shift ( $\text{cm}^{-1}$ ) of 2D band. The difference in peak shift between mono-layered and multi-layered graphene is caused by interactions between the stacked graphene layers. The Raman shift of 2D band of mono-layered graphene is  $20\text{ cm}^{-1}$  higher than that of multi-layered graphite.

The characteristic mode of Raman spectrum for SWCNTs is radial breathing mode (RBM) appeared at ca.  $200\text{ cm}^{-1}$ . The RBM bands correspond to the expansion and contraction of the tubes. Diameter of SWCNTs can be estimated by dividing 248 by the Raman shift of the actual RBM band [91]. This equation can change depending on the separated or aggregated SWCNTs. Another feature of spectra for SWCNTs is separation of G band to G+ and G- (Breit-Wigner-Fano) band. G+ band is shifted at  $1590\text{ cm}^{-1}$ , but the G- band is shifted to different frequency depending on the structures of SWCNTs. The frequency of G- band in Raman spectrum of metallic nanotubes is

shifted to  $1550\text{ cm}^{-1}$ , whereas that of semi-metallic nanotubes is shifted to  $1580\text{ cm}^{-1}$  [88], indicating that G band in Raman spectrum of metallic nanotubes is separated into two clear bands. The main feature in the  $C_{60}$  spectrum is a relatively sharp line at around  $1469\text{ cm}^{-1}$ , known as the pentagonal pinch mode [140].

#### **1.4 Density functional theory calculation**

Structures of defects with atomic size on nano carbon materials could be fully understood only if empirical and computational analyses were combined because current technology has not achieved to analyze the defective structure completely using only empirical approach. Density functional theory (DFT) has been commonly utilized in computational simulation because of its efficiency in time cost and accuracy of calculation. Various calculations such as geometry optimizations, vibrational analysis, and population analysis can be conducted using DFT. Through these simulations, reaction mechanism [141,142] and simulated XPS [80-83], Raman [143], IR [74,75,78], and UV-Vis spectra [62] can be calculated.

#### **1.5 Purpose of this study**

In this study, introduction and characterization of defects on nano carbon materials were investigated. This study is comprised of three following objects. The first object is analysis of pentagon-containing graphene by XPS. C1s XPS spectra of graphene with two to twelve pentagons were simulated using DFT calculation. The second one is introduction of epoxide on fullerenes and characterization of the epoxidized fullerenes upon heat treatment by spectroscopies. The third one is estimation of pyrolysis mechanism of epoxidized fullerenes upon heat treatment by DFT calculation.

##### **1.5.1 Spectral change of simulated X-ray photoelectron spectroscopy from graphene to fullerene**

Graphene has received enormous attention because of various possible applications such as electronic devices and catalyst supports [144]. The presence of pentagons in graphene changes the morphology [108], electronic states [109], and reactivity of graphene [110]. Quantitative information such as the number of pentagons per area (i.e. areal density) in graphene and qualitative information such as closeness of pentagons are essential to understand such electrical and chemical properties.

Pentagons have been analyzed by several methods such as high resolution TEM (HRTEM) [145] and Raman [146], IR [147], and nuclear magnetic resonance

(NMR) [148] spectroscopies. For example, pentagons have been directly observed at grain boundaries of graphene and defective structures of reduced graphene oxide by HRTEM [145], but electron irradiation during observation may cause the structural change and prevent from observing correct structures. Raman and IR spectroscopies have been utilized to determine vacancy defects and STW defects in graphene [146,147], but the peaks solely analyzing pentagons have not been reported other than fullerenes. In addition, Raman and IR have disadvantages in quantitative analysis. Conventional solid-state NMR spectroscopy requires the large amount of samples for measurement, which is not suitable for analyzing precious nano materials. Thus, it is urgent to develop other analytical techniques.

XPS analysis can be one of suitable techniques to analyze graphene with pentagons quantitatively and qualitatively. Most research groups have separated the main peak of C1s spectra of graphene as  $sp^2C$  and  $sp^3C$ , and neglected the analysis of detailed states of bonding of graphene. In terms of fullerene containing pentagons, the peak position of C1s spectra has been reported, but the peak originating from pentagons of fullerenes has not been separated from hexagons because all pentagons connect with hexagons [15,150]. Because of the difficulty to synthesize such reference compounds currently, computational simulation is necessary as one of the tools to investigate the structure clearly.

Computational simulations of XPS spectra of graphene-related materials have been recently utilized to clarify the defective structures [78,81,82,151-156]. Since Proctor and Sherwood [151] and Boutique et al. [152] have started computational analyses of functional groups on carbon materials in the 1980s, several groups have reported assignments of defective structures of graphene-related materials using calculation [78,82,153-156]. However, XPS analysis of pentagons on graphene has not been reported except three papers [81-83] to the best of our knowledge. For example, point defects including one pentagon in graphene have been analyzed and the peak originating from the pentagon was negatively shifted to -0.8 eV from a peak originating from carbon atoms on hexagons [81]. As another example, peak shifts of carbons on pentagon in single vacancies (from -1.10 to -0.37 eV), double vacancies (from -1.18 to -0.34 eV), and STW defects (-0.94 eV) from a  $sp^2C$ - $sp^2C$  peak of graphene has been reported [82]. These works showed only the peak shifts originated from the presence of either one or two pentagons in graphene, and influence of the number and closeness of pentagons on peak shifts as well as the FWHM were not mentioned.

Our group has demonstrated the effects of defects such as functional groups and STW defects on FWHMs and shifts of XPS spectra [83,157]. Electron-withdrawing

groups such as C=O and C-CN have large effects on shifts of main peaks as well as the increment of FWHMs. Pentagons have a similar role to C=O and C-CN because of their electron-withdrawing nature [158]. It is possible that the presence of pentagons also affect shifts of main peaks as well as FWHMs.

In this work, the number of pentagons was increased in the basal plane of graphene and the effect of the number and position of introduced pentagons on C1s shifts and FWHMs was analyzed by computational simulation of C1s XPS spectra. Especially, isolated pentagons and connected pentagons in graphene generated the different peak shifts each other.

### **1.5.2 Pyrolysis of epoxidized fullerenes analyzed by spectroscopies**

The defects such as functional groups and vacancy defects on nano carbon materials are well-known as one of the major issues for mechanical, chemical, and electrical properties of nano carbon materials [159]. It is important to study mechanisms of defect formations in the basal plane of nano carbon materials in order to fully understand, improve, and control these properties [142,160,161]. Especially, oxidation is among the simplest and historically the most important approaches for introducing functional groups and vacancy defects in nano carbon materials [117,142,160-163].

The most common oxidation method of nano carbon materials to introduce vacancy defects in the basal plane of nano carbon materials is heat treatment under oxygen and ozone gas [15,117,164]. This one-step oxidation reaction is currently still favored because of the simplicity and the cost-effectiveness. But this one-step treatment basically involves mainly three mechanisms such as chemisorption of oxygen molecules [165,166], migration of oxygen atoms [167,168], and pyrolysis of oxygen-containing functional groups such as epoxides and lactone groups [169,170], leaving vacancy defects in the basal plane of nano carbon materials. In addition, van der Waals interactions among contacting nano carbon materials in the form of powders cause diffusion-limited region for the oxygen gas. The non-uniform reaction cannot be avoided unless single-layered graphene and single-walled carbon nanotubes without overlapping and bundling are utilized [117], respectively. Fullerenes are crystals which have face-centered cubic close-packed structures [171], which cause difficulty to react uniformly with the oxygen gas. The multiple mechanisms and non-uniform reactions cause difficulties to analyze each mechanism in detail.

Epoxidation of fullerenes in a solvent is, on the other hand, one of the simplest uniform liquid-phase reactions for fullerenes [13,14]. Because epoxidation of fullerenes can be conducted at much lower temperature (ca. 343 K) than oxidation of fullerenes by

the oxygen gas (above 473 K), this reaction temperature avoids the severe migration of oxygen atoms in the basal plane. Thus, the epoxidation reaction is an effective approach to separate the one-step method involving multiple mechanisms into two mechanisms.

One of the separated mechanisms is epoxidation. Even with this simple epoxidation reaction, various functional groups are formed as shown in this work. Organic chemists commonly discuss selectivity of reactions, which indicates the percentage of transformation of structures from a raw material into an aiming compound. The same concept can be applied to the functional groups on nano carbon materials such as fullerenes. Because of the presence of these multiple functional groups on fullerenes, it is essential to clarify the types of functional groups accurately.

Another separated mechanism is migration and pyrolysis of oxygen-containing functional groups. Migration of one epoxide in the basal plane of graphene has been reported in detail [167,168,170]. Migration of one epoxide occurs at ca. 94.1 kJ mol<sup>-1</sup> of activation energy [168]. The presence of one epoxide close to another epoxide reduces the total electron energy comparing to two isolated epoxides, so that epoxides tend to be gathered [170]. Upon heat treatment of two epoxides in the basal plane of graphene, one O<sub>2</sub> gas is formed [170]. Upon heat treatment of three epoxides, lactone and ketone groups are formed and CO and CO<sub>2</sub> gases generate [170]. This second mechanism including migration and pyrolysis of epoxidized fullerene also involve changes of functional groups upon heat treatment, so that the techniques to analyze the functional groups in detail are required.

XPS and IR have been utilized to analyze nano carbon materials with oxygen-containing functional groups [161,172-174]. For example, fullerenes with oxygen-containing functional groups have been analyzed by XPS. Only up to four peaks originating from C=C, mono- (C-O), di- (C=O), and tri-oxygenated carbon (O-C=O) have been mainly utilized for the waveform separation of C1s spectra [172-174]. However, more than three types of functional groups should be formed upon heat treatment. Thus, techniques to clarify the difference of many types of functional groups are essential to determine the mechanisms for pyrolysis of epoxidized fullerenes. Since analysis of nano carbon materials by only one spectroscopy technique is not reliable [83], IR spectroscopy should be combined with XPS. Fullerenes with oxygen-containing functional groups have also been analyzed using IR spectroscopy, and several functional groups such as ether, epoxy, C=O, and hydroxyl groups have been assigned [174,175]. But defective structures of fullerenes could be revealed more precisely by comparing with the results of computational simulations.

Since Proctor and Sherwood have started computational analysis of functional

groups on carbon fibers for XPS using small aromatic molecules [151], computational analyses of defective structures including oxygen-containing functional groups of carbon materials have been developed [83,81]. Computational analysis is necessary especially for the fine analysis of XPS spectra. But most of the modelled molecules used in the prior work are either small molecules [151] or relatively large graphene sheets with terminated hydrogen atoms and without pure pentagons [83]. The presence of hydrogen atoms and pentagons should influence XPS and IR spectra. For fine analysis of pyrolysis of epoxidized fullerenes, the utilization of whole fullerene molecules is necessary to reveal structures of defective fullerenes in detail.

In this work, defects such as oxygen-containing functional groups and vacancy defects were introduced on fullerenes by epoxidation and heat treatment. The defective structures were analyzed by combination of spectroscopic and computational methods.

### **1.5.3 Oxygen migration and selective CO and CO<sub>2</sub> formation from epoxidized fullerenes**

Oxidation is one of the most effective approaches to introduce vacancy defects at the end caps of CNTs [176-181]. CNTs with such open end caps have been utilized as test tubes to observe movements of molecules by microscopes [30,182-186] and electrodes of electric double layer capacitors [163], whereas the mechanisms for opening end caps are still under investigation. Fullerenes have similarity to end caps of CNTs because of the pentagons. Because the area of end caps of CNTs is small compared to that of CNT wall, analyses of end caps of CNTs are difficult, whereas pyrolyzed fullerenes with epoxides show clear difference in the results of X-ray photoelectron spectroscopy and IR [150]. Thus, analyses of fullerenes are essential to understand hole-opening mechanisms of the end caps of CNTs.

Hole-opening of the basal plane of graphene and the wall of CNTs has been reported empirically [117,163,176-181] and theoretically [167,187-189]. It has been understood that the hole-opening mechanisms involve mainly three mechanisms such as chemisorption of oxygen molecules, migration of oxygen atoms in the form of epoxides, and pyrolysis of oxygen-containing functional groups [142,145,160,161,169,190]. An activation energy required for migration of one epoxide in the basal plane of graphene has been reported to be ca. 94.1 kJ mol<sup>-1</sup>, indicating that epoxides migrate even at a low temperature [168]. The migrated epoxides gather to minimize the energy, forming other functional groups such as lactone and ketone groups [170]. These functional groups are decomposed and CO and CO<sub>2</sub> gases are released at an elevated temperature [169].

All of these hole-opening mechanisms of graphene-based materials containing

only hexagons have been discussed, whereas mechanisms of pyrolysis of epoxidized fullerenes containing pentagons have not been reported in detail. The only report that I have found is the heat treatment of fullerenes in an O<sub>2</sub> gas which has been studied by Wohlers et al [15]. The heat treatment of fullerenes in the O<sub>2</sub> gas involves mechanisms such as chemisorption of O<sub>2</sub> molecules, transformation from oxygen atoms to either an epoxide or a ketone group, and the formation of CO and CO<sub>2</sub> gases at 570 K [15]. Since it has been reported that oxygen atoms migrate in the basal plane of graphene [165,168] and unzip the C-C bond [167,188,189,192], it is expected that the migration of oxygen atoms and unzipping of C-C bond may also occur on C<sub>60</sub> fullerene.

Contrary to the relatively simple mechanisms proposed by Wohlers et al. [15], I have empirically demonstrated more detailed mechanisms such as the formation of ketone and lactone groups generating CO and CO<sub>2</sub> gases by pyrolysis of epoxidized C<sub>60</sub> [150]. I have also empirically shown that the ratio of the CO<sub>2</sub> gas to the CO gas increased as the coverage of oxygen atoms on C<sub>60</sub> increased. However, I have not shown the detailed mechanism theoretically. It is expected that understanding mechanisms for migration of oxygen atoms and the formation of CO and CO<sub>2</sub> gases on C<sub>60</sub> will lead to further control the size and the structure of vacancy defects at end caps of CNTs.

In this work, activation and formation energies for migration of oxygen atoms and transformation of oxygen-containing functional groups upon pyrolysis of epoxidized C<sub>60</sub> were calculated using computer simulations based on DFT.

## Chapter 2 Experimental

### 2.1 X-ray photoelectron spectroscopy of fullerene related materials

#### 2.1.1 Spectral change of simulated X-ray photoelectron spectroscopy from graphene to fullerene

##### 2.1.1.1 Simulation of X-ray photoelectron spectroscopy

Graphene terminated with hydrogen atoms on zigzag and armchair edges ( $C_{100}H_{26}$ ) was constructed (Fig. 2-1) as a basic structure in this work. The introduced positions of pentagons and the numbering of the positions are indicated in the structure. Structures used in this work are shown in Fig. 2-2. Zero (Fig. 2-2a), two (Fig. 2-2b), four (Fig. 2-2c), six (Fig. 2-2d), and eight pentagons (Fig. 2-2e) were introduced in the basal plane of graphene. Peak positions and FWHMs of XPS spectra of isolated pentagons such as two (Fig. 2-2b) and four (Fig. 2-2c) pentagons in graphene and connected pentagons such as six (Fig. 2-2d) and eight (Fig. 2-2e) pentagons in graphene were estimated to determine whether isolated pentagons or connected pentagons. For comparison,  $C_{60}$  fullerene with twelve pentagons (Fig. 2-2f) was also used. These structures include mainly three types of carbon atoms such as C1 ( $sp^2C-sp^2C$ ) on hexagons, C2 ( $sp^2C-H$ ), and C3 (pink spheres) on pentagons (Fig. 2-2b-f).

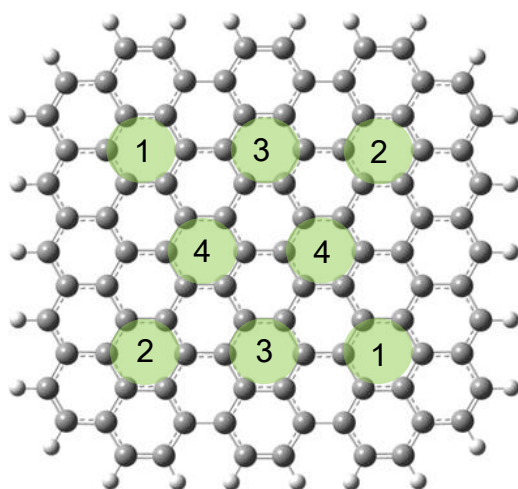


**Figure 2-1** Positions of introduced pentagons and the numbering of the positions in graphene terminated with hydrogen atoms. Two pentagons : Position 1. Four pentagons: Positions 1 and 2. Six pentagons: Positions 1, 2, and 3. Eight pentagons: Positions 1, 2, 3, and 4.

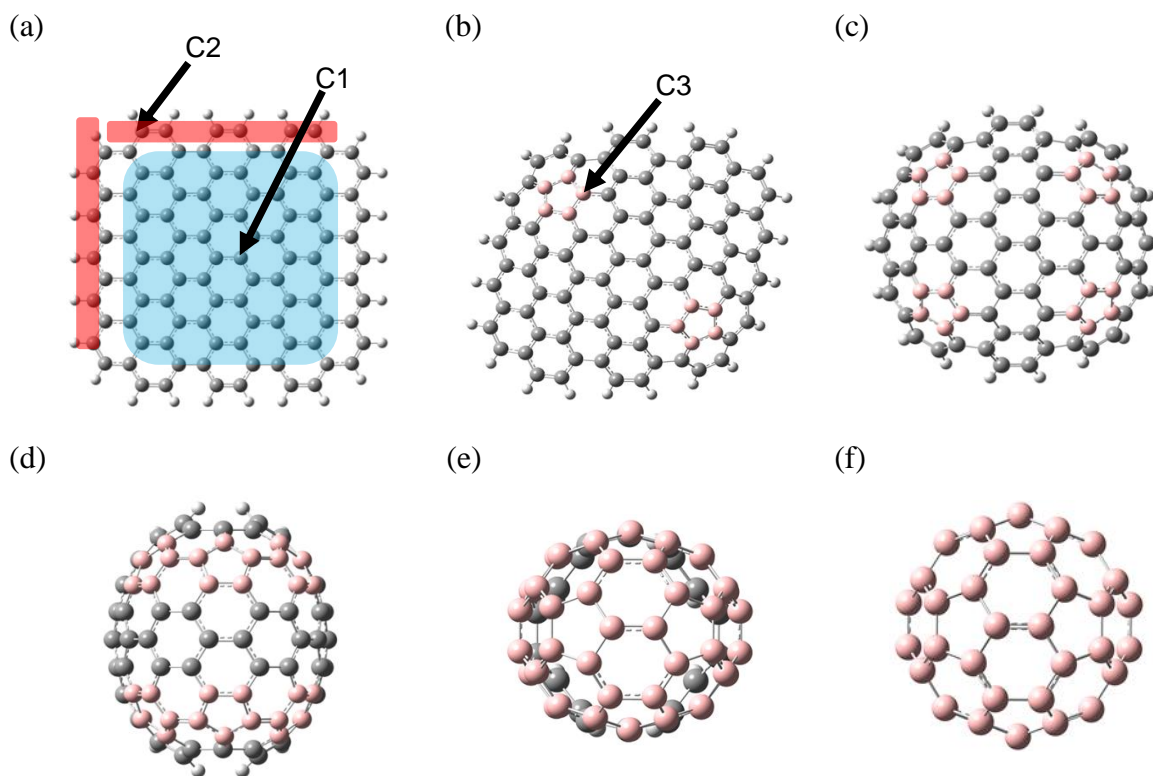


**Figure 2-2** Optimized structures of graphene, pentagon-containing graphene, and fullerene. All the edges were terminated with hydrogen atoms (white sphere). C1 is carbon atoms on hexagons which bonded with carbon atoms. C2 is carbon atoms bonded with hydrogen atoms. C3 is carbon atoms on pentagons (pink spheres). (a) Graphene terminated with hydrogen atoms. (b) Two pentagons. (c) Four pentagons. (d) Six pentagons. (e) Eight pentagons. (f) Twelve pentagons without hydrogen atoms (Fullerene).

All of the following calculations were conducted using B3LYP/6-31g(d) integral=grid=ultrafine of Gaussian 09 [193]. After the structures were optimized, population analyses for simulated XPS spectra using the keyword of pop=full gfpint were conducted. Charge was set as either 0 or 2, but charge was normally equal to 0 unless stated. Spin multiplicity was set as 1 for all calculations. Binding energies of these model structures were directly obtained from the orbital energy using an approximation based on the modified Koopmans theory [194] calculating from the highest occupied molecular orbital (HOMO) level to each orbital. For simulating C1s spectra using the calculated binding energy, the scaling factor of 1.038, obtained from

the actual value of graphite (284.0 eV from Fermi level) divided by the calculated value of graphene terminated with hydrogen atoms (273.7 eV from HOMO level), was multiplied to all of calculated binding energies to compensate for the difference between the calculated and the actual binding energies. The number of orbitals was counted every 0.05 eV to simulate C1s spectra (Fig. 2-3). Furthermore, modified asymmetric Voigt-type lineshape [195] was applied to obtain simulated XPS spectra which resemble actual XPS spectra. (Fig. 2-4a and b). Different values of ratio of Lorentzian function to Gaussian function ( $m$ ) calculated from following equation was applied to XPS spectrum of each structure (Fig. 2-4c).

$$m = \text{Lorentzian function} / (\text{Lorentzian function} + \text{Gaussian function}) \quad \text{eq.1}$$

Different values of asymmetry factor ( $\alpha$ ) were also applied to XPS spectrum of each structure (Fig. 2-4c). All of the maximum intensities of C1s spectra were adjusted at 1.0 for fair comparisons. The number of electrons of carbon atoms in each structure was obtained using the Mulliken population analysis.

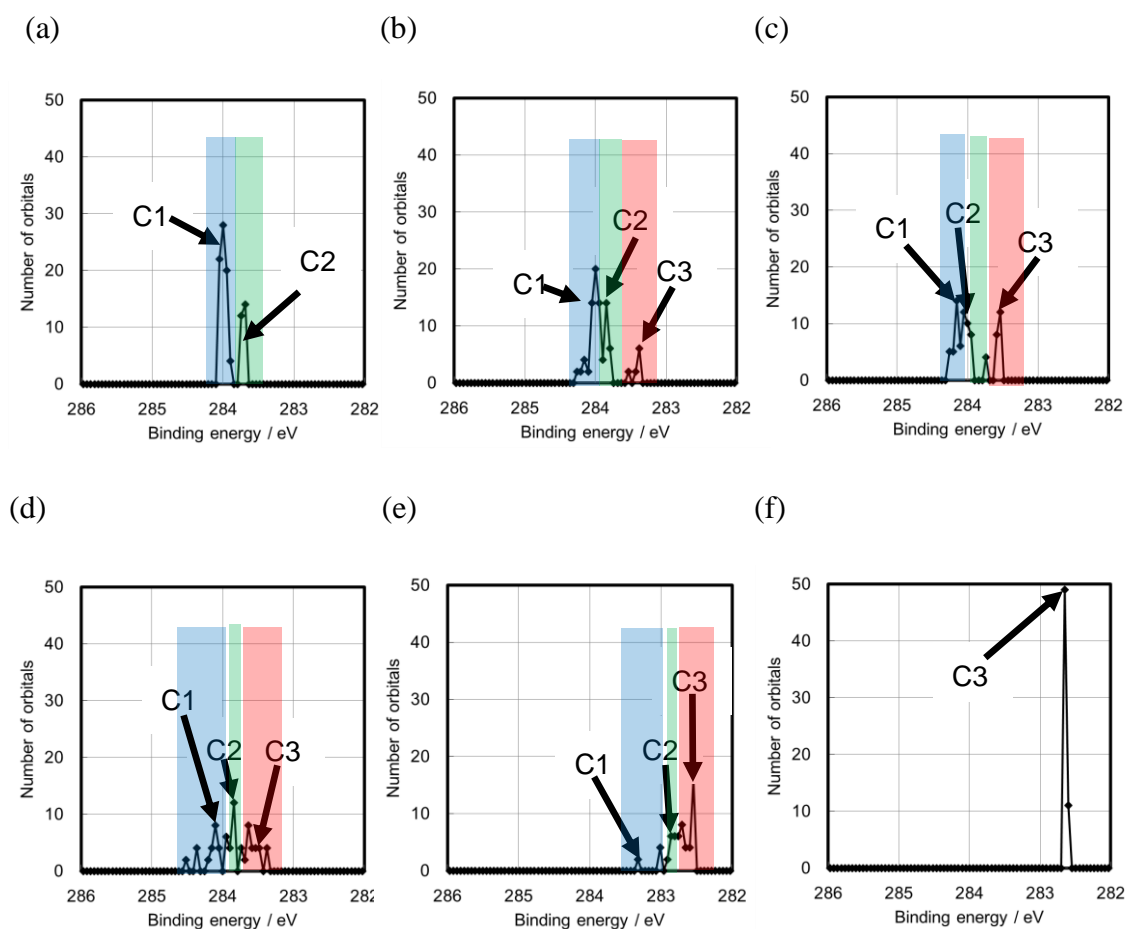


**Figure 2-3** Simulated C1s XPS spectra of structures shown in Fig. 2-2. (a) Graphene terminated with hydrogen atoms. (b) Two pentagons. (c) Four pentagons. (d) Six pentagons. (e) Eight pentagons. (f) Twelve pentagons without hydrogen atoms (Fullerene). C1 indicates carbon atoms on hexagons which bonded with carbon atoms. C2 indicates carbon atoms bonded with hydrogen atoms. C3 indicates carbon atoms on pentagons.

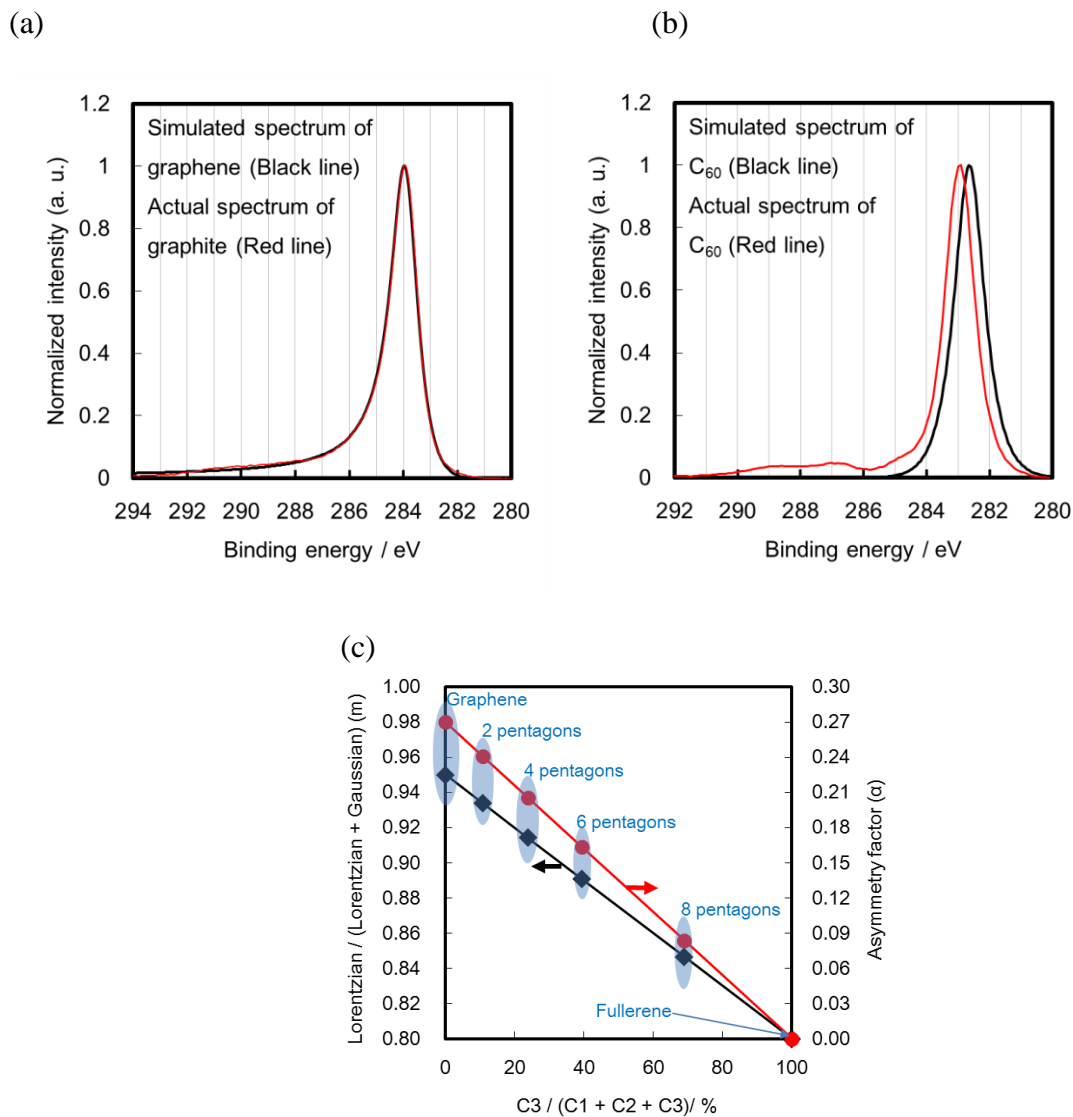


**Figure 2-4** Actual XPS spectra of graphite and C<sub>60</sub> and simulated XPS spectra of graphene and C<sub>60</sub> using asymmetric Voigt-type with different of values of  $m$  and  $\alpha$ . (a) XPS spectra of graphene (graphite). Black line: Simulated XPS spectrum of graphene using asymmetric Voigt-type lineshape ( $m = 0.95$ ,  $\alpha = 0.27$ ). Red line: Actual XPS spectrum of graphite. (b) XPS spectra C<sub>60</sub>. Black line: Simulated XPS spectrum of C<sub>60</sub> using asymmetric Voigt-type lineshape ( $m = 0.80$ ,  $\alpha = 0$ ). Red line: Actual XPS spectrum of C<sub>60</sub>. (c) Proposed values of  $m$  and  $\alpha$  for applying simulated XPS spectrum of each structure (Fig. 2-2).

### **2.1.1.2 Measurement of X-ray photoelectron spectroscopy**

Graphite (SP270, particle size: 4  $\mu\text{m}$ , Brunauer-Emmett-Teller specific (BET) surface area: 265  $\text{m}^2\text{g}^{-1}$ ) was provided from Nippon Graphite Industries, Ltd in Japan. This graphite consists of ca. 10 layers of graphene which were geometrically calculated from the BET specific surface area. Fullerene ( $\text{C}_{60}$ ) was purchased from Kanto Chemical, Ltd. in Japan. XPS analysis (AXIS ULTRA DLD, Shimadzu Corp.) was conducted using X-ray gun of Mg at 10 mA and 10 kV and pass energy of 40 eV. Samples were placed on conductive tapes (3 M X-7001) for XPS analysis. The binding energies at peak maxima of C1s spectra of graphite and fullerenes were obtained after adjusting energies at Fermi level to 0 eV for correcting charging phenomenon. As another method, gold nano powder (99.9 %, <100 nm, Sigma-Aldrich Corp.) was placed on samples for correcting charging phenomenon. Au4f<sub>7/2</sub> was set at 83.8 eV, and all of the spectra were adjusted. Adjustment of energies at Fermi level to 0 eV was selected in two methods for correcting charging phenomenon in this work. The modified asymmetric Voigt-type lineshape [195] was applied to separate the waveform of XPS spectra. All of the maximum intensities of C1s spectra were adjusted to 1.0.

## **2.1.2 Pyrolysis of epoxidized fullerenes analyzed by spectroscopies**

### **2.1.2.1 Simulation of X-ray photoelectron spectroscopy**

Calculation method is the same to that in section 2.1.1.1. All calculations were carried out using a whole  $\text{C}_{60}$  molecule. Charge was set as 0 and spin multiplicity ( $M$ ) was set as either 1 or 3, where  $M$  is equal to 1 unless stated. After the structures were optimized, population analyses for simulated XPS spectra were conducted. For simulating C1s XPS spectra using the calculated binding energy, the first scaling factor of 1.024, obtained from dividing the empirical value of 284.3 eV by the calculated value of 277.6 eV, was multiplied to all of calculated binding energies to compensate for the difference between calculated values and empirical values [83]. The second scaling factor of 1.2 was further multiplied to simulated C1s shifts from C=C and simulated O1s shifts from C-O in epoxides.

### **2.1.2.2 Measurement of X-ray photoelectron spectroscopy**

The defective structure of epoxidized  $\text{C}_{60}$  and the pyrolyzed sample of epoxidized  $\text{C}_{60}$  were characterized by XPS (AXIS ULTRA DLD, Shimadzu Corp.). Measurement method is the same to that of section 2.1.1.2. The main peak originating from C=C was normalized to unity and the peak top was adjusted to 284.9 eV which is

the peak top of the main peak for as-received C<sub>60</sub>.

## **2.2 Other experimental parts**

### **2.2.1 Pyrolysis of epoxidized fullerenes analyzed by spectroscopies**

#### **2.2.1.1 Sample preparation**

Fullerene C<sub>60</sub> (0.001 mol, purity 99%, Kanto Chemical, Ltd.) was added in toluene (100 ml, Wako Pure Chemical Industries, Ltd.) dissolving m-chloroperoxybenzoic acid (0.01 mol, Tokyo Chemical Industry Co., Ltd.). The solution was stirred at 343 K for 50, 300, and 900 h. Epoxidized C<sub>60</sub> is abbreviated as E\_T, where T is a reaction time in hour. Epoxidized C<sub>60</sub> was separated from purple solution by filtration. The filtered brown solid was rinsed with methanol (Wako Pure Chemical Industries, Ltd.) five times and dried at 323 K for 24 h. Epoxidized C<sub>60</sub> was pyrolyzed at 673 K for 1 h in helium gas to remove thermally unstable oxygen-containing functional groups along with carbon atoms on C<sub>60</sub>. The pyrolyzed sample of epoxidized C<sub>60</sub> is abbreviated as E\_T-P, where P stands for pyrolysis.

#### **2.2.1.2 Characterization**

The amount of CO and CO<sub>2</sub> gases formed from epoxidized C<sub>60</sub> were determined by elemental analysis (CE-440F, Elemental Analysis Inc.). The gases decomposed from epoxidized C<sub>60</sub> were also analyzed by direct injection-mass spectrometry (DI-MS, GCMS-QP2010 plus, Shimadzu Corp.) up to 673 K at a heating rate of 10 K min<sup>-1</sup>. The defective structure of epoxidized C<sub>60</sub> and the pyrolyzed sample of epoxidized C<sub>60</sub> were characterized by diffuse reflectance infrared Fourier transform (DRIFT) spectroscopy (FT-IR-4200, JASCO Corp.). DRIFT spectroscopic analysis was performed with a resolution of 4 cm<sup>-1</sup> after each sample was mixed with 100 times of KBr in weight for measurement. HRTEM and powder X-ray diffraction (XRD) were carried out to ensure the absence of cross-linking. For HRTEM observation, C<sub>60</sub> and epoxidized and pyrolyzed C<sub>60</sub> were inserted inside SWCNTs with a diameter of ca. 1.5 nm. Purified and uncapped SWCNTs were placed in a glass ampule with as-received C<sub>60</sub> or pyrolyzed sample of epoxidized C<sub>60</sub>, and the ampule was sealed in vacuum and heated at 673 K for 50 h. The peapods were rinsed with methanol to remove C<sub>60</sub> outside the SWCNTs and dried prior to HRTEM observation. HRTEM was carried out on the TEAM 0.5 microscope carried out to ensure the absence of cross-linking. The microscope was operated in monochromated mode at 50 keV and tuned for bright atom contrast (C3 = -13 μm, C5 = 4 mm). Crystallographic analysis was performed with

powder XRD (XRD7000, Shimadzu Corp.) in reflection mode using CuK $\alpha$  radiation.

### **2.2.1.3 Computational method**

Frequency analysis for computational DRIFT spectra was conducted using Gaussian 09 [193]. The scaling factor of 0.96 was multiplied with the calculated DRIFT spectra to adjust the difference with empirical spectra. Charge distributions were obtained using the Mulliken population analysis.

### **2.2.2 Oxygen migration and selective CO and CO<sub>2</sub> formation from epoxidized fullerenes**

All calculations were carried out using an entire C<sub>60</sub> molecule by the DFT calculation at the B3LYP/6-31G(d) integral=grid=ultrafine level using Gaussian 09 [193], not using a partial structure of C<sub>60</sub>. Charge was set as 0. Spin multiplicity ( $M$ ) was basically set as 1 except an O<sub>2</sub> molecule ( $M=3$ ) and a carbene site. Spin multiplicity of structures with a carbene site was set as both  $M=1$  and  $M=3$ . Total electron energies at ground and transition states were calculated to obtain activation energies. The structures of transition states were verified by the existence of imaginary vibrations obtained from frequency analyses and intrinsic reaction coordinate analyses.

## Chapter 3 Results and discussion

### 3.1 Spectral change of simulated X-ray photoelectron spectroscopy from graphene to fullerene

Figure 3-1a-f shows simulated C1s XPS spectra using structures in Fig. 2-2a-f. The peak tops originating from C1 (a thin line) and C2 (a dashed line) in Fig. 3-1a were at 284.0 and 283.7 eV, respectively. The peak top of C2 is lower than that of C1 in binding energy because hydrogen atoms donate electrons to carbon atoms of C2 (Fig. 3-2) [83, 157]. The peak top of C3 in graphene with two pentagons (a dotted line) was located at 283.4 eV (Fig. 3-1b), whose binding energy was the lowest among those of C1, C2, and C3 because of electron-withdrawing nature of the pentagons (Fig. 3-3). In Table 3-1 and Fig. 3-1, the binding energies of peak tops of C3 for graphene with two, four, and six pentagons were the lowest among peak tops of C1, C2, and C3 of each spectrum (Fig. 3-1b-d), but the binding energy of the peak top of C2 for graphene with eight pentagons (282.6 eV in Fig. 3-1e) was lower than that of C3 (282.7 eV in Fig. 3-1e). This change was induced by the connection of all eight pentagons in graphene and the decrease of the number of electrons on carbon atoms (Table 3-1 and Fig. 3-4).

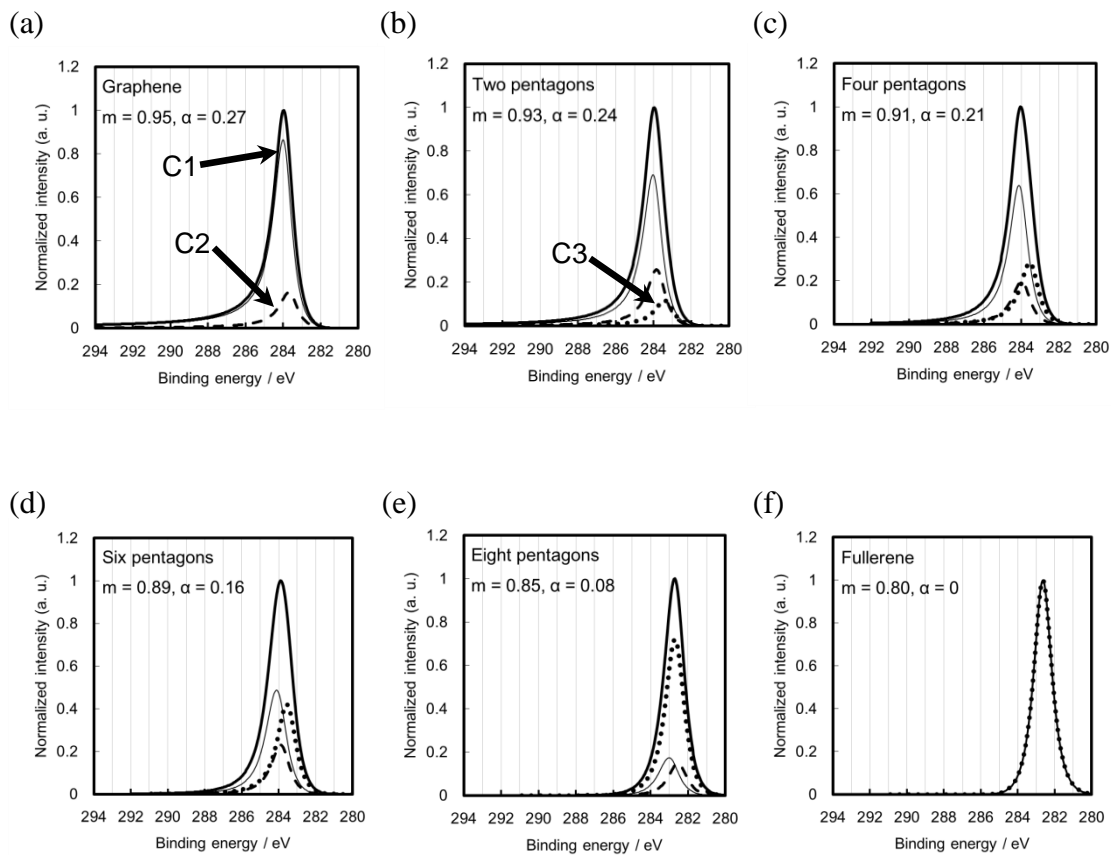


**Figure 3-1** Simulated and normalized C1s XPS spectra of structures shown in Fig. 2-2 using asymmetric Voigt-type lineshape. Simulated original spectra are shown as bold lines. Peaks originating from carbon atoms on hexagons which bonded with carbon atoms (C1), carbon atoms bonded with hydrogen atoms (C2), and carbon atoms on pentagons (C3) are shown as thin, dashed, and dotted lines, respectively. (a) Graphene terminated with hydrogen atoms. (b) Two pentagons. (c) Four pentagons. (d) Six pentagons. (e) Eight pentagons. (f) Twelve pentagons without hydrogen atoms (Fullerene). Values of  $m$  and  $\alpha$  (Fig. 2-4) were applied to each spectrum.

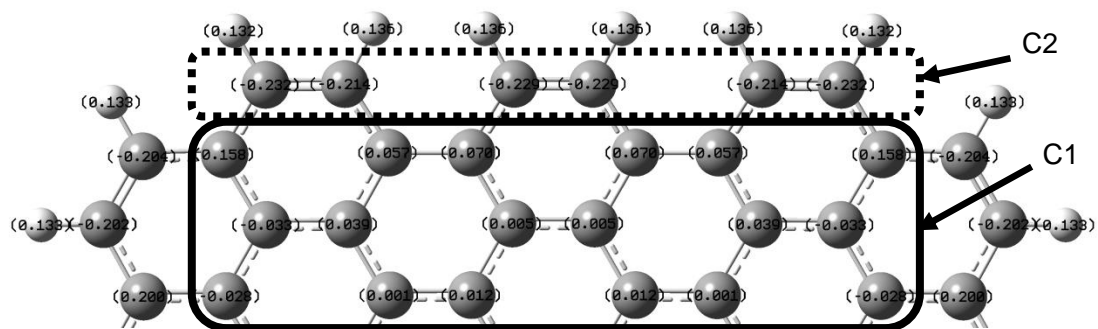


**Figure 3-2** Mulliken charge distribution of graphene terminated with hydrogen atoms. C1 indicates carbon atoms which bond with carbon atoms. C2 indicates carbon atoms bonded with hydrogen atoms.

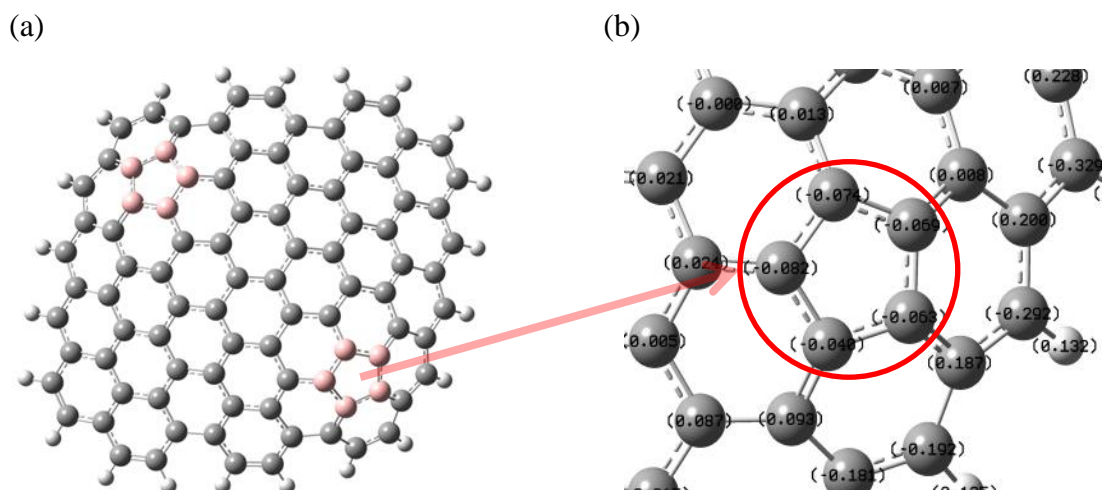


**Figure 3-3** Mulliken charge distribution of graphene with two pentagons. (a) An optimized structure. Two pentagons are identical in structures. (b) A magnified image of (a) and charge distribution of one pentagon.

**Table 3-1** Calculated peak shifts and FWHMs of C1s spectra and work function.

Number of pentagons		0	2	4	6	8	12
Ratio of the number of carbon atoms (C1:C2:C3)		100:26:0	60:22:10	46:18:20	32:14:30	10:8:40	0:0:60
Whole C1s spectrum (C1 + C2 + C3)	Peak top / eV	284.0	284.0	284.0	283.9	282.7	282.7
	FWHM / eV	1.25	1.30	1.35	1.45	1.25	1.15
Simulated whole C1s spectrum [196]	Peak top / eV	289.7-290.1 (Pyrene)	-	-	-	-	290.5
	Peak top / eV	284.3 (Graphite)	-	-	-	-	284.7
C1 + C3	Peak top / eV	-	284.0	284.0	283.9	282.8	-
	FWHM / eV	-	1.25	1.45	1.55	1.25	-
C1 (Hexagon)	Peak top / eV	282.9	283.0	283.0	283.0	281.9	-
	Peak shift of C1 from C1 of graphene / eV	0	0.1	0.1	0.1	-1.0	-
	FWHM / eV	1.15	1.20	1.15	1.30	1.20	-
C2 (C-H)	Peak top / eV	283.7	283.9	284.0	283.9	282.6	-
	Peak shift of C2 from C1 / eV	-0.3	-0.2	-0.1	-0.2	-0.4	-
	FWHM / eV	1.15	1.20	1.20	1.15	1.15	-
C3 (Pentagon)	Peak top / eV	-	283.4	283.6	283.6	282.7	-
	Peak shift of C3 from C1 / eV	-	-0.7	-0.5	-0.5	-0.3	-
	FWHM / eV	-	1.20	1.15	1.20	1.15	-
Work function <sup>a</sup> / eV		3.98	4.03	4.13	4.30	5.56	5.99
Empirical work function / eV [197]		4.73 (Graphite)	-	-	-	-	6.16
Empirical work function / eV [198]		4.80 (Graphite)	-	-	-	-	6.50
Averaged number of electrons of one carbon atom on one pentagon		-	6.066	6.060	6.034	6.008	-

<sup>a</sup>Work function: Energy difference between HOMO level and vacuum level.

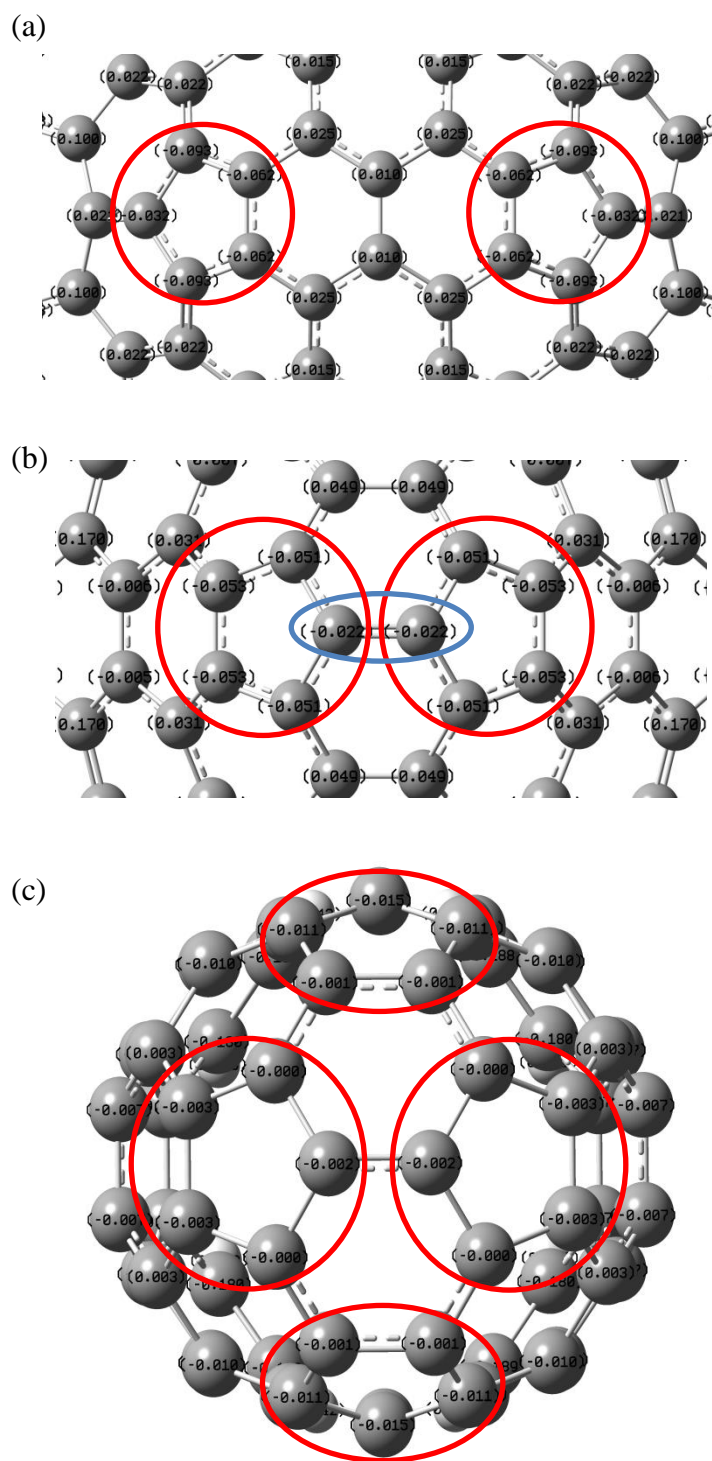


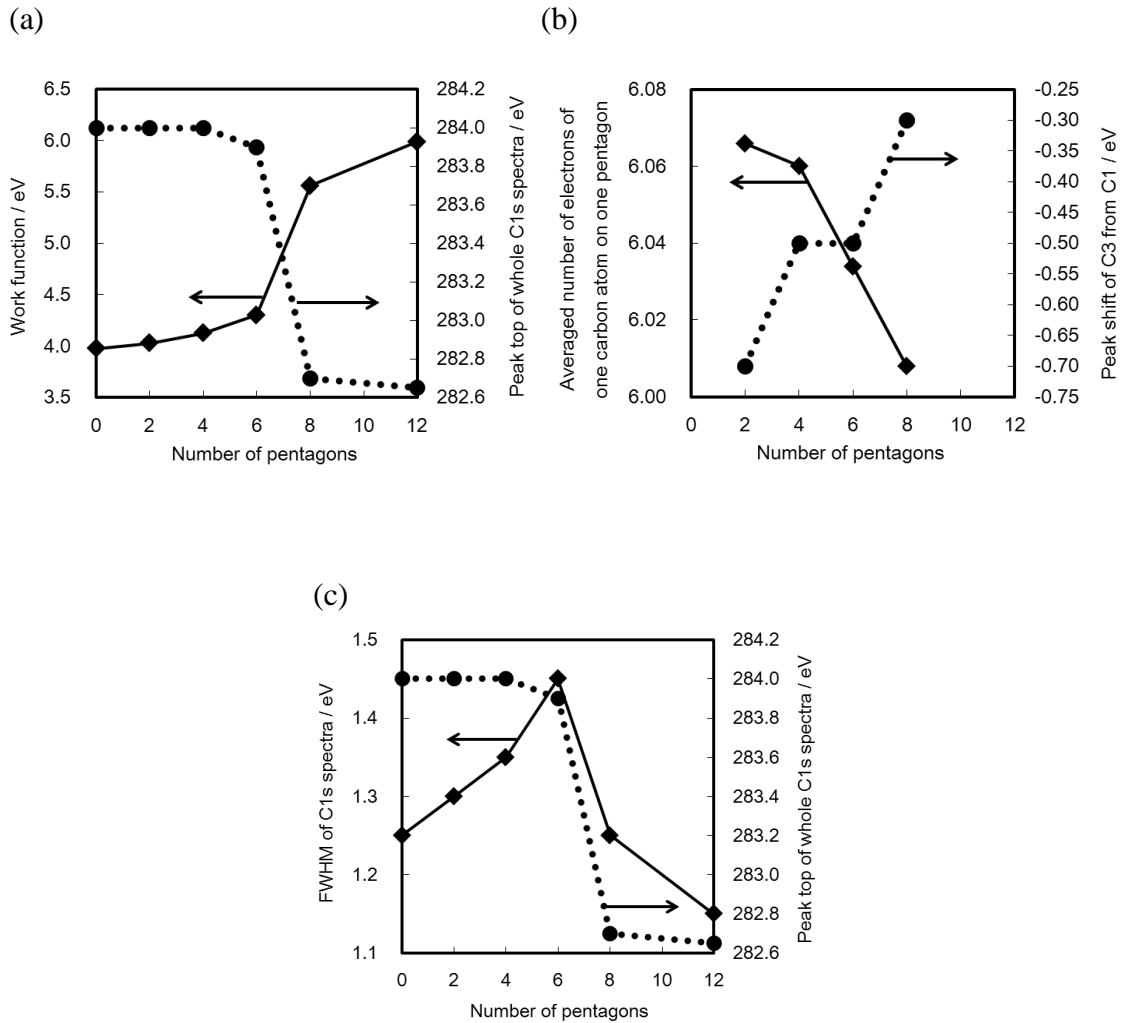
**Figure 3-4** Mulliken charge distributions of isolated pentagons and connected pentagons. (a) Two isolated pentagons. (b) Two connected pentagons. (c) Eight connected pentagons. Red circle: One pentagon. Blue circle: Two carbon atoms bonded each other in two connected pentagons.

The peak top of calculated spectra of graphene (284.0 eV) was slightly shifted to 283.9 eV by introducing six pentagons and the peak top was dramatically shifted to lower binding energy as the number of connected pentagons increased. The peak top reached up to 282.7 eV by introducing twelve pentagons (fullerene) (Figs. 2-2 and 3-1 and Table 3-1). These tendencies were well-matched with results simulated in a state of elimination of hydrogen atoms on edges (C2) (Table 3-1). Actual peak tops of C1s spectrum of graphite and fullerenes analyzed by a device in this work were 284.0 and 282.9 eV from Fermi level, respectively (Fig. 3-6). The actual peak shift of C1s spectrum of fullerenes from that of graphite was -1.1 eV, whereas the calculated peak shift of C1s spectrum of fullerene from that of graphene was -1.3 eV (Table 3-1). The difference between actual and calculated binding energy can be explained by the charging phenomena of fullerenes with low electrical conductivity. I calculated the peak position of C1s spectrum using fullerene with charge +2 to explain this difference between actual and computational values. I obtained the result that peak position of fullerene with charge +2 (283.1 eV) was higher than that of fullerene (282.9 eV), indicating that the binding energy of fullerene cation shifted higher than that of fullerene without charging.

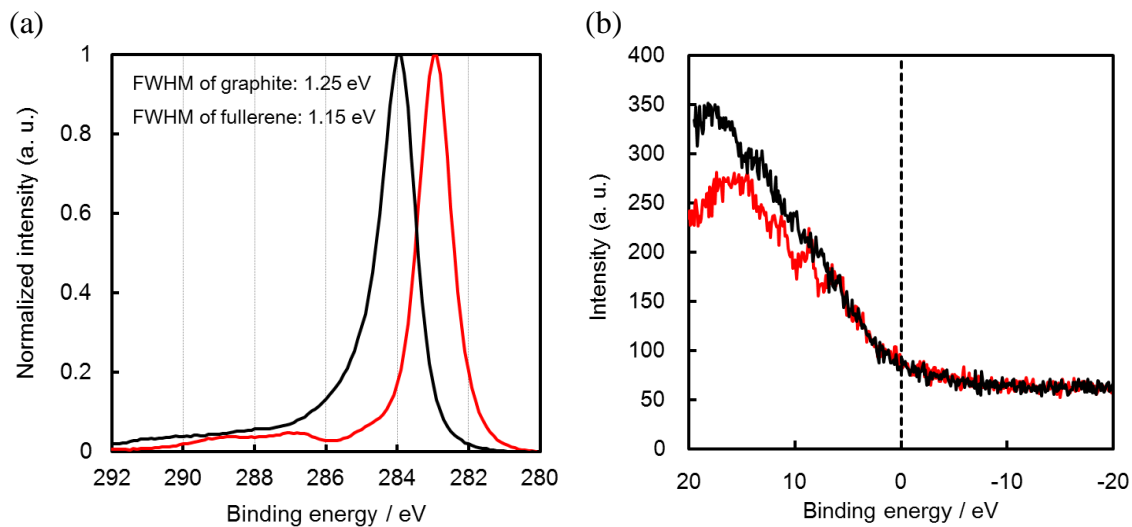
The reported empirical binding energy of the peak top of C1s spectrum for graphite (284.3 eV), on the other hand, was lower than that for C<sub>60</sub> (284.7 eV) (Table 3-1) [196]. Similarly, the reported calculated binding energy of the peak top of the whole C1s spectrum for pyrene (from 289.7 to 290.1 eV), which was utilized as a substitute of graphite, was lower than that of C<sub>60</sub> (290.5 eV) [196]. These opposite tendency between our results and reported values [196] can be explained from the difference of standards. The peak tops of empirical C1s spectra of graphite and C<sub>60</sub> using Au4f<sub>7/2</sub> as a standard were 284.3 and 284.6 eV, respectively. The peak tops of calculated C1s spectra of graphene and C<sub>60</sub> using vacuum level as a standard in this work were 284.3 and 285.1 eV, respectively. My empirical results using Au4f<sub>7/2</sub> and calculated results using vacuum level imply that the standard for the reported data may not be Fermi level, but I utilized the Fermi level to alleviate the charging effect caused by the low electronic conductivity of C<sub>60</sub>.

Several groups have reported that the work functions of graphite and C<sub>60</sub> are 4.73-4.80 and 6.16-6.50 eV [197, 198], respectively. In this work, the calculated work functions, which were determined from energy differences between HOMO level [199] and vacuum level, were 3.98, 4.03, 4.13, 4.30, 5.56, 5.99 eV for graphene with zero (graphene), two, four, six, eight, and twelve (fullerene) pentagons, respectively (Table

3-1). The negative shifts of the peak top of C1s spectra were well-correlated with the increment of these work functions as the number of pentagons increased (Table 3-1 and Fig. 3-5a), because C1s orbitals and Fermi level become close to the atomic nucleus and the energy required for removing electrons from carbon atoms in graphene with pentagons becomes smaller than those without pentagons.



**Figure 3-5** Dependence of physical properties on the number of pentagons. (a) Dependence of work functions and peak tops of whole C1s spectra on the number of pentagons. (b) Dependence of averaged numbers of electrons of 1 carbon atom on 1 pentagon and peak shifts of C3 from C1 on the number of pentagons. (c) Dependence of FWHMs and peak tops of C1s spectra on the number of pentagons.



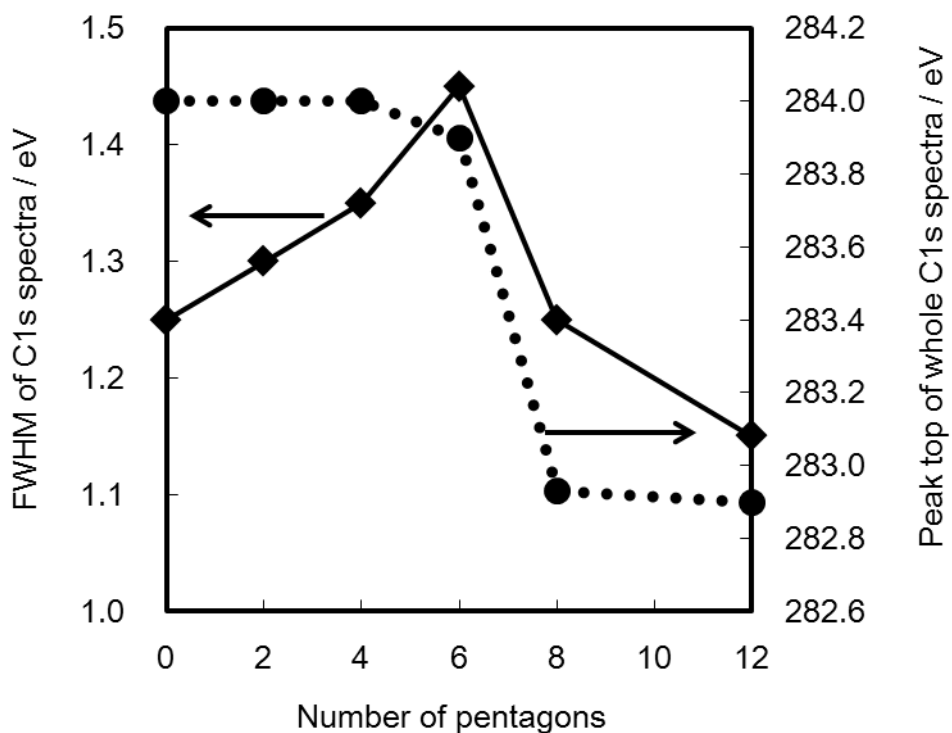
**Figure 3-6** Actual C1s XPS spectra (a) and spectra near Fermi level (b) of graphite and fullerene. Black line: graphite. Red line: fullerene.

Table 3-1 shows peak shifts of C1 of graphene with pentagons from C1 of graphene without pentagons. It also shows peak shifts of C2 and C3 from C1. The peak top of C1 was negatively shifted from 284.0 to 283.0 eV as the number of pentagons increased from zero to eight. The peak shifts of C2 for graphene without pentagons were -0.3 eV and those for graphene with pentagons were from -0.1 to -0.4 eV, indicating that the shift of C2 from C1 was not drastically changed. The peak shifts of C3 for graphene with two, four, six, and eight pentagons from C1 were -0.7, -0.5, -0.5, and -0.3 eV, respectively (Table 3-1 and Fig. 3-1). The increment of peak shifts of C3 from C1, i.e. from -0.7 to -0.3 eV, can be explained by an averaged number of electrons of one carbon atom on one pentagon. The averaged numbers of electrons of one carbon atom on one pentagon were 6.066, 6.060, 6.034, and 6.008 in graphene with two (Fig. 3-3), four, six, and eight pentagons, respectively (Table 3-1). The averaged numbers of electrons were obtained by adding the number of electron (6.000) for carbon atoms to the negative value of Mulliken charge. Especially, connection of pentagons reduced the number of electrons (Fig. 3-4). This connection caused the positive peak shifts of C3.

The number of pentagons in graphene also had an influence on FWHMs of C1s spectra in addition to the shift. Calculated FWHMs of whole C1s spectra of graphene (1.25 eV for graphene including peaks originated from C-H bonding and 1.15 eV for graphene excluding peaks originated from C-H bonding) and fullerenes (1.15 eV) in

Table 3-1 and Fig. 3-5c were well-matched with actual FWHMs of whole C1s spectra of graphite (1.25 eV) and fullerenes (1.15 eV) in Fig. 3-6a. However, FWHMs were increased to 1.30, 1.35, 1.45, and 1.25 eV by introducing two, four, six, and eight pentagons in graphene, respectively (Table 3-1 and Fig. 3-5c). The reason for the small FWHMs of the calculated and actual C1s spectra of graphene (1.25 eV) and fullerenes (1.15 eV) is the presence of either similar or same states of C-C bonding, respectively. For example, graphene terminated with hydrogen atoms contains only two types of carbon atoms such as hexagonal  $sp^2C-sp^2C$  (C1) and  $sp^2C-H$  (C2) and fullerene contains only one type of pentagonal  $sp^2C-sp^2C$  (C3). The increment of pentagons increased the presence of different states of C-C bondings and FWHMs became wide similar to our previously reported results of FWHMs of C1s spectra for graphene with oxygen- and nitrogen-containing functional groups [83, 157]. The FWHM of whole C1s XPS spectra (C1+C2+C3) basically depended on the calculated peak shifts of C1, C2, and C3 spectra as well as the ratios among the numbers of carbon atoms of C1, C2, and C3 (Fig. 3-1). Especially, the ratio between the number of carbon atoms with the highest binding energy (C1) and that with the lowest binding energy (C3) influenced FWHMs. The ratio between C1 and C3 of graphene with six pentagons was close to each other (C1:C3=32:30) and this specific ratio increased FWHMs significantly.

Figure 3-7 and Table 3-2 show proposed FWHMs and peak tops of whole C1s spectra for actual XPS analysis. Calculated results (Fig. 3-5c and Table 3-1) and actual measured results (Fig. 3-6a) were used to obtain proposed peak tops. The Fermi energies of graphite and  $C_{60}$  were set as 0 eV (Fig. 3-6b) for fair comparison of the peak position of C1s spectrum between graphite and  $C_{60}$ . Introduction of six pentagons increased the proposed FWHM up to 1.45 eV, and it slightly shifted the proposed peak top from 284.0 eV to a low binding energy of 283.9 eV. Introduction of eight pentagons decreased the proposed FWHM compared to six pentagons, and it shifted the proposed peak top to 282.9 eV. The binding energy is high for graphene with 0-6 pentagons (from 284.0 to 283.9 eV) and become low by introducing more than 8 pentagons (282.9 eV). By separating Fig. 3-7 into two regions such as below and above 6 pentagons, the number of pentagons can be determined using FWHMs because the FWHMs depend on the number of pentagons.



**Figure. 3-7** Proposed FWHMs and peak tops of whole C1s spectra of graphene including 0 to 8 pentagons and fullerene. The peak tops of actual spectra of graphite and fullerene in Fig. 3-6 were utilized for adjustment.

**Table 3-2** Proposed peak shifts and FWHMs of C1s spectra.

Number of pentagons		0 (Graphene)	2	4	6	8	12 (Fullerene)
Whole C1s spectrum	Peak top / eV	284.0	284.0	284.0	283.9	282.9	282.9
	(C1+C2+C3)	FWHM / eV	1.25	1.30	1.35	1.45	1.25

## 3.2 Pyrolysis of epoxidized fullerenes analyzed by spectroscopies

### 3.2.1 Elemental analysis and constructed model structures

Table 3-3 shows the atomic percentages of carbon and oxygen atoms in epoxidized C<sub>60</sub> and the pyrolyzed sample of epoxidized C<sub>60</sub> by elemental analysis. On average, two to three oxygen atoms were introduced on each C<sub>60</sub> by epoxidation and one to two oxygen atoms were eliminated by heat treatment. E50 released 1.0 oxygen atom corresponding to 52% of oxygen atom (=1.0/1.9), whereas E900 released 1.4

oxygen atoms corresponding to 45% of oxygen atom (=1.4/3.1). It indicates that the energy barriers for removing one oxygen atoms from E50 and E900 are close to each other.

**Table 3-3** The number of oxygen atoms per one C<sub>60</sub> molecule prior to pyrolysis and the number of oxygen atoms eliminated per one C<sub>60</sub> molecule after pyrolysis as determined by elemental analysis.

Sample name	Atomic percentages of C and O		The number of oxygen atoms per one C <sub>60</sub>	The number of eliminated oxygen atoms per one C <sub>60</sub>
	Carbon	Oxygen		
C <sub>60</sub>	100	0.0	0.0	-
E50	97.0	3.0	1.9	-
E50-P	98.6	1.4	0.9	1.0
E300	96.3	3.7	2.3	-
E300-P	98.1	1.9	1.2	1.1
E900	95.1	4.9	3.1	-
E900-P	97.2	2.8	1.7	1.4

The number of oxygen atoms on epoxidized C<sub>60</sub> is estimated as three or less on average as results of elemental analysis. Thus, as possible structures, one (1A - 1C), two (2A - 2E), and three (3A - 3D) oxygen atoms were introduced on C<sub>60</sub> (Fig. 3-8). In addition, C<sub>60</sub> with a mono-vacancy defect (MV) was also listed as the pyrolyzed structure whose stability was confirmed using our calculated results [200]. A zigzag-type carbene site formed on MV, 1C, and 2C was marked as an asterisk (Fig. 3-8).

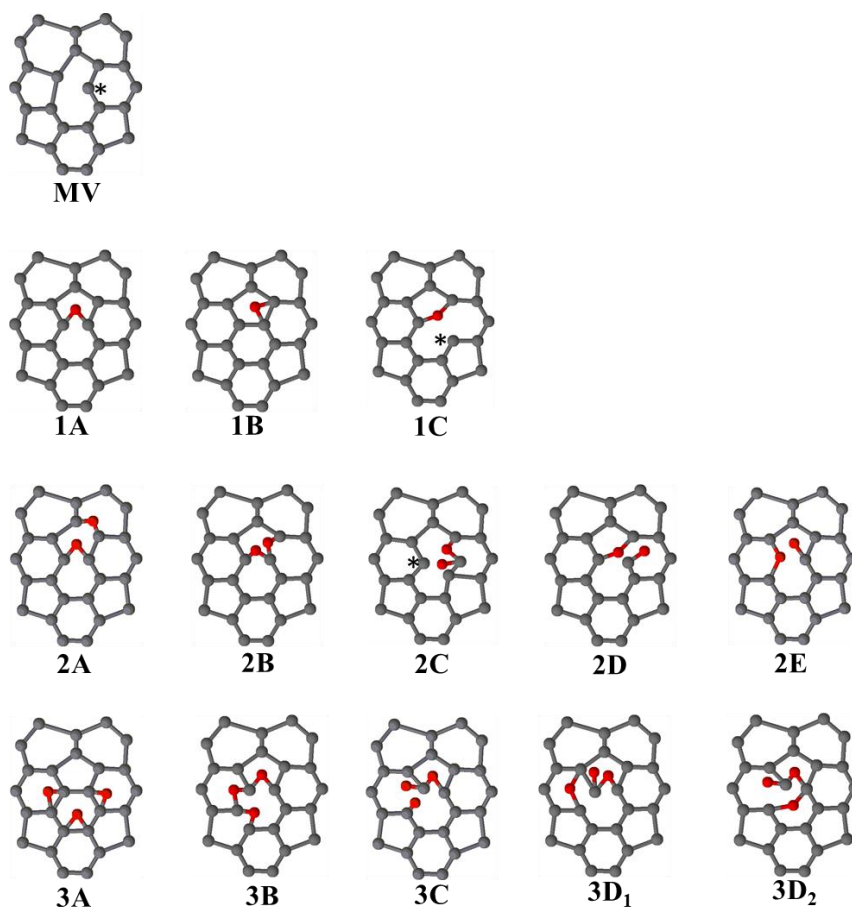


**Figure 3-8** Possible structures of epoxidized C<sub>60</sub> and pyrolyzed structures of epoxidized C<sub>60</sub>. The zigzag-type carbene site on MV, 1C, and 2C is marked with an asterisk.

### 3.2.2 Mass analysis

Figure 3-9 shows that the gases decomposed from E10, E50, E300, and E900 upon heat treatment as analyzed by DI-MS. CO and CO<sub>2</sub> gases were generated and O<sub>2</sub> gas was desorbed from epoxidized fullerenes upon heat treatment. The longer epoxidation time was, the more CO and CO<sub>2</sub> gases generated, whereas the amount of desorbed O<sub>2</sub> gas did not increase. Thus, the amount of vacancy defects on C<sub>60</sub> tended to increase as O coverage increases.

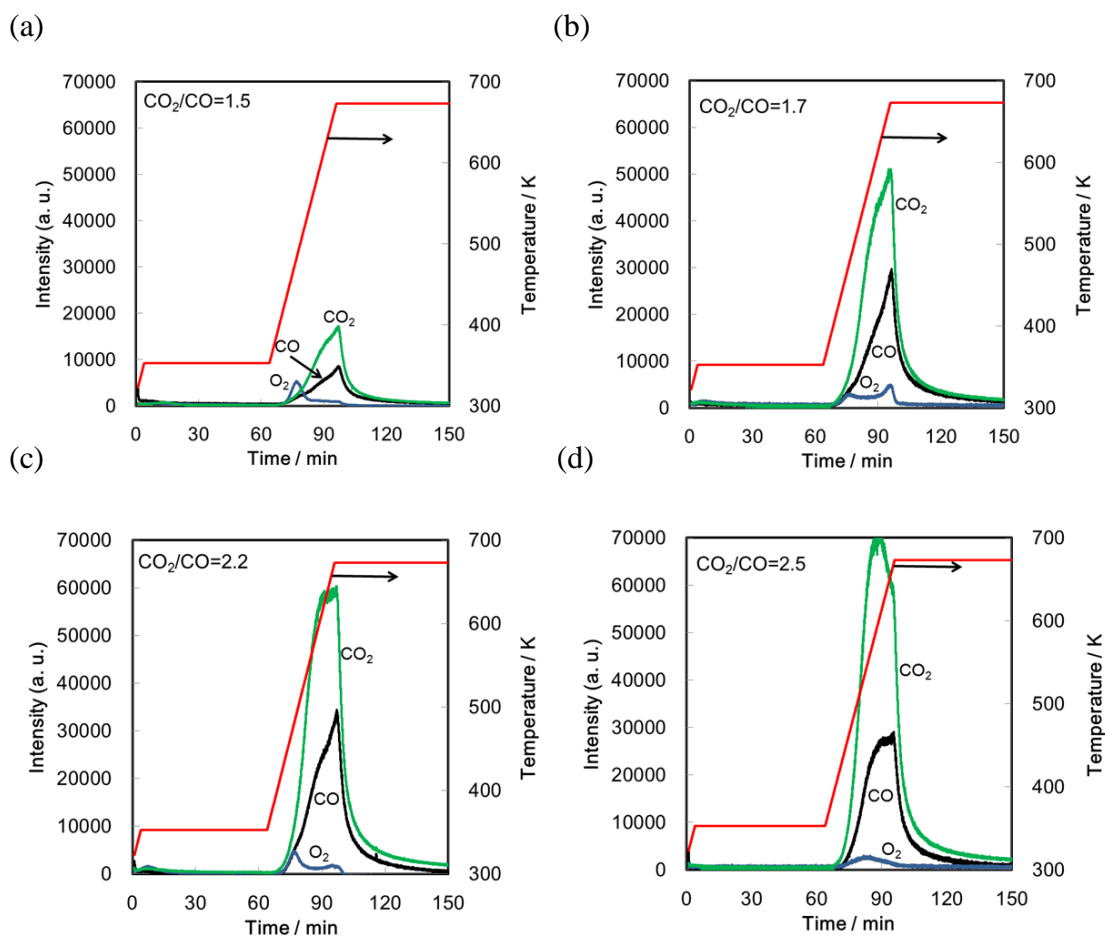


**Figure 3-9** Gases decomposed from (a) E10, (b) E50, (c) E300, and (d) E900 upon heat treatment as analyzed by DI-MS.

It was also found that the epoxidation time also affected the ratio of the  $\text{CO}_2$  gas to the CO gas. The ratios of the  $\text{CO}_2$  gas to the CO gas decomposed from E10, E50, E300, and E900 were 1.5, 1.7, 2.2, and 2.5, respectively. It indicates that the ratios of the  $\text{CO}_2$  gas to the CO gas increased as epoxidation time increased. I have shown by calculation that a CO gas tends to be released more than a  $\text{CO}_2$  gas from two oxygen atoms on  $\text{C}_{60}$ , whereas a  $\text{CO}_2$  gas tends to be released more than a CO gas from three oxygen atoms on  $\text{C}_{60}$  [200]. These results suggest that the pyrolysis mechanisms of epoxidized  $\text{C}_{60}$  strongly depend on the O coverage on  $\text{C}_{60}$ .

### 3.2.3 XPS analysis

#### 3.2.3.1 Computational XPS analysis

Table 3-4 shows the calculated C1s and O1s XPS shifts of various structures in Fig. 3-8 and C1s XPS shifts from references. The C1s XPS shifts originating from oxygen-containing functional groups have been reported [172-174], but the values of the peak shifts have wide ranges. For example, mono-oxygenated carbon varies between 0.2 and 1.4 eV, and di-oxygenated carbon varies between 1.6 and 3.8 eV.

From our calculated results, the detailed assignments were obtained. C1s shifts originating from C=C in C1s XPS spectra of C<sub>60</sub> range from -0.1 to 0.1 eV. The range of C1s shifts originating from C=C became wide (-0.6 ~ 0.8 eV) in the presence of vacancy defects and functional groups (VD and/or FGs in structures MV, 1C, and 2E). The tendency was same as our previously reported assignments for graphite oxide [83]. It has been reported that spin multiplicities of graphene with a zigzag-type carbene site influenced the charge distribution of graphene [201]. Thus, the spin multiplicities of 1 and 3 for MV, 1C, and 2C were compared in Table 3-4. C1s XPS peak shifts between *M* = 1 and 3 of MV, 1C, and 2C were slightly different. In terms of difference of total electron energies between *M* = 1 and 3 in MV, 1C, and 2C, the energy of MV (*M* = 3) was 14.0 kJ mol<sup>-1</sup> lower than that of MV (*M* = 1), whereas that of 1C (*M* = 1) was 65.4 kJ mol<sup>-1</sup> lower than that of 1C (*M* = 3) and that of 2C (*M* = 1) was 131 kJ mol<sup>-1</sup> lower than that of 2C (*M* = 3). Thus, *M* = 3 for MV and *M* = 1 for 1C and 2C were used for assigning C1s shifts.

In addition to the C1s shift originating from C=C, I obtained C1s shifts caused by the presence of oxygen-containing functional groups. The peak shifts originating from epoxide (1B and 3A) and unzipped epoxide (1A and 2A) were in the range of 1.6 ~ 1.8 eV. The peak shifts of C-O-C (ether), C-O-C=O (lactone), and C=O groups were in the range of 2.0 ~ 2.5 eV. The peak shifts of one carbon atom located in the middle of two connecting ether groups (C-O-C-O-C) in 2B, 3B, and 3D<sub>2</sub> were in the range of 3.1 ~ 3.5 eV. The peak shifts originating from C-O-C=O (lactone) groups were in the range of 3.5 ~ 4.0 eV.

In O1s spectra, the binding energy of the peak top of epoxide in 1A was used as a reference binding energy for O1s spectra. The peak shifts originating from C=O and C-O-C=O (lactone) groups were in the range of -1.6 ~ -0.7 eV. The peak shifts originating from oxygen atoms in two connecting ethers (C-O-C-O-C), ether (C-O-C), and lactone (C-O-C=O) groups were in the range of 0.5 ~ 1.3 eV.

**Table 3-4** Calculated peak shifts of C1s and O1s of various defects.

Model	Name of defects	C1s	O1s	C1s from references
		Peak shifts from the peak top of C=C (eV)	Peak shifts from the peak top of epoxide on 1A (eV)	Peak shifts from the peak top of C=C (eV)
-	Mono-oxygenated C (C-O)	-	-	0.2 [172], 2.0 [173], 1.4 [174]
-	Di-oxygenated C (C=O, O-C-O)	-	-	1.6 [172], 4.2 [173], 3.8 [174]
-	Tri-oxygenated C (COOH)	-	-	2.5 [172]
$C_{60}$	-	-0.1 ~ 0.1	-	-
MV ( $M=1$ )	VD <sup>a</sup>	-0.4 ~ 0.7	-	-
MV ( $M=3$ )	VD <sup>a</sup>	-0.5 ~ 0.6	-	-
1A	Unzipped epoxide	1.7	0	-
	FGs <sup>b</sup>	-0.1 ~ 0.6	-	-
1B	Epoxide	1.8	0	-
	FGs <sup>b</sup>	0 ~ 0.1	-	-
1C ( $M=1$ )	C-O-C	2.0	1.3	-
	VD <sup>a</sup> and/or FGs <sup>b</sup>	-0.1 ~ 0.5	-	-
1C ( $M=3$ )	C-O-C	2.6	1.3	-
	VD <sup>a</sup> and/or FGs <sup>b</sup>	-0.1 ~ 0.8	-	-
2A	Unzipped epoxide	1.7	0	-
	FGs <sup>b</sup>	-0.1 ~ 0.5	-	-
2B	<u>C-O-C-O-C</u>	3.2	0.5	-
	<u>C-O-C-O-C</u>	2.0	-	-
	FGs <sup>b</sup>	-0.1 ~ 0.8	-	-
2C ( $M=1$ )	<u>C-O-C=O</u>	4.0	-0.9	-
	<u>C-O-C=O</u>	2.0	0.7	-
	FGs <sup>b</sup>	-0.2 ~ 0.5	-	-
2C ( $M=3$ )	<u>C-O-C=O</u>	4.0	-1.1	-
	<u>C-O-C=O</u>	2.0	0.6	-
	FGs <sup>b</sup>	-0.1 ~ 0.8	-	-
2D	C-O-C	2.0	1.3	-
	C=O	2.3	-1.1	-
	FGs <sup>b</sup>	-0.2 ~ 0.6	-	-

2E	C-O-C	2.0	1.2	
	C=O	2.2	-1.6	-
	VD <sup>a</sup> and/or FGs <sup>b</sup>	-0.6 ~ 0.7	-	
3A	Epoxide	1.6	0	
	FGs <sup>b</sup>	-0.1 ~ 0.1	-	-
3B	<u>C-O-C-O-C-O-C</u>	3.5	1.1	
	<u>C-O-C-O-C-O-C</u>	2.2	1.1	-
	FGs <sup>b</sup>	-0.2 ~ 0.6	-	
3C	C=O	2.3	-1.4	
	C-O- <u>C=O</u>	3.5	-1.3	
	<u>C-O</u> -C=O	2.0	0.9	-
	FGs <sup>b</sup>	-0.1 ~ 0.6	-	
3D <sub>1</sub>	C-O(C=O)C- <u>O-C</u>	2.1	0.6	
	<u>C-O</u> (C=O)C-O-C	2.5	0.7	
	C-O(C=O) <u>C</u> -O-C	2.8	-	-
	C-O( <u>C=O</u> )C-O-C	4.0	-0.7	
	FGs <sup>b</sup>	-0.2 ~ 0.8	-	
3D <sub>2</sub>	<u>C-O</u> -C-O-C=O	2.2	0.7	
	C-O- <u>C-O</u> -C=O	3.1	0.1	
	C-O-C-O- <u>C=O</u>	4.0	-1.3	-
	FGs <sup>b</sup>	-0.2 ~ 1.0	-	

<sup>a</sup> VD: vacancy defect. <sup>b</sup> FGs: C=C influenced by neighboring functional groups such as unzipped epoxide, C=O, ether, and lactone groups.

### 3.2.3.2 Empirical XPS spectra

The calculated shifts in Table 3-4 were used to assign the empirical C1s and O1s peaks as shown in Tables 3-5 and 3-6, respectively. Figure 3-10 shows C1s and O1s spectra of C<sub>60</sub>, epoxidized C<sub>60</sub>, and the pyrolyzed sample of epoxidized C<sub>60</sub>. The peak shifts in Tables 3-5 and 3-6 were used to assign the peaks in Fig. 3-10. XPS spectra of defective graphene and graphite have been analyzed in detail recently. For instance, Larciprete and coworkers have analyzed C1s XPS spectra of graphene oxide and separated the spectra into seven peaks such as carbon atoms on a vacancy defect (VD), an interaction between graphene and a substrate, C=C, ether, epoxide, C=O, and lactone group [170]. Barinov and coworkers have analyzed the structure of defective highly

oriented pyrolytic graphite by calculated XPS spectra and separated the spectra of graphite with MV into four peaks depending on the positions near MV [81]. Our group has recently reported the calculated peak shifts of C1s and O1s spectra of pyrolyzed graphite oxide [83]. But these peak assignments of graphite oxide and graphite should not be exactly the same as those of fullerenes.

**Table 3-5** Lists of possible functional groups and other defects of C1s.

Number of peaks	Peak 1	Peak 2	Peak 3	Peak 4	Peak 5	Peak 6	Peak 7	Peak 8 <sup>c</sup>
Peak tops (eV)	284.3	284.9	285.7	286.6	287.3	288.0	288.8	290.9
Shifts from C=C (eV)	-0.6	0.0	0.8	1.7	2.4	3.1	3.9	6.0
FWHM (eV)	1.2	1.1	0.9	1.4	1.4	1.2	1.4	2.1
Possible functional groups and other defects	VD <sup>a</sup> , FGs <sup>b</sup>	C=C	VD <sup>a</sup> , FGs <sup>b</sup>	Epoxide, Unzipped epoxide	C-O-C, C=O, <u>C</u> -O-C=O	C-O- <u>C</u> -O-C	C-O- <u>C</u> =O	$\pi$ - $\pi^*$ shakeup

<sup>a</sup> VD: vacancy defect. <sup>b</sup> FGs: C=C which is influenced by neighboring functional groups as unzipped epoxide, C=O, ether, and lactone group. <sup>c</sup> Peak 8: the peak position was determined from a reference [202].

**Table 3-6** Lists of possible functional groups of O1s.

Number of peaks	Peak 9	Peak 10	Peak 11
Peak top (eV)	531.9	532.9	533.8
FWHM (eV)	1.4	1.6	1.6
Possible functional groups	C=O, C-O-C= <u>O</u>	Epoxide, Unzipped epoxide	C-O-C-O-C, C-O-C (Ether), C- <u>O</u> -C=O

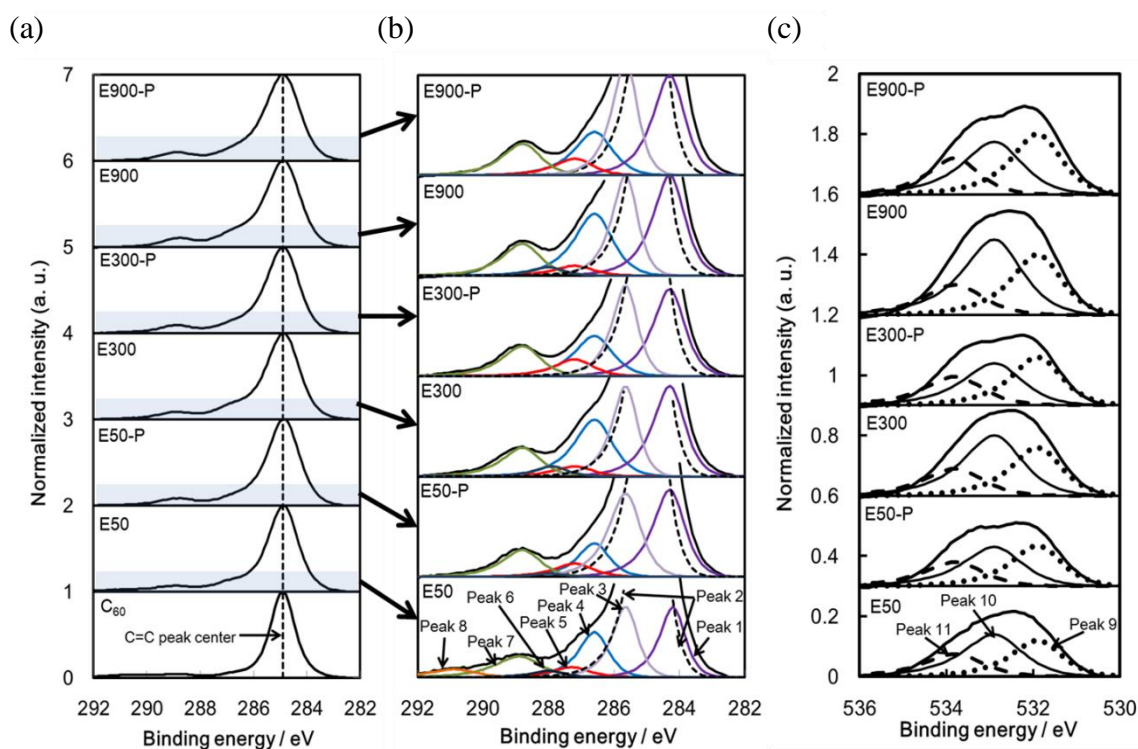


**Figure 3-10** XPS spectra of  $C_{60}$ , epoxidized  $C_{60}$ , and the pyrolyzed sample of epoxidized  $C_{60}$ . (a) C1s spectra. (b) Enlarged C1s spectra and waveform separation. (c) O1s spectra and waveform separation.

The C1s spectra of epoxidized  $C_{60}$  were fitted with up to eight peaks as shown in Fig. 3-10b. These peaks correspond to the following carbon atom components: VD and/or FGs (Peak 1), C=C (Peak 2), VD and/or FGs (Peak 3), epoxide and unzipped epoxide (Peak 4), C-O-C (ether) group, C=O group, and  $\underline{C}$ -O-C=O group (Peak 5), C-O- $\underline{C}$ -O-C group (Peak 6), C-O- $\underline{C}$ =O group (Peak 7), and pi-pi\* shakeup (Peak 8). The peak position of pi-pi\* shakeup (Peak 8) was determined from a reference [202]. The O1s spectra in Fig. 3-10c can be fitted with three components: C=O and C-O-C=O group (Peak 9), epoxide and unzipped epoxide (Peak 10), C-O-C-O-C, C-O-C (ether), and C-O-C=O group (Peak 11).

Figure 3-10 also shows the correlation between epoxidation time and the amount of epoxide (Peak 4 of E50, E300, and E900 in Fig. 3-10b and Peak 10 of E50, E300, and E900 in Fig 3-10c). After epoxidation, the C1s peak originating from pi-pi\* shakeup (Peak 8 in Fig. 3-10b) disappeared except for E50 because conjugated pi bonds were decreased. After epoxidized  $C_{60}$  was pyrolyzed at 673 K, the amount of epoxide

(Peak 4 in Fig. 3-10b and Peak 10 in Fig. 3-10c) and C-O-C-O-C groups (Peak 6 in Fig. 3-10b) also decreased, whereas that of C-O-C groups (Peak 5 in Fig. 3-10b) increased. The amount of the lactone groups (Peak 7 in Fig. 3-10b) remained unchanged. The reason for the unchanged amount of the lactone groups is thought to be because of the balance between a formation of the lactone groups by migration of epoxides and decomposition of the lactone groups into CO and CO<sub>2</sub> gases. Thus, the formation of CO and CO<sub>2</sub> gases detected by DI-MS should be because of the pyrolysis of the lactone groups.

### 3.2.4 DRIFT spectroscopic analysis

The functional groups were analyzed by DRIFT spectroscopy as shown in Fig. 3-11. The peak positions of vibration modes of C<sub>60</sub> (1183 and 1425 cm<sup>-1</sup>) and many functional groups such as epoxide (1000-1150 and 1250 cm<sup>-1</sup>), C=O groups (1750-1850 cm<sup>-1</sup>), and carboxyl groups (1650-1750 cm<sup>-1</sup>) on C<sub>60</sub> have been reported in FT-IR analyses [174,175]. Wohlers and coworkers experimentally showed that the peak at 1550 cm<sup>-1</sup> is because of isolated double bonds arising from break-down of conjugated double bonds in C<sub>60</sub> [15]. I interpreted the isolated double bonds as carbene sites. From the results of our calculated DRIFT spectra (Fig. 3-11a and b), the peak position of epoxide in 1B, unzipped epoxide in 1A and 2A, and zigzag-type carbene in 1C and MV is 1520-1590 cm<sup>-1</sup>. Unzipped epoxide in 1A and 2A also shows the peak at 1000-1165 cm<sup>-1</sup> and 1210-1260 cm<sup>-1</sup>. C=O group in 3C (1754 cm<sup>-1</sup>) and lactone groups in 2C and 3C (1801 cm<sup>-1</sup>) on C<sub>60</sub> were confirmed. The calculated peak positions of the lactone groups and carbene sites in Fig. 3-11a and b were used to analyze empirical DRIFT spectra in Fig. 3-11c-e.

Figure 3-11c-e shows empirical DRIFT spectra of C<sub>60</sub>, epoxidized C<sub>60</sub>, and C<sub>60</sub> pyrolyzed at 523 K and 673 K after epoxidation. Unzipped epoxides (1000-1150 and 1220-1270 cm<sup>-1</sup>), C=O groups (1650-1740 cm<sup>-1</sup>), and lactone groups (1740-1820 cm<sup>-1</sup>) were introduced on C<sub>60</sub> by epoxidation (E50, E300, and E900). After epoxidized C<sub>60</sub> were heated at 523 K (E50-P at 523 K, E300-P at 523 K, and E900-P at 523 K), the peaks corresponding to C=O and lactone groups increased because of the structural change from unzipped epoxides into combination of C=O and lactone groups such as 3C in Fig. 3-8. After epoxidized C<sub>60</sub> was heated at 673 K, the intensities corresponding to vibration modes of pure C<sub>60</sub> decreased because of the presence of oxygen-containing functional groups and vacancy defects. In addition, the amount of unzipped epoxides, lactone groups, and C=O groups decreased after epoxidized C<sub>60</sub> was heated at 673 K.

Decrease of the lactone group and C=O groups indicates that vacancy defects were introduced by formations of CO and CO<sub>2</sub> gases. After the heat treatment, the amount of residual lactone groups was less than that of the residual C=O groups. Mass spectrometry analysis indicated that epoxidized C<sub>60</sub> generated the CO<sub>2</sub> gas more than the CO gas upon heat treatment (Fig. 3-9). Thus, it is considered that the CO<sub>2</sub> gas was formed more than the CO gas from lactone groups by heat treatment. Moreover, the amount of carbene sites (1560-1620 cm<sup>-1</sup>) increased as the decomposition of C=O and lactone groups proceeded.

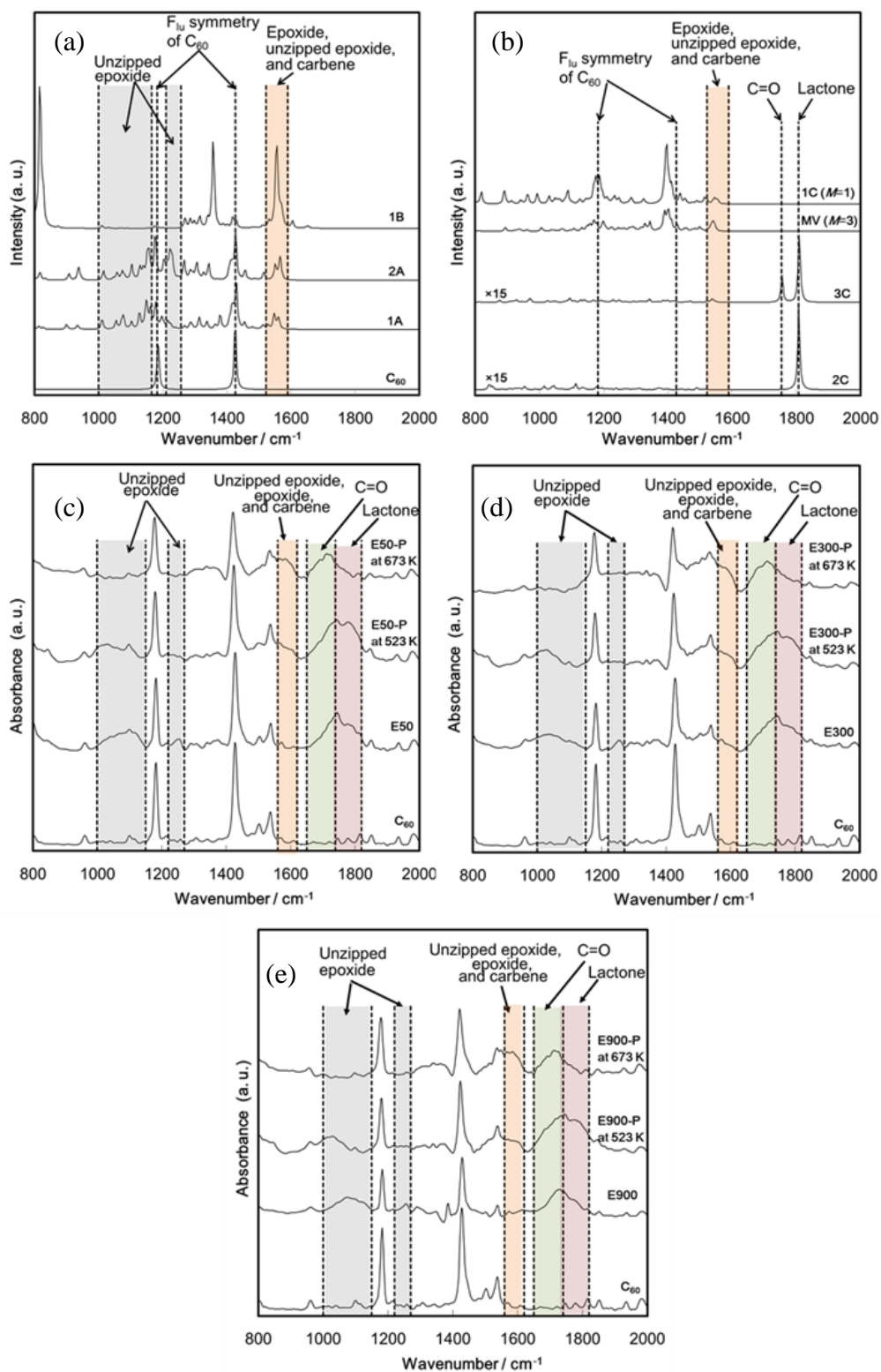


**Figure 3-11** Calculated and empirical DRIFT spectra of defective  $\text{C}_{60}$ . (a and b) Calculated DRIFT spectra of  $\text{C}_{60}$  and defective models in Fig. 3-8. (c-e) Empirical

DRIFT spectra of  $C_{60}$ , epoxidized  $C_{60}$ , and the pyrolyzed sample of epoxidized  $C_{60}$  at 523 K and 673 K after epoxidation. Epoxidation time is 50 h (c), 300 h (d), and 900 h (e).

### 3.2.5 Distributions of electronic charge

The effect of a neighboring oxygen atom on stabilizing a carbene site was analyzed by calculating distributions of electronic charge on carbon atoms and an oxygen atom of MV ( $M = 1, 3$ ) and 1C ( $M = 1, 3$ ) as shown in Fig. 3-12. The position of atoms on  $C_{60}$  is named as 1, 2, and so forth. The position 1 with an asterisk in Fig. 3-12a and b indicates a zigzag-type carbene site. The position 1 in MV is negatively charged because of the presence of a carbene site (Fig. 3-12a, c, and d). However, the position 1 in 1C is positively charged because of the presence of the neighboring oxygen atom with high electronegativity, indicating that the carbene site was stabilized (Fig. 3-12b, c, and d). The existence of a carbene site at a vacancy defect has been known to cause energetic destabilization [159]. But our result shows that one oxygen atom can stabilize a carbene site.

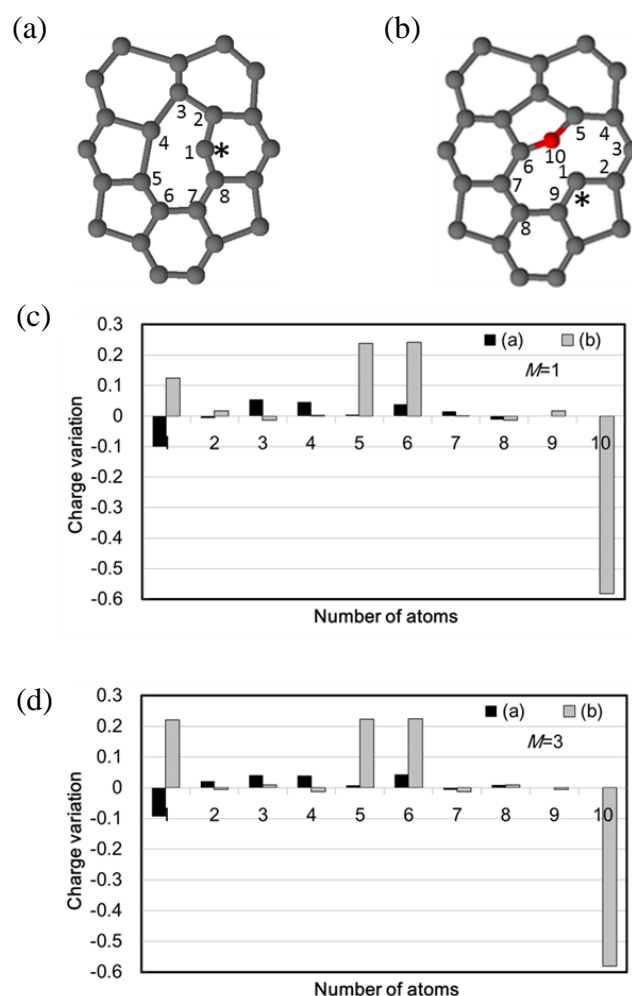


**Figure 3-12** Charge distributions of the structures including zigzag-type carbene with different spin multiplicity ( $M = 1$  and 3). (a) MV in Fig. 3-8. (b) 1C in Fig. 3-8. (c) Charge distributions of the MV and 1C ( $M = 1$ ). (d) Charge distributions on MV and 1C ( $M = 3$ ). The position 1 marked as an asterisk is a zigzag-type carbene site.

### 3.2.6 Proposed pyrolysis mechanism of epoxidized $C_{60}$

From the results of XPS and DRIFT spectroscopy, I propose the following change of functional groups and other defects. After epoxidation, 2A (two unzipped epoxides), 2B (a C-O-C-O-C group), 2C (a lactone group with a carbene site), 3A (three epoxides), 3B (a C-O-C-O-C-O-C group), and 3C (a lactone-ketone group) in Fig. 3-8 are formed. Upon heat treatment, 2C (a lactone group) is converted to 1C (an ether group with a carbene site) and the CO gas is formed. 2C (a lactone group with a carbene site) is also converted to MV and the  $CO_2$  gas is formed. In case of three epoxides on

C<sub>60</sub>, 3A (three epoxides) is converted to 3C (a lactone-ketone group). 3C (a lactone-ketone group) is converted to 2E (an ether-ketone group) and the CO gas is formed. 3C (a lactone-ketone group) is also converted to 1C (an ether group with a carbene site) and the CO<sub>2</sub> gas is formed. However, C=O and lactone groups, which exist in the structure such as 3C, still remain after heat treatment of epoxidized C<sub>60</sub> at 673 K. These results are well agreed with our proposed mechanisms which were obtained by calculation [200].

The decrease of the ratio of the CO<sub>2</sub> gas to the CO gas generated from C<sub>60</sub> with low O coverage (E10) compared to C<sub>60</sub> with high O coverage (E900) can be explained using the calculated apparent activation energies [200]. Migration of two and three oxygen atoms on C<sub>60</sub> is proposed to proceed via mechanisms in Fig. 3-13. By calculation, two oxygen atoms on C<sub>60</sub> (2A) in Route 1 migrate, and CO and CO<sub>2</sub> gases are formed. Among the structures with two oxygen atoms on C<sub>60</sub> such as 2A, 2B, 2C, and 2D, 2A has the lowest total electron energy. The apparent activation energy calculated from the energy of 2A for a formation of the CO<sub>2</sub> gas was larger than that of the CO gas. Thus, the CO gas tends to be generated from two epoxides. By calculation, three oxygen atoms on C<sub>60</sub> (3A) in Route 2 migrate and CO and CO<sub>2</sub> gases are formed. Among the structures with three oxygen atoms on C<sub>60</sub> such as 3A, 3B, 3C, 3D<sub>1</sub>, and 3D<sub>2</sub>, the total electron energy of 3C is the lowest. The apparent activation energy calculated from the energy of 3C for a formation of the CO gas was larger than that of the CO<sub>2</sub> gas. Thus, the CO<sub>2</sub> gas tends to be generated from three epoxides. These calculated apparent activation energies [200] support the empirical results obtained in this work.

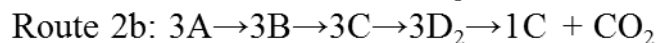
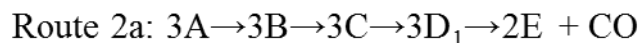
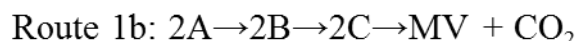
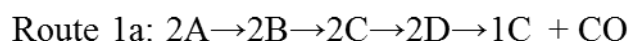


**Figure 3-13** Proposed mechanisms upon pyrolysis of epoxidized C<sub>60</sub> [200]. Route 1 is a mechanism for two oxygen atoms on C<sub>60</sub>. Route 2 is a mechanism for three oxygen atoms on C<sub>60</sub>.

### 3.2.7 Evidence of an absence of cross-linked C<sub>60</sub>

Figure 3-14 shows the HRTEM images of  $C_{60}$  and E50-P inserted inside SWCNTs. E50-P was clearly inserted inside SWCNTs. It is the evidence of the absence of cross-linked  $C_{60}$ , because cross-linked  $C_{60}$  cannot be inserted to SWCNTs. Figure 3-15 shows the XRD patterns of  $C_{60}$ , E300, and E300-P. The  $C_{60}$  molecules have a well-defined crystal structure with three sharp peaks at  $2\theta = 10.8, 17.6,$  and  $20.7$  degrees. The peak intensity of  $C_{60}$  was lowered after epoxidation (E300) because of the introduction of functional groups and the intensity was recovered after heat treatment (E300-P). It also indicates that cross-linking between epoxidized  $C_{60}$  did not proceed by heat treatment.

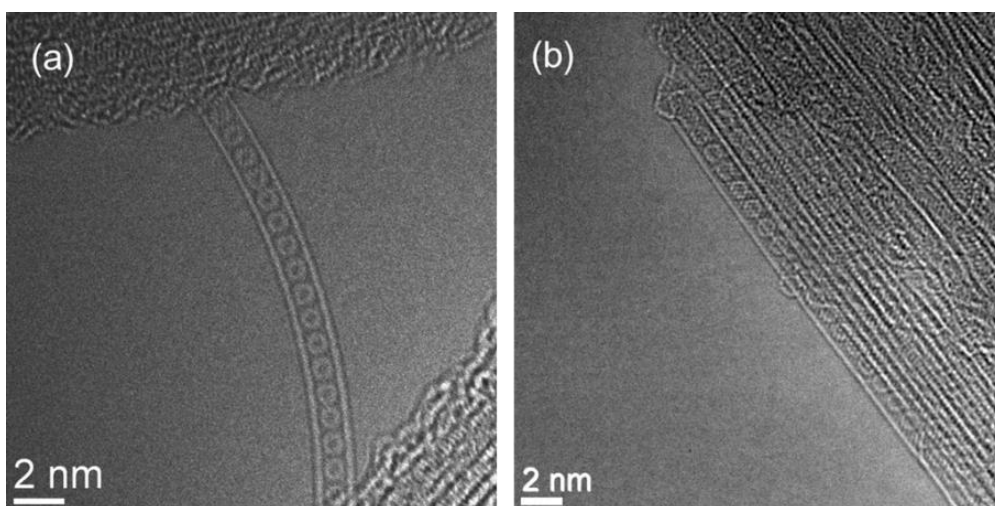


**Figure 3-14** HRTEM images of (a)  $C_{60}$  and (b) E50-P inserted inside SWCNTs.

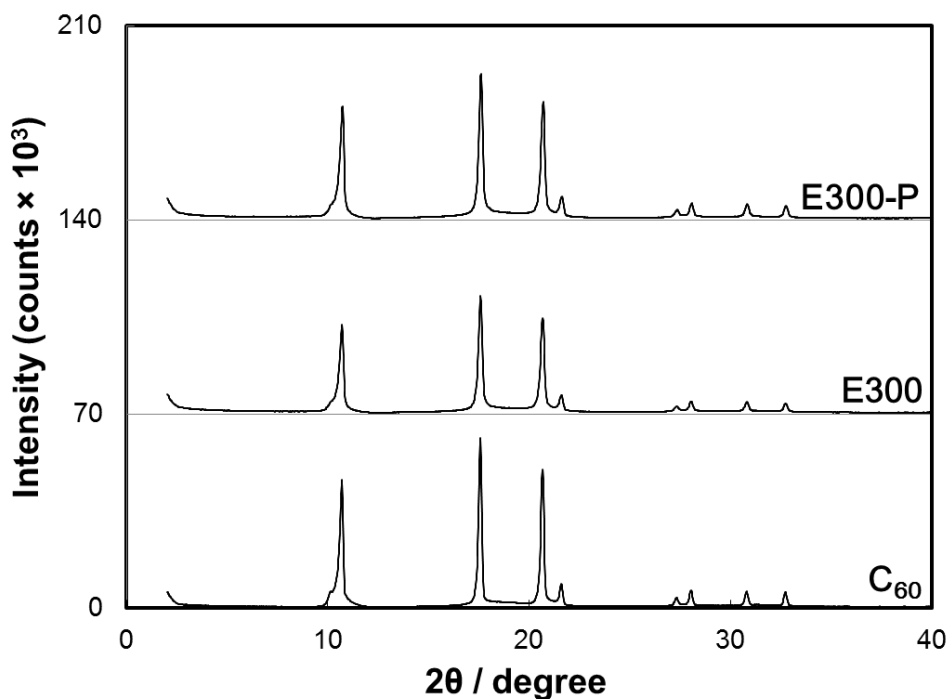


**Figure 3-15** XRD patterns of  $C_{60}$ , E300, and E300-P.

### 3.3 Oxygen migration and selective CO and $CO_2$ formation from epoxidized fullerenes

#### 3.3.1 Migration of oxygen atom(s)

Migrations of one oxygen atom from hexagon-hexagon (X1) to the next pentagon-hexagon (X3) and from pentagon-hexagon (X3) to the next pentagon-hexagon (X5) on  $C_{60}$  are shown in Fig. 3-16a. The activation energy from X1 to X3 and that from X3 to X5 are 210.1 and 218.2  $\text{kJ mol}^{-1}$ , respectively. Radovic et al. have reported that migration of one oxygen atom on  $C_{42}H_{16}$  graphene requires activation energy of 94.1  $\text{kJ mol}^{-1}$  [168]. It indicates that migration of one oxygen atom on  $C_{60}$  is more difficult to proceed than that on graphene.

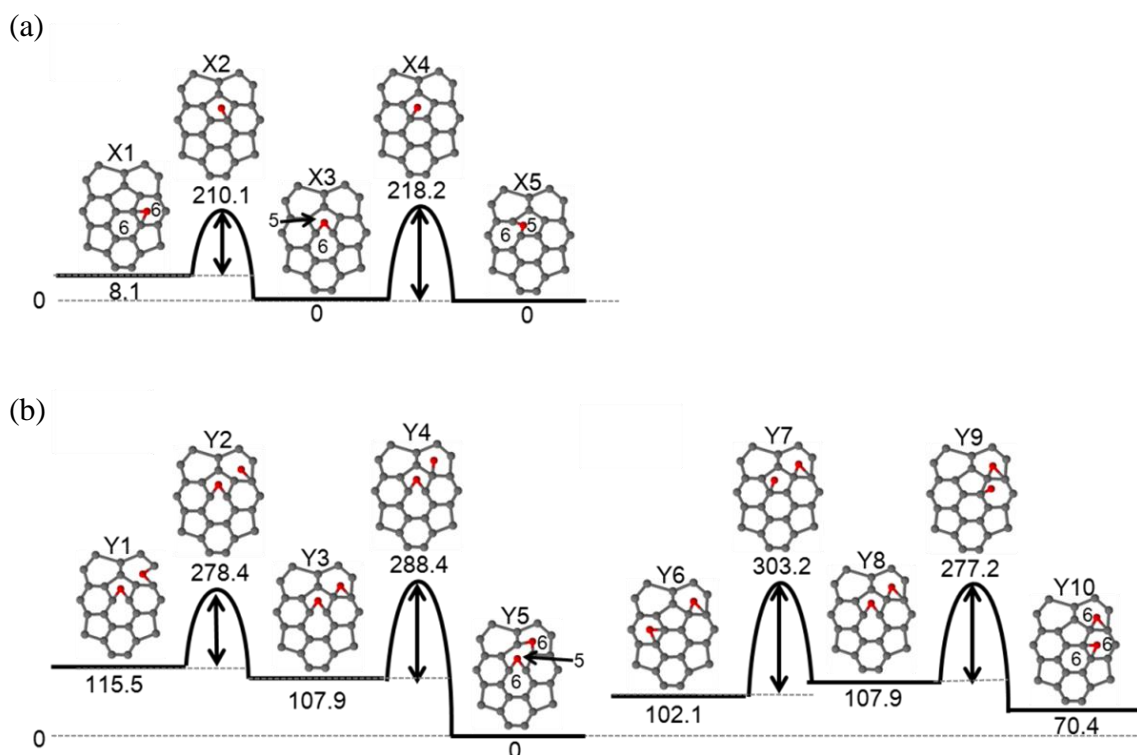


**Figure 3-16** Mechanisms for migration of one oxygen atom on C<sub>60</sub>. (a) Migration of one oxygen atom. Energies (in kJ mol<sup>-1</sup>) written under each structure are energies relative to energies of X3 and X5. (b) Migration of one oxygen atom with another fixed oxygen atom. Energies (in kJ mol<sup>-1</sup>) written under each structure are energies relative to energy of Y5. (Carbon: Gray spheres. Oxygen: Red spheres.)

Figure 3-16b shows migrations of one oxygen atom out of two oxygen atoms on C<sub>60</sub>. There are two mechanisms for migration of one oxygen atom out of two oxygen atoms. One of the mechanisms (b1 in Fig. 3-16) is migration of one oxygen atom out of two isolated oxygen atoms (Y1). Two oxygen atoms next to each other on pentagon-hexagon (Y5) are formed from Y1 at maximum activation energy of 288.4 kJ mol<sup>-1</sup>. Another mechanism (b2 in Fig. 3-16) is migration of one oxygen atom out of two isolated oxygen atoms (Y6). Two oxygen atoms next to each other on hexagon-hexagon (Y10) are formed from Y6 at maximum activation energy of 303.2 kJ mol<sup>-1</sup>. The energies of two oxygen atoms next to each other such as Y5 and Y10 are 115.5 and 31.7 kJ mol<sup>-1</sup> lower than those of two isolated oxygen atoms such as Y1 and Y6, respectively. Thus, soon after migration starts, a clustering of two oxygen atoms proceeds.

### 3.3.2 Pyrolysis of one oxygen atom on C<sub>60</sub>

Pyrolysis of one oxygen atom on C<sub>60</sub> brings only one proposed final structure consisting of one mono-vacancy defect (MV) and a CO gas (Fig. 3-17). The formation of a CO gas from one oxygen atom on graphene has been reported to be strongly endothermic (610 kJ mol<sup>-1</sup>) [169]. Similarly, the formation of the CO gas on C<sub>60</sub> was also strongly endothermic (502.8 kJ mol<sup>-1</sup>). It shows that the formation energy of MV on C<sub>60</sub> is lower than that on graphene. Ma et al. reported that the length of a C-C bond between two carbon atoms on a pentagon ring at MV on graphene is 2.02 Å, which is longer than that of standard length of 1.42 Å for graphene, indicating that the bonding of two carbon atoms is weak [203]. In case of C<sub>60</sub>, the length of two carbon atoms on a pentagon rings at MV in Fig. 3-17 was 1.52 Å, which is shorter than that of graphene, decreasing the energy of MV on C<sub>60</sub> compared to that on graphene. The formation energy of MV (502.8 kJ mol<sup>-1</sup>) is much higher than the activation energy required for migration of an oxygen atom (218.2 kJ mol<sup>-1</sup>) (Fig. 3-16a). Thus, migration of an oxygen atom preferentially proceeds rather than the formation of the CO gas from one oxygen atom on C<sub>60</sub>.

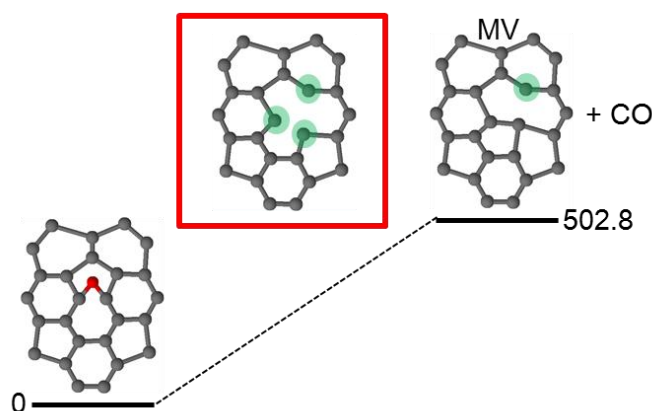


**Figure 3-17** Formation of a CO gas from one oxygen atom on C<sub>60</sub>. Relative energies in kJ mol<sup>-1</sup> are written under each structure. (Carbon: Gray spheres. Oxygen: Red sphere.) Carbon atoms marked by green spheres indicate the carbene sites.

### 3.3.3 Pyrolysis of two oxygen atoms on C<sub>60</sub>

#### 3.3.3.1 Two types of intermediates

Two oxygen atoms next to each other on C<sub>60</sub> were constructed to elucidate the

mechanisms for pyrolysis of two oxygen atoms on  $C_{60}$  as shown in Fig. 3-18. The relative energies of epoxidized  $C_{60}$  are shown below each structure. These structures were labelled with numbers depending on the number of oxygen atoms.  $2A_1$  is the most stable structure among  $2A_1$ - $2A_5$ . From these two oxygen atoms on  $C_{60}$  ( $2A_1$ - $2A_5$ ), two types of intermediates (C-O-C-O-C ( $2B_1$  and  $2B_2$ ) and C-O-O-C ( $2C_1$  and  $2C_2$ )) are formed by pyrolysis (Fig. 3-19).

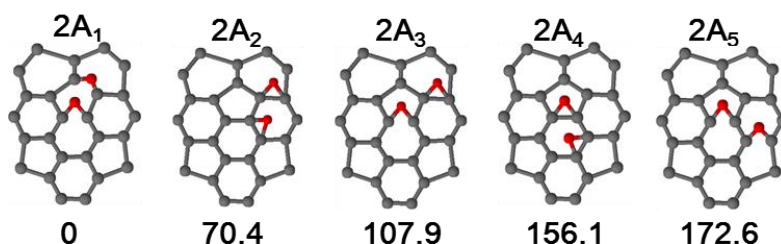


**Figure 3-18** Structures of two oxygen atoms next to each other on  $C_{60}$ . Energies (in  $\text{kJ mol}^{-1}$ ) written under each structure are energies relative to energy of  $2A_1$ . (Carbon: Gray spheres. Oxygen: Red spheres.)

One type of the intermediate (C-O-C-O-C groups ( $2B_1$  and  $2B_2$ )) out of two types of the intermediates is formed by migration of one oxygen atom out of two oxygen atoms (Fig. 3-19). Both  $2A_1$  and  $2A_3$  are converted into  $2B_1$  containing two unzipped epoxides on pentagon-hexagon.  $2A_2$ ,  $2A_3$ ,  $2A_4$ , and  $2A_5$  are converted into  $2B_2$  containing one unzipped epoxide on pentagon-hexagon and one epoxide on hexagon-hexagon. The intermediate C-O-C-O-C groups ( $2B_1$  and  $2B_2$ ) are converted into two types of lactone groups (shown in sections 3.3.3.2 and 3.3.3.3) and both lactone groups decompose into either a CO gas or a  $\text{CO}_2$  gas.

Another intermediate (C-O-O-C groups ( $2C_1$  and  $2C_2$ )) is formed by the bonding of two oxygen atoms on  $C_{60}$ .  $2A_1$ ,  $2A_2$ , and  $2A_3$  are converted into  $2C_1$  containing a C-O-O-C group on pentagon-hexagon.  $2A_4$  and  $2A_5$  are converted into  $2C_2$  containing a C-O-O-C group on hexagon-hexagon. A C-O-O-C group ( $2C_1$  and  $2C_2$ ) generates an  $\text{O}_2$  gas.

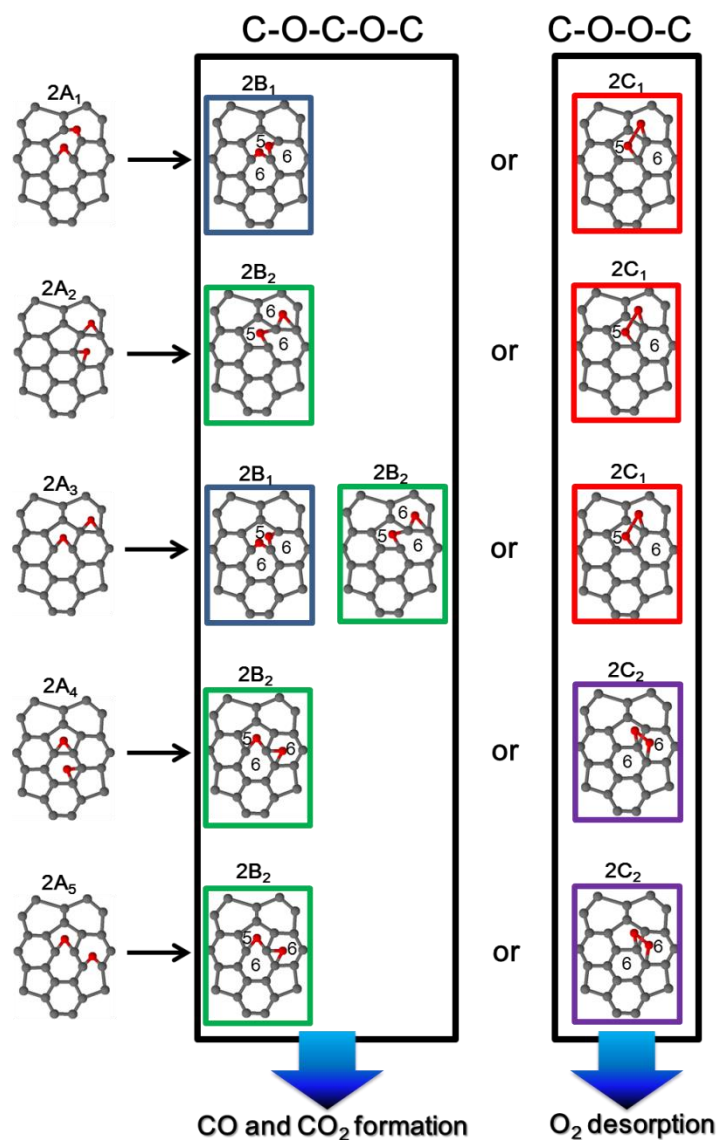


**Figure 3-19** Two types of intermediates formed by pyrolysis of 2A<sub>1</sub>-2A<sub>5</sub>. 2B<sub>1</sub> and 2B<sub>2</sub> include a C-O-C-O-C group. 2C<sub>1</sub> and 2C<sub>2</sub> include a C-O-O-C group. (Carbon: Gray spheres. Oxygen: Red spheres.)

### 3.3.3.2 Pyrolysis of 2A<sub>1</sub>

Figure 3-20a and b shows the proposed mechanisms for pyrolysis of 2A<sub>1</sub> and its energy diagram, respectively. The mechanism for pyrolysis of 2A<sub>1</sub> was used because 2A<sub>1</sub> is the most stable structure among 2A<sub>1</sub>-2A<sub>5</sub> in Fig. 3-18. Total electron energies of structures with a carbene site such as MV, 1A, and 2D<sub>1</sub> (carbene sites are marked by

green spheres in Fig. 3-20a) were calculated for both  $M=1$  and  $M=3$ . The total electron energy of MV ( $M = 3$ ) is  $14.0 \text{ kJ mol}^{-1}$  lower than that of MV ( $M = 1$ ). On the other hand, total electron energies of 1A and  $2D_1$  ( $M = 3$ ) are  $65.4$  and  $131 \text{ kJ mol}^{-1}$  higher than those of 1A and  $2D_1$  ( $M = 1$ ), respectively. Thus,  $M = 3$  was used for MV, whereas  $M = 1$  was used for 1A and  $2D_1$  in Fig. 3-20b.

R1 in Fig. 3-20a is a route for the formation of a CO gas (1A) and a CO<sub>2</sub> gas (MV) via migration of one oxygen atom toward one fixed oxygen atom ( $2A_1$  to  $2B_1$ ). By migration of one oxygen atom on  $2A_1$ , a C-O-C-O-C group ( $2B_1$ ) and a lactone group ( $2D_1$ ) are formed. Pyrolysis of the lactone group ( $2D_1$ ) proceeds via R1-1 and R1-2. R1-1 involves transformation of the lactone group ( $2D_1$ ) into a combination of an ether group and a ketone group ( $2E_1$ ) by bonding an ether group in a lactone group (C-O-C=O) with a carbene site ( $2D_1$  to  $2E_1$ ). Moreover, a CO gas is formed by pyrolysis of a ketone group ( $2E_1$ ), generating a combination of a carbene site and an ether group (1A). R1-2 involves the formation of CO<sub>2</sub> gas from the lactone group and a carbene site ( $2D_1$ ). Importance of R1 is the formation of a carbene site on both 1A and MV. The existence of both a carbene site and a vacancy defect causes energetic destabilization. The formation energy of a combination of 1A and the CO gas is  $47.0 \text{ kJ mol}^{-1}$  lower than that of a combination of MV and the CO<sub>2</sub> gas, indicating that the carbene site in 1A is stabilized by the presence of an oxygen atom. This stabilization can be explained by decrease of electron density at the carbene site in the presence of the neighboring oxygen atom with the high electronegativity [150].

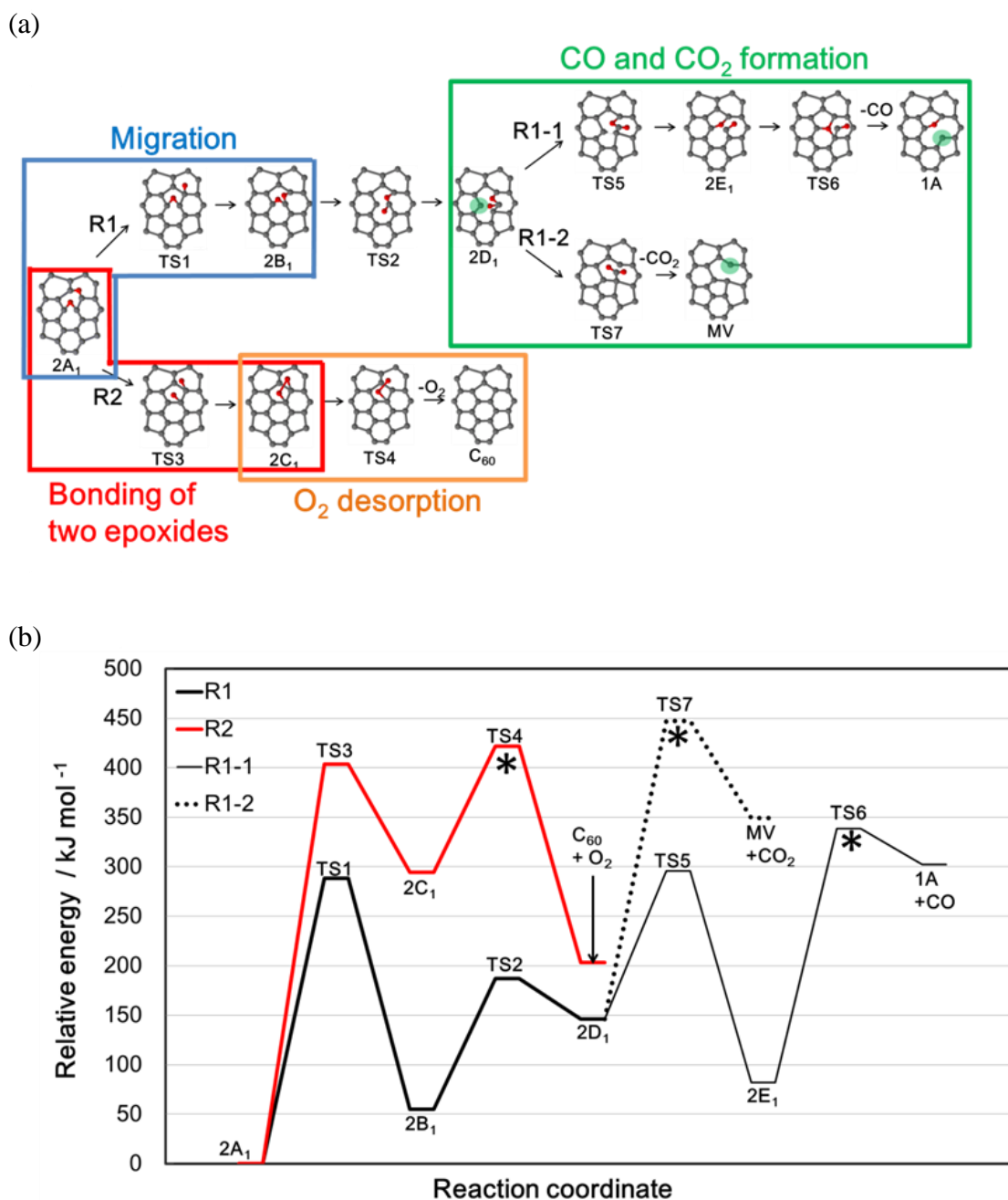


**Figure 3-20** Proposed mechanisms and the corresponding energy diagram for pyrolysis of two oxygen atoms on C<sub>60</sub> (2A<sub>1</sub>). (a) Proposed mechanisms for pyrolysis of 2A<sub>1</sub>. (Carbon: Gray spheres. Oxygen: Red spheres.) Carbon atoms marked by green spheres indicate carbene sites. (b) Energy diagram of R1 (black bold line), R2 (red line), R1-1 (black thin line), and R1-2 (black dotted line). Asterisks indicate the transition states with the highest energy on each route to determine the apparent activation energies for each route. The energy of 2A<sub>1</sub> was set as 0 kJ mol<sup>-1</sup>.

R2 is a route for desorption of an O<sub>2</sub> gas via bonding of two oxygen atoms on C<sub>60</sub> (2A<sub>1</sub>). One out of two C-O bondings in 2C<sub>1</sub> is cleaved (TS4) and one O<sub>2</sub> gas desorbed. Desorption of the O<sub>2</sub> gas does not generate any defects on C<sub>60</sub> in contrast to the formation of the CO gas and the CO<sub>2</sub> gas, which generates defects on C<sub>60</sub>.

All of mechanisms for the formation of the CO gas, the CO<sub>2</sub> gas, and the O<sub>2</sub> gas (Fig. 3-20) are endothermic reactions. The formation energies for the CO gas, the CO<sub>2</sub> gas, and the O<sub>2</sub> gas are 302.4, 349.4, and 203.4 kJ mol<sup>-1</sup>, respectively. The apparent activation energies for the formation of the CO gas, the CO<sub>2</sub> gas, and the O<sub>2</sub> gas are 338.5, 447.3, and 421.9 kJ mol<sup>-1</sup>, respectively. Here, the apparent activation energies mean the energy differences between the energy of 2A<sub>1</sub> and the highest activation energies, which were marked by an asterisk, among all of transition states for each route in Fig. 3-5b. This result indicates that the CO gas tends to form more than the O<sub>2</sub> gas and the CO<sub>2</sub> gas by pyrolysis of 2A<sub>1</sub>.

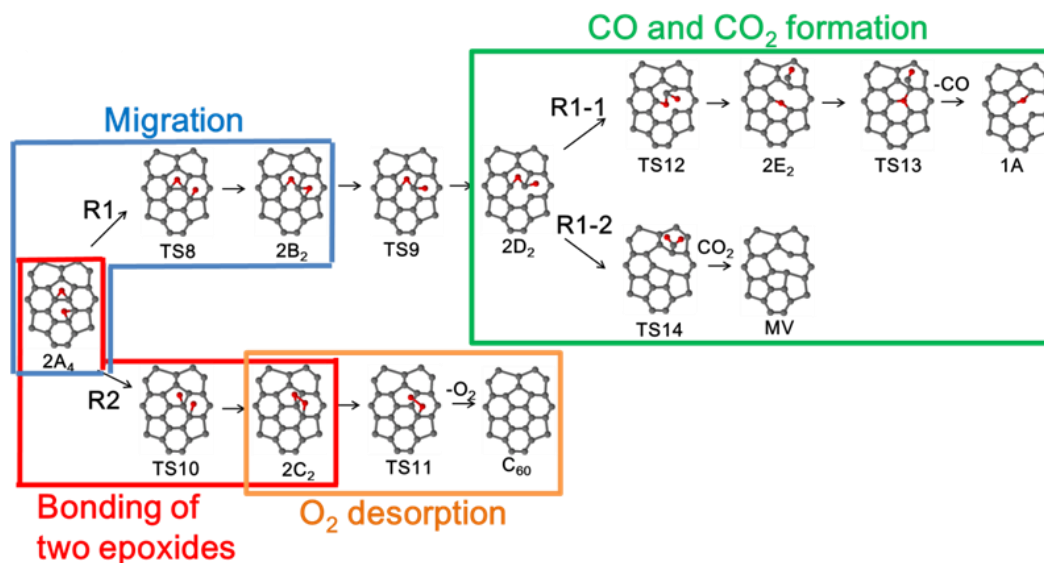
Activation energies for migration of one oxygen atom out of two oxygen atoms (277.2 ~ 303.2 kJ mol<sup>-1</sup>, Fig. 3-1b) are lower than those for the formation of the CO gas, the CO<sub>2</sub> gas, and the O<sub>2</sub> gas from 2A<sub>1</sub>. Thus, migration of one oxygen atom proceeds prior to the formation of these gases. Oxygen atoms in 2A<sub>1</sub> migrate and 2A<sub>2</sub>-2A<sub>5</sub> form (Fig. 3-18). The oxygen atoms in 2A<sub>2</sub>-2A<sub>5</sub> may migrate back to 2A<sub>1</sub>. It means that all of 2A (2A<sub>1</sub>-2A<sub>5</sub>) have a possibility to generate these gases.

### 3.3.3.3 Pyrolysis of 2A<sub>4</sub>

Figure 3-21a and b shows the proposed mechanisms for pyrolysis of 2A<sub>4</sub> and its energy diagram, respectively. The mechanism for pyrolysis of 2A<sub>4</sub> was used because 2A<sub>4</sub> is the initial structure to transform into both 2B<sub>2</sub> and 2C<sub>2</sub> (Figs. 3-19 and 3-21a). Although 2A<sub>5</sub> can also be transformed into both 2B<sub>2</sub> and 2C<sub>2</sub> (Fig. 3-19), the energy of 2A<sub>5</sub> is higher than that of 2A<sub>4</sub> (Fig. 3-18). Other structures such as 2A<sub>2</sub> and 2A<sub>3</sub> in Fig. 3-19 are not transformed into both 2B<sub>2</sub> and 2C<sub>2</sub>. R1 in Fig. 3-21a is a route for the formation of a CO gas (2A<sub>4</sub> to 1A) and a CO<sub>2</sub> gas (2A<sub>4</sub> to MV) via migration of an oxygen atom toward one fixed oxygen atom (2A<sub>4</sub> to 2B<sub>2</sub>), whereas R2 is a route for desorption of an O<sub>2</sub> gas (2A<sub>4</sub> to C<sub>60</sub>) via bonding of two epoxides (2A<sub>4</sub> to 2C<sub>2</sub>). Pyrolysis of a lactone group (2D<sub>2</sub>) proceeds via R1-1 and R1-2. R1-1 involves transformation from the lactone group (2D<sub>2</sub>) to a combination of an ether group and a ketone group (2E<sub>2</sub>). The ketone group (2E<sub>2</sub>) decomposes and a CO gas and a combination of a carbene site and an ether group (1A) are formed. R1-2 involves decomposition of a lactone group (2D<sub>2</sub>) and the formation of CO<sub>2</sub> gas and MV.

All of mechanisms for the formation of a CO gas, a CO<sub>2</sub> gas, and an O<sub>2</sub> gas from 2A<sub>4</sub> are endothermic reactions. The formation energies of the CO gas, the CO<sub>2</sub> gas, and the O<sub>2</sub> gas are 302.4, 349.4, and 203.4 kJ mol<sup>-1</sup>, respectively. The apparent activation energies for the formation of the CO gas, the CO<sub>2</sub> gas, and the O<sub>2</sub> gas are 366.3, 462.2, and 412.3 kJ mol<sup>-1</sup>, respectively. In a similar way to pyrolysis of 2A<sub>1</sub>, this result indicates that the CO gas tends to form from 2A<sub>4</sub> more than the O<sub>2</sub> gas and the CO<sub>2</sub> gas.

(a)



(b)

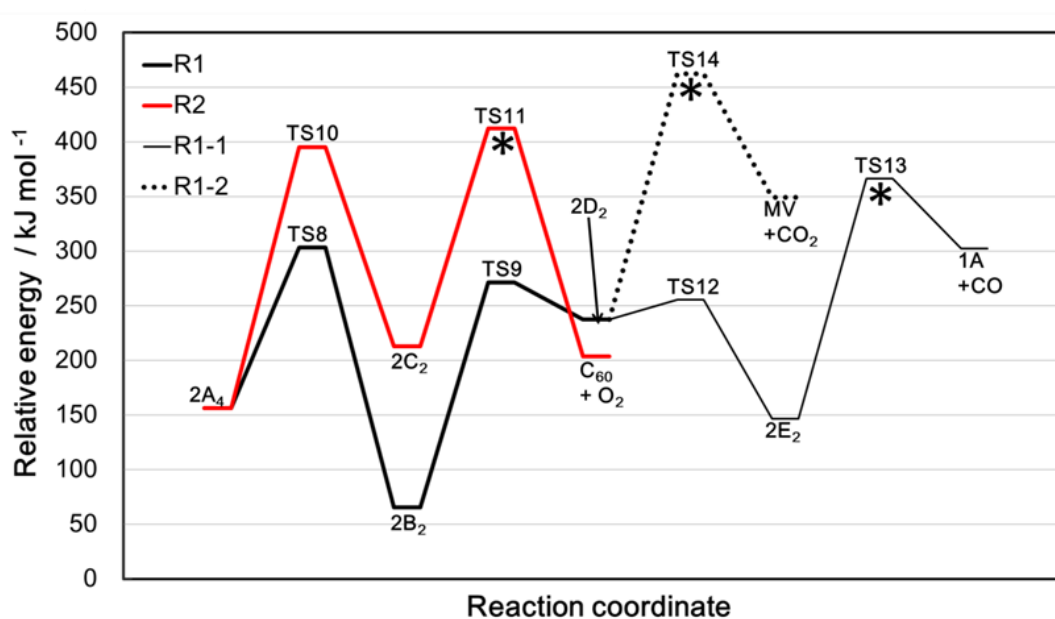


**Figure 3-21** Proposed mechanisms and the corresponding energy diagram for pyrolysis of two oxygen atoms on C<sub>60</sub> (2A<sub>4</sub>). (a) Proposed mechanisms for pyrolysis of 2A<sub>4</sub>. (Carbon: Gray spheres. Oxygen: Red spheres.) (b) Energy diagram of R1 (black bold line), R2 (red line), R1-1 (black thin line), and R1-2 (black dotted line). Asterisks indicate the transition states with the highest energy on each route to determine the apparent activation energies. The energy of 2A<sub>1</sub> in Fig. 3-20 was set as 0 kJ mol<sup>-1</sup>.

#### 3.3.3.4 Comparison for pyrolysis of 2A<sub>1</sub> and 2A<sub>4</sub>

Apparent activation energies to form a CO gas, a CO<sub>2</sub> gas, and an O<sub>2</sub> gas directly from 2A<sub>1</sub> are 338.5 (TS6 in Fig. 3-20b), 447.3 (TS7 in Fig. 3-20b), and 421.9 (TS4 in Fig. 3-20b) kJ mol<sup>-1</sup>, respectively. Apparent activation energies to form the CO gas, the CO<sub>2</sub> gas, and the O<sub>2</sub> gas from 2A<sub>1</sub> via 2A<sub>4</sub> are 366.3 (TS13 in Fig. 3-21b), 462.2 (TS14 in Fig. 3-21b), and 412.3 (TS11 in Fig. 3-21b) kJ mol<sup>-1</sup>, respectively. Comparing these activation energies, both the CO gas and the CO<sub>2</sub> gas are mainly formed from 2A<sub>1</sub> rather than 2A<sub>4</sub>, whereas the O<sub>2</sub> gas is mainly formed from 2A<sub>4</sub> rather than 2A<sub>1</sub>.

Figure 3-22 shows a short summary of energy differences of intermediates such as a C-O-C-O-C group, a lactone group, a combination of an ether group and a ketone group, and a C-O-O-C group on C<sub>60</sub> in Figs. 3-20 and 3-21. 2A<sub>1</sub> is transformed into 2B<sub>1</sub>, 2D<sub>1</sub>, 2E<sub>1</sub>, and 2C<sub>1</sub>. 2A<sub>4</sub> is transformed into 2B<sub>2</sub>, 2D<sub>2</sub>, 2E<sub>2</sub>, and 2C<sub>2</sub>. 2B<sub>1</sub>, 2B<sub>2</sub>, 2D<sub>1</sub>, 2D<sub>2</sub>, 2E<sub>1</sub>, and 2E<sub>2</sub> are intermediates for the formation of either a CO gas or a CO<sub>2</sub> gas, whereas both 2C<sub>1</sub> and 2C<sub>2</sub> are intermediates for desorption of an O<sub>2</sub> gas. The relative energies of 2B<sub>1</sub>, 2D<sub>1</sub>, and 2E<sub>1</sub> are 10.8, 91.4, and 64.9 kJ mol<sup>-1</sup> lower than those of 2B<sub>2</sub>, 2D<sub>2</sub>, and 2E<sub>2</sub>, respectively. It implies that 2A<sub>1</sub> tends to generate the CO gas and the CO<sub>2</sub> gas more than 2A<sub>4</sub>. The relative energy of 2C<sub>2</sub> (a C-O-O-C group on hexagon-hexagon) is 81.6 kJ mol<sup>-1</sup> lower than that of 2C<sub>1</sub> (a C-O-O-C group on pentagon-hexagon). It implies that 2A<sub>4</sub> tends to generate the O<sub>2</sub> gas more than 2A<sub>1</sub>. From the point of view of both apparent activation energies and formation energies, the CO gas and the CO<sub>2</sub> gas tend to form from 2A<sub>1</sub> and the O<sub>2</sub> gas tends to form from 2A<sub>4</sub>.

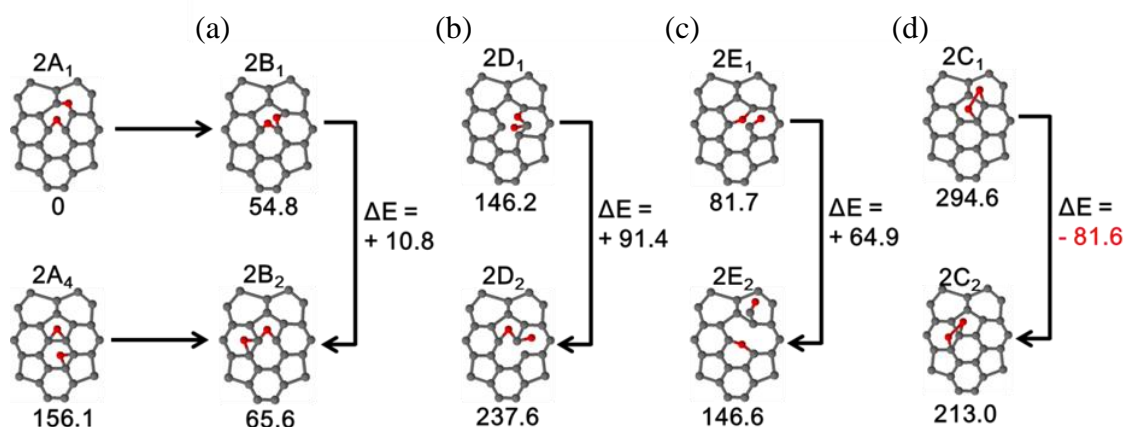


**Figure 3-22** Energy differences of intermediates originating from two oxygen atoms on  $C_{60}$ . (a) C-O-C-O-C groups ( $2B_1$  and  $2B_2$ ). (b) Lactone groups ( $2D_1$  and  $2D_2$ ). (c) Combinations of an ether group and a ketone groups ( $2E_1$  and  $2E_2$ ). (d) C-O-O-C groups ( $2C_1$  and  $2C_2$ ). Energies (in  $\text{kJ mol}^{-1}$ ) written under each structure are energies relative to the energy of  $2A_1$ . (Carbon: Gray spheres. Oxygen: Red spheres.)

### 3.3.4 Pyrolysis of three oxygen atoms on $C_{60}$

#### 3.3.4.1 Three types of intermediates

Three oxygen atoms next to each other on  $C_{60}$  were constructed (Fig. 3-23) to compare with the mechanisms for pyrolysis of two oxygen atoms next to each other on  $C_{60}$ . The energies of three oxygen atoms on  $C_{60}$  relative to that of  $3A_1$  are shown below each structure.  $3A_1$  is the most stable structure among  $3A_1$ - $3A_6$ . In a similar way to pyrolysis of two oxygen atoms on  $C_{60}$  (Fig. 3-19), three oxygen atoms on  $C_{60}$  ( $3A_1$ - $3A_6$ ) form C-O-C-O-C groups and C-O-O-C groups.

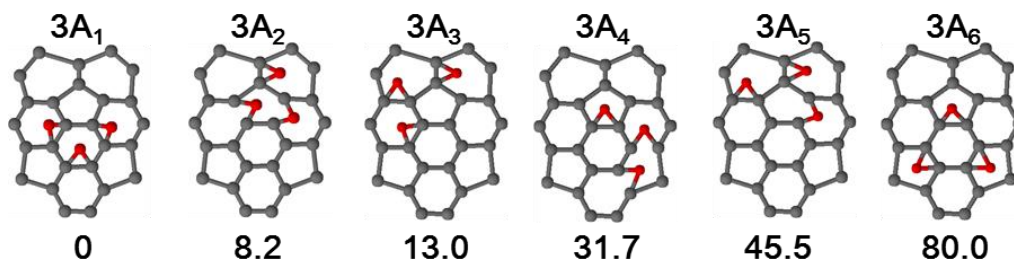


**Figure 3-23** Structures of three oxygen atoms next to each other on  $C_{60}$ . Energies (in  $\text{kJ mol}^{-1}$ ) written under each structure are energies relative to the energy of  $3A_1$ . (Carbon: Gray spheres. Oxygen: Red spheres.)

Figure 3-24 shows energy differences of three types of intermediates such as C-O-C-O-C-O-C groups ( $3C_1$  and  $3C_2$ ), combinations of a lactone group and a ketone group ( $3D_1$  and  $3D_2$ ), and combinations of a C-O-O-C group and an oxygen atom ( $3G_1$  and  $3G_2$ ). Either  $3C_1$  or  $3C_2$  is formed from  $3A_1$ - $3A_6$  by migration of oxygen atoms.  $3D_1$  and  $3D_2$  (combinations of the lactone group and the ketone group) are formed from  $3C_1$  and  $3C_2$  (C-O-C-O-C-O-C groups), respectively.  $3G_1$  and  $3G_2$  include one C-O-O-C group and either one epoxide or one unzipped epoxide. Either  $3G_1$  or  $3G_2$  is formed from  $3A_1$ - $3A_6$  by bonding two oxygen atoms.  $3C_1$ ,  $3C_2$ ,  $3D_1$ , and  $3D_2$  are intermediates for the formation of CO and CO<sub>2</sub> gases, whereas  $3G_1$  and  $3G_2$  are intermediates for desorption of O<sub>2</sub> gas.

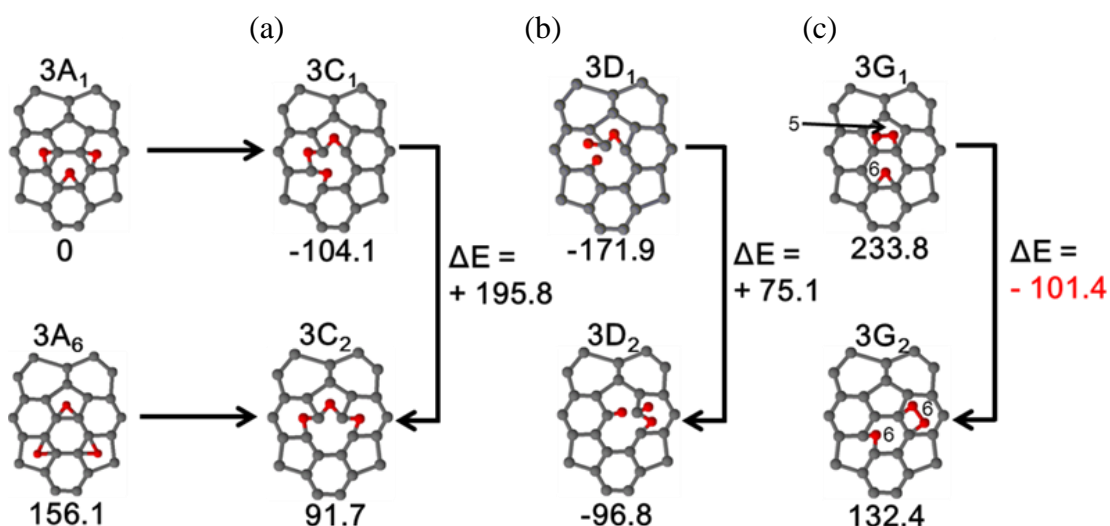


**Figure 3-24** Three types of intermediates originating from three oxygen atoms on C<sub>60</sub>. (a) C-O-C-O-C-O-C groups ( $3C_1$  and  $3C_2$ ). (b) Combinations of a lactone group and a ketone group ( $3D_1$  and  $3D_2$ ). (c) Combinations of a C-O-O-C group and either one epoxide or one unzipped epoxide ( $3G_1$  and  $3G_2$ ). Energies (kJ mol<sup>-1</sup>) written under each structure were energies relative to the energy of  $3A_1$ . (Carbon: Gray spheres. Oxygen: Red spheres.)

The relative energies of  $3C_1$  and  $3D_1$  are 195.8 and 75.1 kJ mol<sup>-1</sup> lower than those of  $3C_2$  and  $3D_2$ , respectively (Fig. 3-24). It indicates that the possibility of existence of  $3C_1$  and  $3D_1$  is higher than that of  $3C_2$  and  $3D_2$ , respectively. Because both  $3C_1$  and  $3D_1$  are formed from  $3A_1$  by migration of oxygen atoms and  $3A_1$  is the most

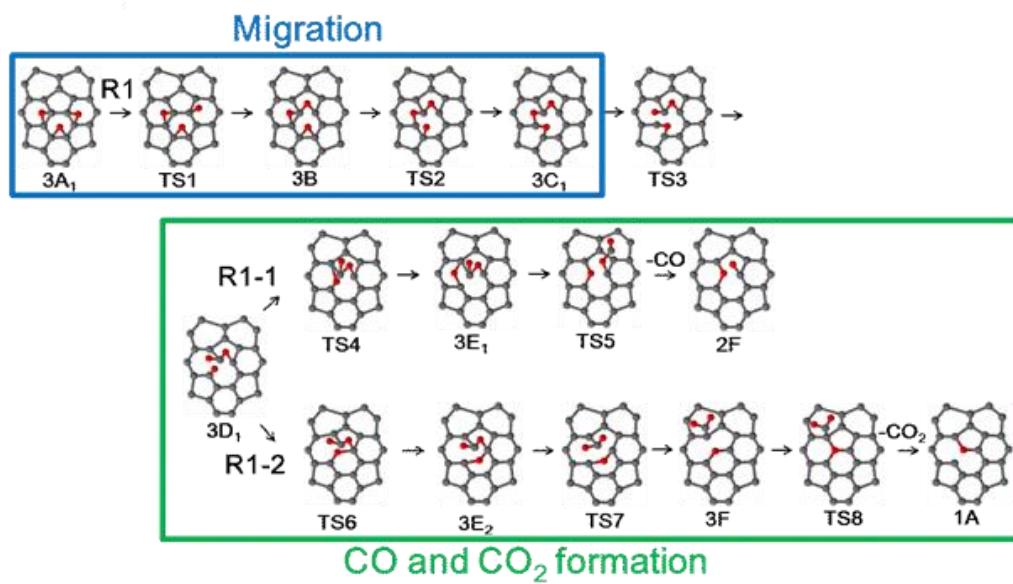
stable structure among  $3A_1$ - $3A_6$ , only  $3A_1$  was selected as an initial structure for the formation of a CO gas and a CO<sub>2</sub> gas. The energy of  $3G_2$  (a C-O-O-C group on hexagon-hexagon) is 101.4 kJ mol<sup>-1</sup> lower than that of  $3G_1$  (a C-O-O-C group on pentagon-hexagon) (Fig. 3-24), indicating that a C-O-O-C group tends to be introduced on hexagon-hexagon ( $3G_2$ ) rather than pentagon-hexagon ( $3G_1$ ). This tendency is similar to the case of two oxygen atoms on C<sub>60</sub> because positions of C-O-O-C groups of  $3G_1$  and  $3G_2$  are same as those of  $2C_1$  and  $2C_2$ , respectively. Moreover, the apparent activation energies for desorption of an O<sub>2</sub> gas via  $2C_1$  and  $2C_2$  are 421.9 and 412.3 kJ mol<sup>-1</sup>, respectively (Figs. 3-20 and 3-21). Thus, the possibility of the existence of  $3G_2$  is higher than that of  $3G_1$  for desorption of the O<sub>2</sub> gas. Because  $3G_2$  is formed from  $3A_6$  by bonding two oxygen atoms, only  $3A_6$  was selected as an initial structure among three oxygen atoms on C<sub>60</sub> ( $3A_1$ - $3A_6$ ) for desorption of the O<sub>2</sub> gas.

### 3.3.4.2 Formation of a CO gas and a CO<sub>2</sub> gas

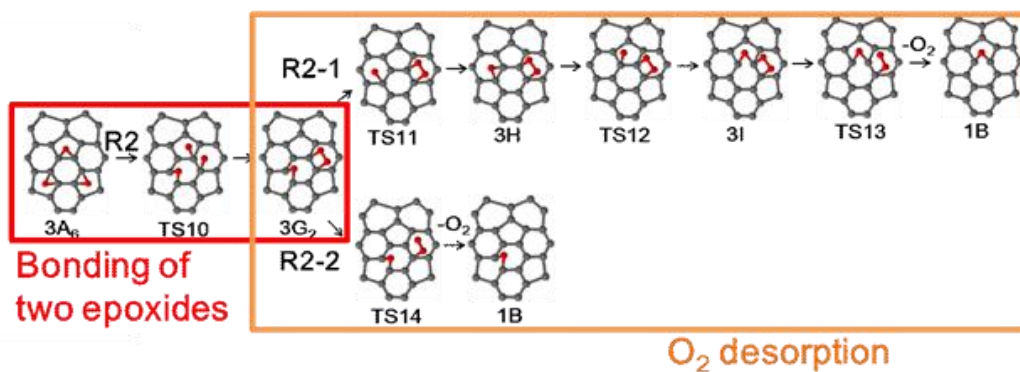
R1 (Fig. 3-25a1 and b) is a route for the formation of the CO gas and the CO<sub>2</sub> gas via migration of two oxygen atoms toward one fixed oxygen atom ( $3A_1$  to  $3C_1$ ). A combination of a lactone group and a ketone group ( $3D_1$ ) is formed from a C-O-C-O-C-O-C group ( $3C_1$ ). Pyrolysis of  $3D_1$  (Fig. 3-25a1 and b) proceeds via R1-1 and R1-2. R1-1 involves the formation of 2F and the CO gas, whereas R1-2 involves the formation of 1A and the CO<sub>2</sub> gas.

The structure  $3A_1$  is gradually stabilized as migration proceeds ( $3A_1$  to  $3D_1$  in Fig. 3-25a1 and b), indicating that migration from  $3A_1$  to  $3D_1$  is an exothermic reaction with the apparent activation energy of 222.6 kJ mol<sup>-1</sup> ( $3A_1$  to  $3D_1$  in Fig. 3-25b). The energy of  $3D_1$  is 171.9 kJ mol<sup>-1</sup> lower than that of  $3A_1$ , indicating that  $3D_1$  is the most stable structure in R1. Pyrolysis of lactone groups ( $2D_1$  and  $2D_2$ ) formed from two oxygen atoms on C<sub>60</sub> ( $2A_1$  and  $2A_4$ ) generates unstable carbene sites (Figs. 3-20 and 3-21), whereas pyrolysis of a combination of a lactone group and a ketone group ( $3D_1$ ) formed from three oxygen atoms on C<sub>60</sub> ( $3A_1$ ) does not generate a carbene site because of the existence of the ketone group in  $3D_1$  (Figs. 3-24b and 3-25a1), indicating that the stability of  $3D_1$  is attributed to the absence of the carbene site.

(a1)



(a2)



(b)

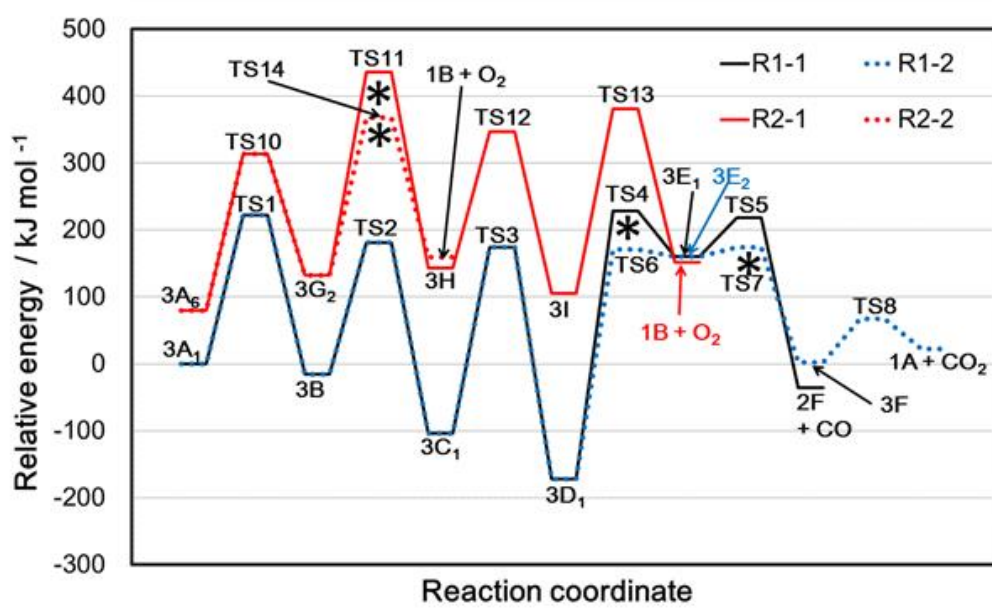


**Figure 3-25** Proposed mechanisms and energy diagram for pyrolysis of three oxygen atoms on  $C_{60}$ . (a) Proposed mechanisms for pyrolysis. (Carbon: Gray spheres. Oxygen: Red spheres.) (b) An energy diagram of R1-1 (black bold line), R1-2 (blue dotted line), R2-1 (red bold line), and R2-2 (red dotted line). Asterisks indicate the transition states with the highest energy on each route to determine the apparent activation energy. The energy of  $3A_1$  was set as  $0 \text{ kJ mol}^{-1}$ .

The structure  $3D_1$  is transformed into  $3E_1$  and  $3E_2$  (combinations of a lactone group and an ether group) via R1-1 and R1-2, respectively. The structural difference between  $3E_1$  and  $3E_2$  causes the difference of generated gases such as a CO gas and a  $CO_2$  gas, respectively. A carbon atom in the ether group bonded with C=O group in the lactone group, which is a C-O-C-(C=O)-O-C group ( $3E_1$ ), weakens the carbon-carbon bond between an ether group and a lactone group (C-O-C-(C=O)-O-C). The bonding accelerates the formation of a CO gas and a combination of an ether group and a ketone group (2F). The formation of 2F does not involve generation of a carbene site. On the other hand, a carbon atom in an ether group bonded with C-O-C in a lactone group, which is a C-O-C-O-C=O group ( $3E_2$ ), weakens the carbon-oxygen bond (C-O-C-O-C=O). This bonding accelerates the formation of a  $CO_2$  gas and 1A generates. The existence of the ether bonded with the lactone group ( $3E_1$  and  $3E_2$ ) weakens the bond with  $sp^3C$  such as C-O-C-C=O-O-C in  $3E_1$  and C-O-C-O-C=O in  $3E_2$ .

Although the relative energy of  $1A + CO_2$  ( $22.2 \text{ kJ mol}^{-1}$ ) (R1-2) is  $57.6 \text{ kJ mol}^{-1}$  higher than that of  $2F + CO$  ( $-35.5 \text{ kJ mol}^{-1}$ ) (R1-1) (Fig. 3-25b), R1-2 proceeds because the apparent activation energy of R1-2 from  $3D_1$  to 1A ( $346.2 \text{ kJ mol}^{-1}$  which is a difference between  $3D_1$  and TS7) is lower than that of R1-1 from  $3D_1$  to 2F ( $400.1 \text{ kJ mol}^{-1}$  which is a difference between  $3D_1$  and TS4). Especially, the activation energy from  $3D_1$  to TS6 ( $342.8 \text{ kJ mol}^{-1}$ ) is lower than that from  $3D_1$  to TS3 ( $345.8 \text{ kJ mol}^{-1}$ ), whereas the activation energy from  $3D_1$  to TS4 ( $400.1 \text{ kJ mol}^{-1}$ ) is higher than that from  $3D_1$  to TS3 ( $345.8 \text{ kJ mol}^{-1}$ ). It indicates that  $3E_2$  tends to form from  $3D_1$  and the  $CO_2$  gas tends to be generated more than the CO gas.

### 3.3.4.3 Desorption of an $O_2$ gas

R2 (Fig. 3-25a2 and b) is a route for desorption of an  $O_2$  gas (1B) via the bonding of two oxygen atoms ( $3A_6$  to  $3G_2$ ). Pyrolysis of  $3G_2$  proceeds via two mechanisms (R2-1 and R2-2) (Fig. 3-25a2 and b). R2-1 is a mechanism via the bonding

of one oxygen atom with a C-O-O-C group by migration of the oxygen atom. R2-2 is a mechanism via desorption of an O<sub>2</sub> gas from a C-O-O-C group which locates far from one oxygen atom.

R2-2 preferably proceeds rather than R2-1 because the apparent activation energy of R2-2 (539.6 kJ mol<sup>-1</sup> which is a difference between 3D<sub>1</sub> and TS14) is lower than that of R2-1 (608.0 kJ mol<sup>-1</sup> which is a difference between 3D<sub>1</sub> and TS11). Here, 3A<sub>6</sub> can be formed from 3A<sub>1</sub> by migration of oxygen atoms. That is the reason why the energy difference of 3D<sub>1</sub> and either TS14 or TS11 was used to obtain the apparent activation energy. However, desorption of an O<sub>2</sub> gas from three oxygen atoms on C<sub>60</sub> is difficult to proceed because the apparent activation energy for desorption of the O<sub>2</sub> gas is higher than those for the formation of a CO gas and a CO<sub>2</sub> gas. Because the CO<sub>2</sub> gas tends to form more than the CO gas as indicated in section 3.3.4.2, the CO<sub>2</sub> gas tends to form more than the O<sub>2</sub> gas and the CO gas by pyrolysis of three oxygen atoms on C<sub>60</sub>.

### 3.3.5 Summary of the formation of gases from two and three oxygen atoms on C<sub>60</sub>

Figure 3-26a and b shows summarized energy diagrams for pyrolysis of two (Figs. 3-20 and 3-21) and three (Fig. 3-25) oxygen atoms on C<sub>60</sub>, respectively. The formation of the CO gas, the CO<sub>2</sub> gas, and the O<sub>2</sub> gas from two oxygen atoms on C<sub>60</sub> endothermically proceeds (Fig. 3-26a). The CO gas tends to form more than the CO<sub>2</sub> gas and the O<sub>2</sub> gas from two oxygen atoms on C<sub>60</sub> because the apparent activation energy for the formation of the CO gas (E<sub>a</sub> (CO) in Fig. 3-26a) is the lowest among the formation of the CO gas (E<sub>a</sub> (CO) in Fig. 3-26a), the CO<sub>2</sub> gas (E<sub>a</sub> (CO<sub>2</sub>) in Fig. 3-26a), and the O<sub>2</sub> gas (E<sub>a</sub> (O<sub>2</sub>) in Fig. 3-26a). Three oxygen atoms on C<sub>60</sub> are transformed into a combination of a lactone group and a ketone group (3D<sub>1</sub> in Fig. 3-26b) and both the CO gas and the CO<sub>2</sub> gas are formed. The apparent activation energy for the formation of the CO<sub>2</sub> gas (E<sub>a</sub> (CO<sub>2</sub>) in Fig. 3-26b) is lower than those for the formation of the CO gas (E<sub>a</sub> (CO) in Fig. 3-26b) and the O<sub>2</sub> gas (E<sub>a</sub> (O<sub>2</sub>) in Fig. 3-26b). It indicates that the CO<sub>2</sub> gas tends to form more than the CO gas and the O<sub>2</sub> gas from three oxygen atoms on C<sub>60</sub>.

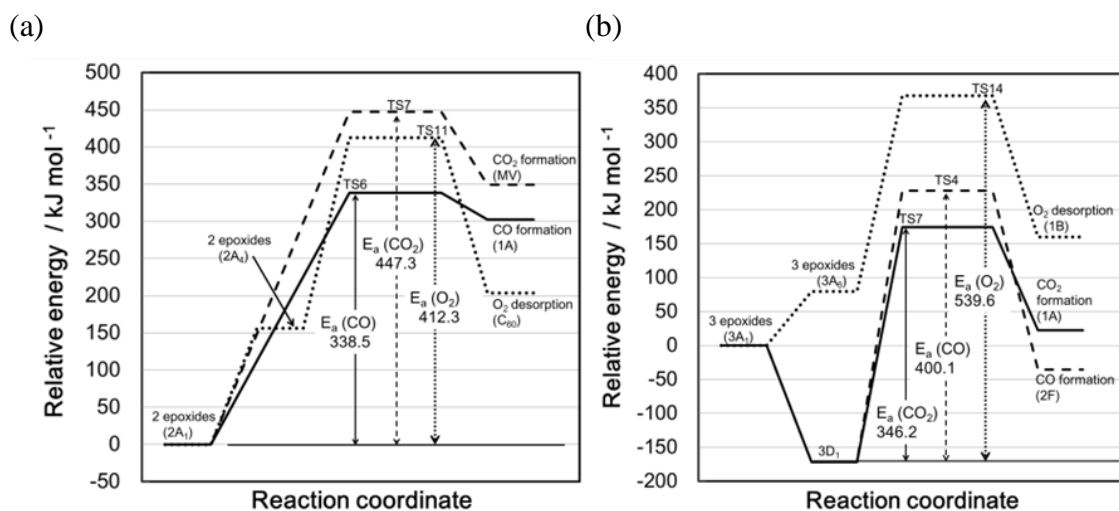


**Figure 3-26** Summarized energy diagrams for pyrolysis of epoxidized  $C_{60}$ . (a) Summary of Figs. 3-20 and 3-21 for the formation of a CO gas (solid line), a  $CO_2$  gas (dashed line), and an  $O_2$  gas (dotted line) gases from two oxygen atoms on  $C_{60}$ . (b) Summary of Fig. 3-25 for the formation of a CO gas (solid line), a  $CO_2$  gas (dashed line), and an  $O_2$  gas (dotted line) from three oxygen atoms on  $C_{60}$ .

### 3.3.6 Comparison with our experimental results

In this work, a CO gas tends to generate via the formation of a lactone group upon pyrolysis of two oxygen atoms on  $C_{60}$ . A  $CO_2$  gas tends to generate via the formation of a combination of a lactone and a ketone group upon pyrolysis of three oxygen atoms on  $C_{60}$ . An  $O_2$  gas is difficult to desorb from both two and three oxygen atoms on  $C_{60}$ .

These calculated results were supported by our following empirical results for pyrolysis of epoxidized  $C_{60}$  [150]. Two to three oxygen atoms on average were introduced on each  $C_{60}$  by epoxidation reaction in a solvent. The functional groups such as C=O and lactone groups were formed by heat treatment of epoxidized  $C_{60}$  at 523 K. At 673 K, lactone groups were decomposed into CO and  $CO_2$  gases. Moreover,  $O_2$ , CO, and  $CO_2$  gases generated from pyrolyzing epoxidized  $C_{60}$  were analyzed by direct injection-mass spectrometry. As the coverage of oxygen atoms on  $C_{60}$  increased, the ratio of the  $CO_2$  gas to the CO gas increased, whereas the amount of the  $O_2$  gas did not change. The amount of the desorbed  $O_2$  gas was negligible. It means that the CO gas and the  $CO_2$  gas tend to form with low and high coverage of oxygen atoms, respectively. The tendency of empirical results [150] is well-matched with that of this calculated work.

## **Chapter 4 Conclusions**

### **4.1 Spectral change of simulated X-ray photoelectron spectroscopy from graphene to fullerene**

Introduction of pentagons in graphene influenced the peak shifts and FWHMs of calculated C1s spectra. The binding energy of the peak top of calculated C1s spectra originated from carbon atoms on pentagons was lower than that originating from carbon atoms on hexagons because of electron-withdrawing nature of the pentagons. Introduction of six or more pentagons shifted the peak top of simulated spectra of graphene to low binding energy and reached the lowest binding energy by introducing twelve pentagons (fullerene). The negative peak shifts of calculated C1s spectra related to the increment of the work function. The FWHM of C1s spectrum of graphene (1.25 eV) increased up to 1.45 eV as the number of pentagons increased up to six because the number of different states of carbon-carbon bondings was maximized. The FWHM decreased down to 1.15 eV by introducing twelve pentagons (fullerene). These results indicate that the number and position of pentagons in graphene can be estimated by analyzing the FWHMs and the peak shifts of C1s spectra.

### **4.2 Pyrolysis of epoxidized fullerenes analyzed by spectroscopies**

Unzipped epoxide, C=O, C-O-C-O-C, and lactone groups were introduced on C<sub>60</sub> by epoxidation as determined by the combined analyses of XPS and DRIFT spectroscopies. After the epoxidized fullerenes were heated at 523 K, the amount of C=O and lactone groups further increased because of the migration of epoxides. The amount of lactone groups decreased more than that of C=O groups between 523 and 673 K and the amount of decomposed the CO<sub>2</sub> gas was more than that of decomposed the CO gas, which indicates that the CO<sub>2</sub> gas can form easier than the CO gas from lactone groups by heat treatment. Mass analysis also indicated that the ratio of the CO<sub>2</sub> gas to the CO gas increased with increasing epoxidation time. Because of the migration of oxygen atoms in the form of lactone groups, either the CO<sub>2</sub> gas or the CO gas were formed. Carbene sites were also generated by formations of CO and CO<sub>2</sub> gases as confirmed by XPS and DRIFT spectra. The carbene site was stabilized by the presence of an adjacent oxygen atom as results of calculation.

### **4.3 Oxygen migration and selective CO and CO<sub>2</sub> formation from epoxidized fullerenes**

Pyrolysis of epoxidized C<sub>60</sub> involving the formation of a CO gas, a CO<sub>2</sub> gas, and an O<sub>2</sub> gas were studied using DFT calculation. It has been reported that migration of one oxygen atom on graphene requires the activation energy of 94.1 kJ mol<sup>-1</sup>. The activation energy for migration of one oxygen atom on C<sub>60</sub> (210.1 ~ 218.2 kJ mol<sup>-1</sup>) is higher than that of graphene, but oxygen atoms on C<sub>60</sub> can migrate, because oxygen atoms in the next-nearest neighbor configurations are energetically more favorable than isolated oxygen atoms, and the activation energy for migration of one oxygen atom toward other oxygen atoms is lower than that of the formation of CO gas from one isolated oxygen.

The formation of a CO gas, a CO<sub>2</sub> gas, and an O<sub>2</sub> gas from two oxygen atoms on C<sub>60</sub> endothermically proceeds. A lactone group formed from two oxygen atoms decomposes and the CO gas and the CO<sub>2</sub> gas form. The combination of a vacancy defect and an ether group generated by the formation of the CO gas is energetically more favorable than a mono-vacancy defect generated by the formation of the CO<sub>2</sub> gas because a carbene site in a combination of vacancy defect and an ether group is stabilized by the ether group. The CO gas tends to form more than the CO<sub>2</sub> gas and the O<sub>2</sub> gas from two oxygen atoms on C<sub>60</sub> because the apparent activation energy for the formation of the CO gas is the lowest among the formation of the CO gas, the CO<sub>2</sub> gas and the O<sub>2</sub> gas.

A combination of a lactone group and a ketone group formed from three oxygen atoms on C<sub>60</sub> is transformed into a combination of a lactone group and an ether group. Decomposition of these functional groups generates both a CO gas and a CO<sub>2</sub> gas. The types of formed gas such as the CO gas and the CO<sub>2</sub> gas depends on the position of the bonding of the ether group positioned next to the lactone group such as C-O-C-C=O-O-C and C-O-C-O-C=O, respectively. The apparent activation energy for the formation of the CO<sub>2</sub> gas is lower than those for the formation of the CO gas and desorption of an O<sub>2</sub> gas. It indicates that the CO<sub>2</sub> gas tends to form more than the CO gas and the O<sub>2</sub> gas from three oxygen atoms.

## References

- [1] H. W. Kroto, J. R. Heath, S. C. O. Brien, R. F. Curl, R. E. Smalley, *Nature* 318 (1985) 162-163.
- [2] S. Iijima, *Nature* 354 (1991) 56-58.
- [3] K. S. Novoselov, A. K. Geim, S. V. Morozov, D. Jiang, Y. Zhang, S. V. Dubonos, L. V. Grigorieba, A. A. Firsov, *Science* 306 (2004) 666-669.
- [4] R. C. Haddon, R. E. Palmer, H. W. Kroto, P. A. Sermon, *Phil. Trans. R. Soc. Lond.* 343 (1993) 53-62.
- [5] H. P. Luthi, J. Almlof, *J. Chem. Phys. Lett.* 135 (1987) 357-360.
- [6] S. Saito, A. Oshiyama, *Phys. Rev. Lett.* 66 (1991) 2637-2640.
- [7] Q. S. Xie, E. Perezcordero, L. Echegoyen, *J. Am. Chem. Soc.* 114 (1992) 3978-3980.
- [8] C. Luo, D. M. Guldi, H. Imahori, K. Tamaki, K. Sakata, *J. Am. Chem. Soc.* 122 (2000) 6535-6551.
- [9] H. Imahori, D. M. Guldi, K. Tamaki, Y. Yoshida, C. P. Luo, Y. Sakata, S. Fukuzumi, *J. Am. Chem. Soc.* 123 (2001) 6617-6628.
- [10] M. A. Herranz, B. Illescas, N. Martin, C. P. Luo, D. M. Guldi, *J. Org. Chem.* 65 (2000) 5728-5738.
- [11] Y. Wang, J. M. Holden, A. M. Rao, W. T. Lee, X. X. Bi, S. L. Ren, G. W. Lehman, G. T. Hager, P. C. Eklund, *Phys. Rev. B* 45 (1992) 14396-14399.
- [12] A. V. Talyzin, Y. O. Tsybin, J. M. Purcell, T. M. Schaub, Y. M. Shulga, D. Noréus, T. Sato, A. Dzwilewski, B. Sundqvist, A. G. Marshall, *J. Phys. Chem. A* 110 (2006) 8528-8534.
- [13] Y. Tajima, K. Takeuchi, *J. Org. Chem.* 67 (2002) 1696-1698.
- [14] A. L. Balch, D. A. Costa, B. C. Noll, M. M. Olmstead, *J. Am. Chem. Soc.* 117 (1995) 8926-8932.
- [15] M. Wohlers, A. Bauer, T. H. Ruhle, F. Neitzel, H. Werner, R. Schlogl, *Fullerene Sci. Technol.* 5 (1997) 49-83.
- [16] L. Y. Chiang, J. W. Swirczewski, C. S. Hsu, S. K. Chowdhury, S. Cameron, K. Creegan, *J. Chem. Soc., Chem. Commun.* 24 (1992) 1791-1793.
- [17] L. Y. Chiang, R. B. Upasani, J. W. Swirczewski, S. Soled, *J. Am. Chem. Soc.* 115 (1993) 5453-5457.
- [18] J. Li, A. Takeuchi, M. Ozawa, X. Li, K. Saigo, K. Kitazawa, *J. Chem. Soc. Chem. Commun.* 23 (1993) 1784-1785.
- [19] K. Kokubo, K. Matsubayashi, H. Tategaki, H. Takada, T. Oshima, *ACS Nano* 2

- (2008) 327-333.
- [20] G. Zhang, Y. Liu, D. Liang, L. Gan, Y. Li, *Angew. Chem. Int. Ed.* 49 (2010) 5293-5295.
- [21] A. Hirsch, Q. Y. Li, F. Wudl, *Angew. Chem. Int. Ed.* 30 (1991) 1309-1310.
- [22] Y. Saito, T. Yoshikawa, M. Inagaki, M. Tomita, T. Hayashi, *Chem. Phys. Lett.* 204 (1993) 277-282.
- [23] D. Ugarte, *Chem. Phys. Lett.* 198 (1992) 596-602.
- [24] R. E. Haufler, J. Conceicao, L. P. F. Chibante, Y. Chai, N. E. Byrne, S. Flanagan, M. M. Haley, S. C. O'Brien, C. Pan, Z. Xiao, W. E. Billups, M. A. Ciufolini, R. H. Hauge, J. L. Margrave, L. J. Wilson, R. F. Curl, R. E. Smalley, *J. Phys. Chem.* 94 (1990) 8634-8636.
- [25] A. Koshio, M. Inakuma, Z. W. Wang, T. Sugai, H. Shinohara, *J. Phys. Chem. B* 104 (2000) 7908-7913.
- [26] R. H. Baughman, A. A. Zakhidov, W. A. de Heer, *Science* 297 (2002) 787-792.
- [27] A. Allaoui, S. Bai, H. M. Cheng, J. B. Bai, *Compos. Sci. Technol.* 62 (2002) 1993-1998.
- [28] S. Bandow, S. Asaka, Y. Saito, A. M. Rao, L. Grigorian, E. Richter, P. C. Eklund, *Phys. Rev. Lett.* 80 (1998) 3779-3782.
- [29] X. Lu, Z. Chen, *Chem. Rev.* 105 (2005) 3643-3696.
- [30] B. W. Smith, M. Monthieux, D. E. Luzzi, *Nature* 396 (1998) 323-324.
- [31] T. Fujimori, A. Morelos-Gómez, Z. Zhu, H. Muramatsu, R. Futamura, U. Koki, M. Terrones, T. Hayashi, M. Endo, S. Y. Hong, Y. C. Choi, D. Tomanek, K. Kaneko, *Nat. Commun.* 4 (2013) 2162.
- [32] L. Xiao, Y. Cao, J. Xiao, B. Schwenzer, M. H. Engelhard, L. V. Saraf, Z. Nie, G. J. Exarhos, J. Liu, *Adv. Mater.* 24 (2012) 1176-1181.
- [33] J. Guo, Y. Xu, C. Wang, *Nano Lett.* 11 (2011) 4288-4294.
- [34] R. S. Ruoff, D. C. Lorents, B. Chan, R. Malhotra, S. Subramoney, *Science* 259 (1993) 346-348.
- [35] W. Chen, X. Pan, X. Bao, *J. Am. Chem. Soc.* 129 (2007) 7421-7426.
- [36] A. N. Khlobystov, *ACS Nano* 5 (2011) 9306-9312.
- [37] Z. Liu, S. Tabakman, K. Welsher, H. Dai, *Nano Res.* 2 (2009) 85-120.
- [38] M. F. P. DPharmSci, M. Bagonluri, *Nanomed. Nanotechnol.* 4 (2008) 183-200.
- [39] D. C. Elias, R. R. Nair, T. M. G. Mohiuddin, S. V. Morozov, P. Blake, M. P. Halsall, A. C. Ferrari, D. W. Boukhvalov, M. I. Katsnelson, A. K. Geim, K. S. Novoselov, *Science* 323 (2009) 610-613.
- [40] R. Grantab, V. B. Shenoy, R. S. Ruoff, *Science* 330 (2010) 946-948.

- [41] C. Lee, X. Wei, J. W. Kysar, J. Hone, *Science* 321 (2008) 385-388.
- [42] K. S. Novoselov, A. K. Geim, S. V. Morozov, D. Jiang, M. I. Katsnelson, I. V. Grigorieva, S. V. Dubonos, A. A. Firsov, *Nature* 438 (2005) 197-200.
- [43] Y. B. Zhang, Y. W. Tan, H. L. Stormer, P. Kim, *Nature* 438(2005) 201-204.
- [44] M. Y. Han, B. Özyilmaz, Y. Zhang, P. Kim, *Phys. Rev. Lett.* 98 (2007) 206805.
- [45] X. Li, X. Wang, L. Zhang, S. Lee, H. Dai, *Science* 319 (2008) 1229-1232.
- [46] T. Ohta, A. Bostwick, T. Seyller, K. Horn, E. Rotenberg, *Science* 313 (2006) 951-954.
- [47] J. J. Palacios, J. Fernández-Rossier, L. Brey, *Phys. Rev. B* 77 (2008) 195428.
- [48] B. R. K. Nanda, M. Sherafati, Z. S. Popović, S. Satpathy, *New J. Phys.* 14 (2012) 083004.
- [49] Y. Wang, Y. Shao, D. W. Matson, J. Li, Y. Lin, *ACS Nano* 4 (2010), 1790-1798.
- [50] Y. Shao, S. Zhang, M. H. Engelhard, G. Li, G. Shao, Y. Wang, J. Liu, I. A. Aksay, Y. Lin, *J. Mater. Chem.* 20 (2010) 7491-7496.
- [51] C. Berger, Z. Song, T. Li, X. Li, A. Y. Ogbazghi, R. Feng, *J. Phys. Chem. B* 108 (2004) 19912-19916.
- [52] K. V. Emtsev, F. Speck, Th. Seyller, L. Ley, J. D. Riley, *Phys. Rev. B* 77 (2008) 155303.
- [53] V. Y. Aristov, G. Urbanik, K. Kummer, D. V. Vyalikh, O. V. Molodtsova, A. B. Preobrajenski, A. A. Zakharov, C. Hess, T. Hanke, B. Buchner, I. Vobornik, J. Fujii, G. Panaccione, Y. A. Ossipyan, M. Knupfer, *Nano Lett.* 10 (2010) 992-995.
- [54] S. Bae, H. Kim, Y. Lee, X. Xu, J.-S. Park, Y. Zheng, J. Balakrishnan, T. Lei, H. R. Kim, Y. I. Song, Y. J. Kim, K. S. Kim, B. Özyilmaz, J. H. Ahn, B. H. Hong, S. Iijima, *Nat. Nanotech.* 5 (2010) 574-578.
- [55] X. Li, W. Cai, J. An, S. Kim, J. Nah, D. Yang, R. Piner, A. Velamakanni, I. Jung, E. Tutuc, S. K. Banerjee, L. Colombo, R. S. Ruoff, *Science* 324 (2009) 1312-1314.
- [56] Z. Li, P. Wu, C. Wang, X. Fan, W. Zhang, X. Zhai, C. Zeng, Z. Li, J. Yang, J. Hou, *ACS Nano* 5 (2011) 3385-3390.
- [57] Y. Wang, Y. Zheng, X. Xu, E. Dubuisson, Q. Bao, J. Lu, K. P. Loh, *ACS Nano* 5 (2011) 9927-9933.
- [58] K. S. Kim, Y. Zhao, H. Jang, S. Y. Lee, J. M. Kim, K. S. Kim, J. H. Ahn, P. Kim, J. Y. Choi, B. H. Hong, *Nature* 457 (2009) 706-710.
- [59] A. Reina, X. Jia, J. Ho, D. Nezich, H. Son, V. Bulovic, *Nano Lett.* 9 (2009) 30-35.
- [60] L. G. D. Arco, Y. Zhang, C. W. Schlenker, K. Ryu, M. E. Thompson, C. Zhou, *ACS Nano* 4 (2010) 2865-2873.
- [61] X. Liang, B. A. Sperling, I. Calizo, G. Cheng, C. A. Hacker, Q. Zhang, Y. Obeng,

- K. Yan, H. Peng, Q. Li, X. Zhu, H. Yuan, A. R. Hight Walker, Z. Liu, L. Peng, C. A. Richter, *ACS Nano* 5 (2011) 9144-9153.
- [62] G. Eda, Y. Y. Lin, C. Mattevi, H. Yamaguchi, H. A. Chen, I. S. Chen, *Adv. Mater.* 22 (2010) 505-509.
- [63] Y. Zhu, S. Murali, W. Cai, X. Li, J. W. Suk, J. R. Potts, R. S. Ruoff, *Adv. Mater.* 22 (2010) 3906-3924.
- [64] P. Blake, P. D. Brimicombe, R. R. Nair, T. J. Booth, D. Jiang, F. Schedin, L. A. Ponomarenko, S. V. Morozov, H. F. Gleeson, E. W. Hill, A. K. Geim, K. S. Novoselov, *Nano Lett.* 8 (2008) 1704-1708.
- [65] J. I. Paredes, S. Villar-Rodil, A. Martinez-Alonso, J. M. D. Tascon, *Langmuir*, 24 (2008) 10560-10564.
- [66] S. Stankovich, R. D. Piner, S. T. Nguyen, R. S. Ruoff, *Carbon* 44 (2006) 3342-3347.
- [67] H. C. Schniepp, J. L. Li, M. J. McAllister, H. Sai, M. Herrera-Alonso, D. H. Adamson, R. K. Prudhomme, R. Car, D. A. Saville, I. A. Aksay, *J. Phys. Chem. B* 110 (2006) 8535-8539.
- [68] H. Chen, M. B. Müller, K. J. Gilmore, G. G. Wallace, D. Li, *Adv. Mater.* 20 (2008) 3557-3561.
- [69] Q. H. Yang, P. X. Hou, S. Bai, M. Z. Wang, H. M. Cheng, *Chem. Phys. Lett.* 345 (2001) 18-24.
- [70] J. Jiang, S. I. Sandler, *Phys. Rev. B* 68 (2003) 245412.
- [71] P. Y. Huang, C. S. Ruiz-Vargas, A. M. van der Zande, W. S. Whitney, M. P. Levendorf, J. W. Kevek, *Nature* 469 (2011) 389-392.
- [72] L. B. Biedermann, M. L. Bolen, M. A. Capano, D. Zemlyanov, R. G. Reifengerber *Phys. Rev. B* 79 (2009) 125411.
- [73] W. Chen, Z. Zhu, S. Li, C. Chen, L. Yan, *Nanoscale* 4 (2012) 2124-2129.
- [74] M. Acik, G. Lee, C. Mattevi, A. Pirkle, R. M. Wallace, M. Chhowalla, K. Cho, Y. Chabal, *J. Phys. Chem. C* 115 (2011) 19761-19781.
- [75] M. Acik, G. Lee, C. Mattevi, M. Chhowalla, K. Cho, Y. J. Chabal, *Nat. Mater.* 9 (2010) 840-845.
- [76] J. U. Lee, W. Lee, J. W. Yi, S. S. Yoon, S. B. Lee, B. M. Jung, *J. Mater. Chem. A* 1 (2013) 12893-12899.
- [77] S. Niyogi, E. Bekyarova, M. E. Itkis, J. L. McWilliams, M. A. Hamon, R. C. Haddon, *J. Am. Chem. Soc.* 128 (2006) 7720-7721.
- [78] S. Kim, S. Zhou, Y. Hu, M. Acik, Y. J. Chabal, C. Berger, W. Heer, A. Bongiorno, E. Riedo, *Nat. Mater.* 11 (2012) 544-549.

- [79] A. Ishitani, Carbon 19 (1981) 269-275.
- [80] R. Larciprete, P. Lacovig, S. Gardonio, A. Baraldi, S. Lizzit, J. Phys. Chem. C 116 (2012) 9900-9908.
- [81] A. Barinov, O. B. Malcioğlu, S. Fabris, T. Sun, L. Gregoratti, M. Dalmiglio, M. Kiskinova, J. Phys. Chem. C 113 (2009) 9009-9013.
- [82] T. Susi, M. Kaukonen, P. Havu, M. P. Ljungberg, P. Ayala, E. I. Kauppinen, Beilstein J. Nanotechnol. 5 (2014) 121-132.
- [83] Y. Yamada, H. Yasuda, K. Murota, M. Nakamura, T. Sodesawa, S. Sato, J. Mater. Sci. 48 (2013) 8171-8198.
- [84] Y. S. Kim, J. H. Kang, T. Kim, Y. Jung, K. Lee, J. Y. Oh, J. Park, C. R. Park, Chem. Mater. 26 (2014) 5549-5555.
- [85] N. Han, T. V. Cuong, M. Han, B. D. Ryu, S. Chandramohan, J. B. Park, J. H. Kang, Y. J. Park, K. B. Ko, H. Y. Kim, H. K. Kim, J. H. Ryu, Y. S. Katharria, C. J. Choi, C. H. Hong, Nat. Commun. 4 (2013) 1452.
- [86] P. J. Larkin, IR and Raman spectroscopy. Principles and Spectral Interpretation. Elsevier Inc, Amsterdam. (2011) 86-90.
- [87] N. B. Colthup, L. H. Daly, S. E. Wiberley, Introduction to infrared and Raman spectroscopy. Academic Press, Massachusetts. (1990) 261-279.
- [88] M. S. Dresselhaus, G. Dresselhaus, R. Saito, A. Jorio, Phys. Rep. 409 (2005) 47-99.
- [89] K. Sasaki, Y. Tokura, T. Sogawa, Crystals. 3 (2013) 120-140.
- [90] A. C. Ferrari, J. C. Meyer, V. Scardaci, C. Casiraghi, M. Lazzeri, F. Mauri, S. Piscanec, D. Jiang, K. S. Novoselov, S. Roth, A. K. Geim, Phys. Rev. Lett. 97 (2006) 187401.
- [91] A. Jorio, R. Saito, J. H. Hafner, C. M. Lieber, M. Hunter, T. McClure, G. Dresselhaus, M. S. Dresselhaus, Phys. Rev. Lett. 86 (2001) 1118-1121.
- [92] S. Itoh, P. Ordejon, D. A. Drabold, R. M. Martin, Phys. Rev. B 53 (1996) 2132-2140.
- [93] V. Lordi, S. X. C. Ma, N. Yao, Surf. Sci. 421 (1999) 150-155.
- [94] L. P. Biro, R. Ehlich, Z. Osvath, A. Koós, Z. E. Horváth, J. Gyulai, J. B. Nagy, Diamond Relat. Mater. 11 (2002) 1081-1085.
- [95] S. V. Lisenkov, I. V. Ponomareva, L. A. Chernozatonskii, Phys. Solid State 46 (2004) 1577-1582.
- [96] J. C. Meyer, C. Kieselowski, R. Erni, M. D. Rossell, M. F. Crommie, A. Zettl, Nano Lett. 8 (2008) 3582-3586.
- [97] P. Y. Huang, C. S. Ruiz-Vargas, A. M. van der Zande, W. S. Whitney, M. P.

- Levendorf, J. W. Kevek, S. Garg, J. S. Alden, C. J. Hustedt, Y. Zhu, J. Park, P. L. McEuen, D. A. Muller, *Nature* 469 (2011) 389-393.
- [98] K. Kim, S. Coh, C. Kisielowski, M. F. Crommie, S. G. Louie, M. L. Cohen, A. Zettl, *Nat. Commun.* 4 (2013) 2723.
- [99] L. Li, S. Reich, J. Robertson, *Phys. Rev. B* 72 (2005) 184109.
- [100] J. Ma, D. Alfe, A. Michaelides, E. Wang, *Phys. Rev. B* 80 (2009) 033407.
- [101] P. Koskinen, S. Malola, H. Häkkinen, *Phys. Rev. Lett.* 101 (2008) 115502.
- [102] C. Pozrikidis, *Arch. Appl. Mech.* 79 (2009) 113-123.
- [103] L. Nasdala, G. Ernst, M. Lengnick, H. Rothert, *Comput. Model. Eng. Sci.* 7 (2005) 293-304.
- [104] Q. Lu, B. Bhattacharya, *Nanotechnology* 16 (2005) 555-566.
- [105] K. I. Tserpes, P. Papanikos, *Compos. Struct.* 79 (2007) 581-589.
- [106] J. H. Eom, H. Lee, J. Im, Electronic structure of defects and quantum transport in carbon nanotubes. *Phys. B: Condensed Matter.* 376-377 (2006) 7-10.
- [107] J. K. Pachos. *Cont. Phys.* 50 (2009) 375-389.
- [108] B. An, S. Fukuyama, K. Yokogawa, M. Yoshimura, M. Egashira, Y. Korai, I. Mochida, *Appl. Phys. Lett.* 78 (2001) 3696-3698.
- [109] R. Tamura, M. Tsukada, *Phys. Rev. B* 49 (1994) 7697-7708.
- [110] S. M. Dubois, A. Lopez-Bezanilla, A. Cresti, F. Triozon, B. Biel, J. C. Charlier, S. Roche, *ACS Nano* 4 (2010) 1971-1976.
- [111] X. Peng, R. Ahuja, *Nano Lett.* 8 (2008) 4464-4468.
- [111] D. Jiang, V. R. Cooper, S. Dai, *Nano Lett.* 9 (2009) 4019-4024.
- [112] H. Du, J. Li, J. Zhang, G. Su, X. Li, and Y. Zhao, *J. Phys. Chem. C* 115 (2011) 23261-23266.
- [113] Y. Yamada, M. Miyauchi, J. Kim, K. Hirose-Takai, Y. Sato, K. Suenaga, T. Ohba, T. Sodesawa, S. Sato, *Carbon* 49 (2011) 3375-3378.
- [114] Y. Yamada, Y. Suzuki, H. Yasuda, S. Uchizawa, K. Hirose-Takai, Y. Sato, K. Suenaga, S. Sato, *Carbon* 75 (2014) 81-94.
- [115] A. W. Robertson, C. S. Allen, Y. A. Wu, K. He, J. Olivier, J. Neethling, A. I. Kirkland, J. H. Warner, *Nat. Commun.* 3 (2012) 1144.
- [116] J. H. Kim, J. H. Hwang, J. Suh, S. Tongay, S. Kwon, C. C. Hwang, J. Wu, J. Y. Park, *Appl. Phys. Lett.* 103 (2013) 171604.
- [117] Y. Yamada, K. Murota, R. Fujita, J. Kim, A. Watanabe, M. Nakamura, S. Sato, K. Hata, P. Ercius, J. Ciston, C. Y. Song, K. Kim, W. Regan, W. Gannett, A. Zettl, *J. Am. Chem. Soc.* 136 (2014) 2232-2235.
- [118] D. P. Yang, X. Wang, X. Guo, X. Zhi, K. Wang, C. Li, G. Huang, G. Shen, Y. Mei,

- D. Cui, *J. Phys. Chem. C* 118 (2014) 725-731.
- [119] H. Mao, R. Wang, J. Zhong, S. Zhong, W. Chen, *Carbon* 76 (2014) 212-219.
- [120] M. H. Gass, U. Bangert, A. L. Bleloch, P. Wang, R. R. Nair, A. K. Geim, *Nat. Nanotechnol.* 3 (2008) 676-681.
- [121] J. C. Meyer, C. Kisielowski, R. Erni, M. D. Rossell, M. F. Crommie, A. Zettl, *Nano Lett.* 8 (2008) 3582-3586.
- [122] M. M. Ugeda, I. Brihuega, F. Guinea, J. M. Gomez-Rodriguez, *Phys. Rev. Lett.* 104 (2010) 096804.
- [123] O. V. Yazyev, L. Helm, *Phys. Rev. B* 75 (2007) 125408.
- [124] A. A. El-Barbary, R. H. Telling, C. P. Ewels, M. I. Heggie, P. R. Briddon, *Phys. Rev. B* 68 (2003) 144107.
- [125] G. D. Lee, C. Z. Wang, E. Yoon, N. M. Hwang, D. Y. Kim, K. M. Ho, *Phys. Rev. Lett.* 95 (2005) 205501.
- [126] S. D. Bergin, V. Nicolosi, P. V. Streich, S. Giordani, Z. Sun, A. H. Windle, *Adv. Mater.* 20 (2008) 1876-1881.
- [127] E. T. Michelson, C. B. Huffman, A. G. Rinzler, R. E. Smalley, R. H. Hauge, J. L. Margrave, *Chem. Phys. Lett.* 296 (1998) 188-194.
- [128] E. T. Michelson, I. W. Chiang, J. L. Zimmerman, P. J. Boul, J. Lozano, J. Liu, R. E. Smalley, R. H. Hauge, J. L. Margrave, *J. Phys. Chem. B* 103 (1999) 4318-4322.
- [129] J. Zheng, H. T. Liu, B. Wu, C. A. Di, Y. L. Guo, T. Wu, G. Yu, Y. Q. Liu, D. B. Zhu, *Sci. Rep.* 2 (2012) 662.
- [130] M. Pumera, R. Scipioni, H. Iwai, T. Ohno, Y. Miyahara, M. Boero, *Chem. Eur. J.* 15 (2009) 10851.
- [131] Y. Shao, J. Wang, H. Wu, J. Liu, I.A. Aksay, Y. Lin, *Electroanal.* 22 (2010) 1027.
- [132] A. K. Geim, K. S. Novoselov, *Nat. Mater.* 6 (2007) 183-191.
- [133] A. H. Castro Neto, F. Guinea, N. M. R. Peres, K. S. Novoselov, A. K. Geim, *Rev. Mod. Phys.* 81 (2009) 109-162.
- [134] D. Jariwala, V. K. Sangwan, L. J. Lauhon, T. J. Marks, M. C. Hersam, *Chem. Soc. Rev.* 42 (2013) 2824-2860.
- [135] K. C. Yung, W. M. Wu, M. P. Pierpoint, F. V. Kusmartsev, *Contemp. Phys.* 54 (2013) 233-251.
- [136] N. Mahmood, C. Z. Zhang, H. Yin, Y. L. Hou, *J. Mater. Chem. A* 2 (2014) 15-32.
- [137] Y. Q. Sun, Q. O. Wu, G. Q. Shi, *Energy Environ. Sci.* 4 (2011) 1113-1132.
- [138] J. Park, W. H. Lee, S. Huh, S. H. Sim, S. B. Kim, K. Cho, B. H. Hong, K. S. Kim, *J. Phys. Chem. Lett.* 2 (2011) 841.
- [139] D. Wei, Y. Liu, Y. Wang, H. Zhang, L. Huang, G. Yu, *Nano Lett.* 9 (2009),

1752-1758.

- [140] P. A. Persson, U. Edlund, P. Jacobsson, D. Johnels, A. Soldatov, B. Sundqvist, *Chem. Phys. Lett.* 258 (1996) 540-546.
- [141] L. Yu, X. Pan, X. Cao, P. Hu, X. Bao, *J. Catal.* 282 (2011) 183-190.
- [142] X. Gao, J. Jang, S. Nagase, *J. Phys. Chem. C* 114 (2010) 832-842.
- [143] K. N. Kudin, B. Ozbas, H. C. Schniepp, R. K. Prudhomme, I. A. Aksay, R. Car, *Nano Lett.* 8 (2008) 36-41.
- [144] C. Huang, C. Li, G. Shi, *Energy Environ. Sci.* 5 (2012) 8848-8868.
- [145] K. Erickson, R. Erni, Z. Lee, N. Alem, W. Gannett, A. Zettl, *Adv. Mater.* 22 (2010) 4467-4472.
- [146] V. N. Popov, L. Henrard, P. Lambin, *Carbon* 47 (2009) 2448-2455.
- [147] X. Rocquefelte, G. M. Rignanese, V. Meunier, H. Terrones, M. Terrones, J. C. Charlier, *Nano Lett.* 4 (2004) 805-810.
- [148] A. A. Gakh, A. Y. Romanovich, A. Bax, *J. Am. Chem. Soc.* 125 (2003) 7902-7906.
- [149] Y. Zhu, T. Yi, B. Zheng, L. Cao, *Appl. Surf. Sci.* 137 (1999) 83-90.
- [150] J. Kim, Y. Yamada, Y. Suzuki, J. Ciston, S. Sato, *J. Phys. Chem. C* 118 (2014) 7076-7084.
- [151] A. Proctor, P. M. A. Sherwood, *J. Electron. Spectrosc. Rel. Phenom.* 27 (1982) 39-56.
- [152] J. P. Boutique, J. J. Verbist, J. G. Fripiat, J. Delhalle, G. Pfister-Guillouzo, G. J. Ashwell, *J. Am. Chem. Soc.* 106 (1984) 4374-4378.
- [153] J. Casanovas, J. M. Ricart, J. Rubio, F. Illas, J. M. Jimenez-Mateos, *J. Am. Chem. Soc.* 118 (1996) 8071-8076.
- [154] S. Souto, M. Pickholz, M. C. dos Santos, F. Alvarez, *Phys. Rev. B* 57 (1998) 2536-2540.
- [155] R. Ohta, K. H. Lee, N. Saito, Y. Inoue, H. Sugimura, O. Takai, *Thin Solid Films* 434 (2003) 296-302.
- [156] W. Zhang, V. Carravetta, Z. Li, Y. Luo, J. Yang, *J. Chem. Phys.* 131 (2009) 244505.
- [157] Y. Yamada, J. Kim, S. Matsuo, S. Sato, *Carbon* 70 (2014) 59-74.
- [158] K. G. Zhou, Y. H. Zhang, L. J. Wang, K. F. Xie, Y. Q. Xiong, H. L. Zhang, C. W. Wang, *Phys. Chem. Chem. Phys.* 13 (2011) 15882-15890.
- [159] F. Banhart, J. Kotakoski, A. V. Krasheninnikov, *ACS Nano* 5 (2011) 26-41.
- [160] J. M. Carlsson, F. Hanke, S. Linic, M. Scheffler, *Phys. Rev. Lett.* 102 (2009) 166104.

- [161] A. Bagri, C. Mattevi, M. Acik, Y. J. Chabal, M. Chhowalla, V. B. Shenoy, *Nat. Chem.* 2 (2010) 581-587.
- [162] Y. Miyata, T. Kawai, Y. Miyamoto, K. Yanagi, Y. Maniwa, H. Kataura, *J. Phys. Chem. C* 111 (2007) 9671-9677.
- [163] Y. Yamada, O. Kimizuka, K. Machida, S. Suematsu, K. Tamamitsu, S. Saeki, Y. Yamada, N. Yoshizawa, O. Tanaike, J. Yamashita, F. Don, K. Hata, H. Hatori, *Energy Fuels* 24 (2010) 3373-3377.
- [164] J. P. Deng, C. Y. Mou, *Fullerene Sci. Technol.* 5 (1997) 1325-1336.
- [165] L. R. Radovic, A. B. Silva-Tapia, F. Vallejos-Burgos, *Carbon* 49 (2011) 4218-4225.
- [166] X. Y. Zhu, S. M. Lee, Y. H. Lee, T. Frauenheim, *Phys. Rev. Lett.* 85 (2000) 2757-2760.
- [167] T. Sun, S. Fabris, *Nano Lett.* 12 (2012) 17-21.
- [168] L. R. Radovic, A. B. Silva-Tapia, F. Vallejos-Burgos, *Carbon* 49 (2011), 4226-4238.
- [169] T. Sun, S. Fabris, S. Baroni, *J. Phys. Chem. C* 115 (2011) 4730-4737.
- [170] R. Larciprete, S. Fabris, T. Sun, P. Lacovig, A. Baraldi, S. Lizzit, *J. Am. Chem. Soc.* 133 (2011), 17315-17321.
- [171] Y. Quo, N. Karasawa, William A. Goddard III, *Nature* 351 (1991) 464-467.
- [172] P. Scharff, C. Siegmund, K. Risch, *Nanotub. Car. N.* 13 (2005) 497-509.
- [173] J. D. Fortner, D. I. Kim, A. M. Boyd, J. C. Farkner, S. Moran, V. L. Corvin, J. B. Hughes, J. H. Kim, *Environ. Sci. Technol.* 41 (2007) 7497-7502.
- [174] Y. Wang, D. Nepal, K. E. Geckeler, *J. Mater. Chem.* 15 (2005) 1049-1054.
- [175] V. I. Ladyanov, V. V. Aksenovab, R. M. Nikonova, *Russ. J. Phys. Chem. A* 84 (2009) 1699-1705.
- [176] P. M. Ajayan, S. Iijima, *Nature* 361 (1993) 333-334.
- [177] P. M. Ajayan, T. W. Ebbesen, T. Ichihashi, S. Iijima, K. Tanigaki, H. Hiura, *Nature* 362 (1993) 522-525.
- [178] S. C. Tsang, P. J. H. Harris, M. L. H. Green, M. L. Nature 362 (1993) 520-522.
- [179] A. C. Dillon, K. M. Jones, T. A. Bekkedahl, C. H. Kiang, D. S. Bethune, M. J. Heben, *Nature* 386 (1997) 377-379.
- [180] M. S. C. Mazzoni, H. Chacham, P. Ordejón, D. Sánchez-Portal, J. M. Soler, E. Artacho, *Phys. Rev. B* 60 (1999) 2208-2211.
- [181] D. B. Mawhinney, V. Naumenko, A. Kuznetsova, J. T. Yates Jr, J. Liu, R. E. Smalley, *J. Am. Chem. Soc.* 122 (2000) 2383-2384.
- [182] B. W. Smith, D. E. Luzzi, *Chem. Phys. Lett.* 321 (2000) 169-174.

- [183] R. Kitaura, H. Shinohara, *Jpn. J. Appl. Phys.* 46 (2007) 881-891.
- [184] R. Kitaura, N. Imazu, K. Kobayashi, H. Shinohara, *Nano Lett.* 8 (2008) 693-699.
- [185] K. Hirahara, K. Suenaga, S. Bandow, H. Kato, T. Okazaki, H. Shinohara, S. Iijima, *Phys. Rev. Lett.* 85 (2000) 5384-5387.
- [186] J. H. Warner, S. R. Plant, N. P. Young, K. Porfyrakis, A. I. Kirkland, G. A. D. Briggs, *ACS Nano* 5 (2011) 1410-1417.
- [187] N. L. Rangel, J. C. Sotelo, J. M. Seminario, *J. Chem. Phys.* 131 (2009) 031105.
- [188] J. L. Li, K. Kudin, M. McAllister, R. Prud'homme, I. Aksay, R. Car, *Phys. Rev. Lett.* 96 (2006) 176101.
- [189] Z. Li, W. Zhang, Y. Luo, J. Yang, J. G. Hou, *J. Am. Chem. Soc.* 131. (2009), 6320-6321.
- [190] K. A. Mkhoyan, A. W. Contryman, J. Silcox, D. A Stewart, G. Eda, C. Mattevi, S. Miller, M. Chhowalla, *Nano Lett.* 9 (2009) 1058-1063.
- [191] A. Bagri, R. Grantab, N. V. Medhekar, V. B. Shenoy, *J. Phys. Chem. C* 114 (2010) 12053-12061.
- [192] S. Fujii, T. Enoki, *J. Am. Chem. Soc.* 132 (2010) 10034-10041.
- [193] M. J. Frisch, G. W. Trucks, H. B. Schlegel, G. E. Scuseria, M. A. Robb, J. R. Cheeseman, J. A. Montgomery, T. Jr.; Vreven, K. N. Kudin, J. C. Burant, et al. *Gaussian 09*, Revision D.01, Gaussian, Inc., 2009.
- [194] T. Koopmans, *Physica* 1 (1933) 104-113.
- [195] D. Briggs, J. T. Grant, *Surface analysis by Auger and X-ray photoelectron spectroscopy*. West Sussex and Manchester. IMPublications and SurfaceSpectra Ltd, (2003) 401-403.
- [196] K. Endo, D. Matsumoto, Y. Takagi, S. Shimada, T. Ida, M. Mizuno, Y. Suzuki, K. Takahashi, K. Uchida, H. Yajima, *J. Surf. Anal.* 14 (2008) 348-351.
- [197] W. Y. Li, A. A. Ibrahimi, K. Goto, R. Shimizu, *J. Surf. Anal.* 12 (2005) 109-112.
- [198] M. Shiraishi, M. Ata, *Carbon* 39 (2001) 1913-1917.
- [199] D. Briggs, J. T. Grant, *Surface analysis by Auger and X-ray photoelectron spectroscopy*. West Sussex and Manchester. IMPublications and SurfaceSpectra Ltd, (2003) 39.
- [200] J. Kim, Y. Yamada, S. Sato, *J. Phys. Chem. C* 118 (2014) 7085-7093.
- [201] L. R. Radovic, A. F. Silva-Villalobos, A. B. Silva-Tapia, F. Vallejos-Burgos, *Carbon* 49 (2011) 3471-3487.
- [202] J. Klocek, K. Kolanek, D. Schmeißer, *J. Phys. Chem. Solid.* 73 (2012) 699-706.
- [203] Y. Ma, P. O. Lehtinen, A. S. Foster, R. M. Nieminen, *New J. Phys.* 6 (2004) 68.

## List of publications

1. **J. Kim**, Y. Yamada, M. Kawai, S. Sato, "Spectral change of simulated X-ray photoelectron spectroscopy from graphene to fullerene", *Diamond Relat. Mater.* under revision.
2. **J. Kim**, Y. Yamada, S. Sato, "Oxygen migration and selective CO and CO<sub>2</sub> formation from epoxidized fullerenes", *J. Phys. Chem. C* 118(13) (2014) 7085-7093.
3. **J. Kim**, Y. Yamada, Y. Suzuki, J. Ciston, S. Sato, "Pyrolysis of epoxidized fullerenes analyzed by spectroscopies", *J. Phys. Chem. C* 118(13) (2014) 7076-7084.
4. Y. Yamada, **J. Kim**, S. Matsuo, S. Sato, "Nitrogen-containing graphene analyzed by X-ray photoelectron spectroscopy", *Carbon* 70 (2014) 7059-7074.
5. Y. Yamada, K. Murota, R. Fujita, **J. Kim**, A. Watanabe, M. Nakamura, S. Sato, K. Hata, E. Peter, J. Ciston, C. Song, K. Kim, W. Regan, W. Gannett, A. Zettl, "Subnanometer vacancy defects introduced on graphene by oxygen gas", *J. Am. Chem. Soc.* 136(6) (2014) 2232-2235.
6. Y. Yamada, M. Miyauchi, **J. Kim**, K. H. Takai, Y. Sato, K. Suenaga, T. Ohba, T. Sodesawa, S. Sato, "Exfoliated graphene ligands stabilizing copper cations", *Carbon* 49(10) (2011) 3375-3378.

## List of presentations (International conference)

1. **J. Kim**, Y. Yamada, S. Sato, "X-ray photoelectron spectroscopy analyses of graphene including pentagons and heptagons", *Carbon 2014*, Jeju, Korea, June 30. 2014. (Oral)
2. **J. Kim**, Y. Yamada, S. Sato, "High-density pentagons and heptagons on graphene", *Carbon 2014*, Jeju, Korea, July 1. 2014.(Poster)
3. **J. Kim**, R. Fujita, Y. Yamada, S. Sato, "Bromination of carbon materials with pentagon, heptagon, and oxygen", *Carbon 2014*, Jeju, Korea, July 1. 2014.(Poster)
4. **J. Kim**, Y. Yamada, T. Sodesawa, S. Sato, "Analysis of defective fullerene by spectroscopy and calculation of density functional theory", *Carbon 2012*, Auditorium Maximum, Krakow, Poland, June 18. 2012.(Poster)
5. **J. Kim**, Y. Yamada, T. Sodesawa, and S. Sato, "Introducing defects on fullerene through epoxidation", *Carbon 2011*, East China University of Science and Technology, Shanghai, China, July 25. 2011.(Poster)

## **List of awards**

1. [KCS Student Award] World conference Carbon 2014, Jeju, Korea, July 4. 2014.

Title of the presentation: Bromination of carbon materials with pentagon, heptagon, and oxygen.

2. [Presentation Award] The 40th annual meeting on carbon, Kyoto, Japan, Dec. 3. 2013.

Title of the presentation: X-ray photoelectron spectroscopy analyses of graphene including pentagons and heptagons.

## **Acknowledgement**

I would like to thank all of the faculty and staff of Department of Applied Chemistry and Biotechnology for the many diverse ways in which they have assisted me in my research at Chiba University. I would like to express the deepest appreciation to my academic advisor, Assistant Prof. Yasuhiro Yamada, whose encouragement, guidance, and support from the initial to the final research stage enabled me to develop understanding of the subject. I am deeply grateful to Prof. Satoshi Sato for the valuable advices and discussions. I am also very grateful to Prof. Motoi Machida, Prof. Keiki Kishikawa, and Prof. Nagahiro Hoshi for serving on my committee and providing me the insightful comments and suggestions.

This dissertation would not be possible without significant contributions from the members of Prof. Satoshi Sato's group for the discussions and assistances of the experiments. Especially, previous group members such as Mr. Masato Miyauchi, Mr. Kazumasa Murota, Ms. Yukiko Suzuki, and Mr. Ryo Fujita and present group members such as Ms. Saiko Uchizawa, Mr. Yosuke Tanaka, Mr. Shintarou Matsuo, Ms. Miki Kawai, and Mr. Takehiro Tanabe have provided me valuable assistances.

I would also like to express my gratitude to Japanese Government Scholarship for supporting my graduate study and Japan Society for the Promotion of Science Fund for studying abroad in U.S.A. My friends such as Ms. Sujin Shin, Mr. Sangcheol Koh, Mr. Kyunghun Kim, Mr. Jungwon Yang, Mr. Yongwoon Jung, Mr. Hyunpil Kim, Mr. Dongyoung Kim, Mr. Kyungrok Kim, Mr. Jaebo Woo, and Mr. Minu Jun deserve my deepest gratitude. At last but not least, I would like to thank my family for their endless love, understanding, support, encouragement and sacrifice throughout my study. Finally, God, I thank for all you have done. I truly appreciate everything.